

AD-A046 297

ILLINOIS UNIV AT URBANA-CHAMPAIGN DEPT OF ELECTRICAL --ETC F/G 17/5
STUDIES OF EXTRINSIC SILICON INFRARED DETECTORS.(U)

AUG 77 C T SAH

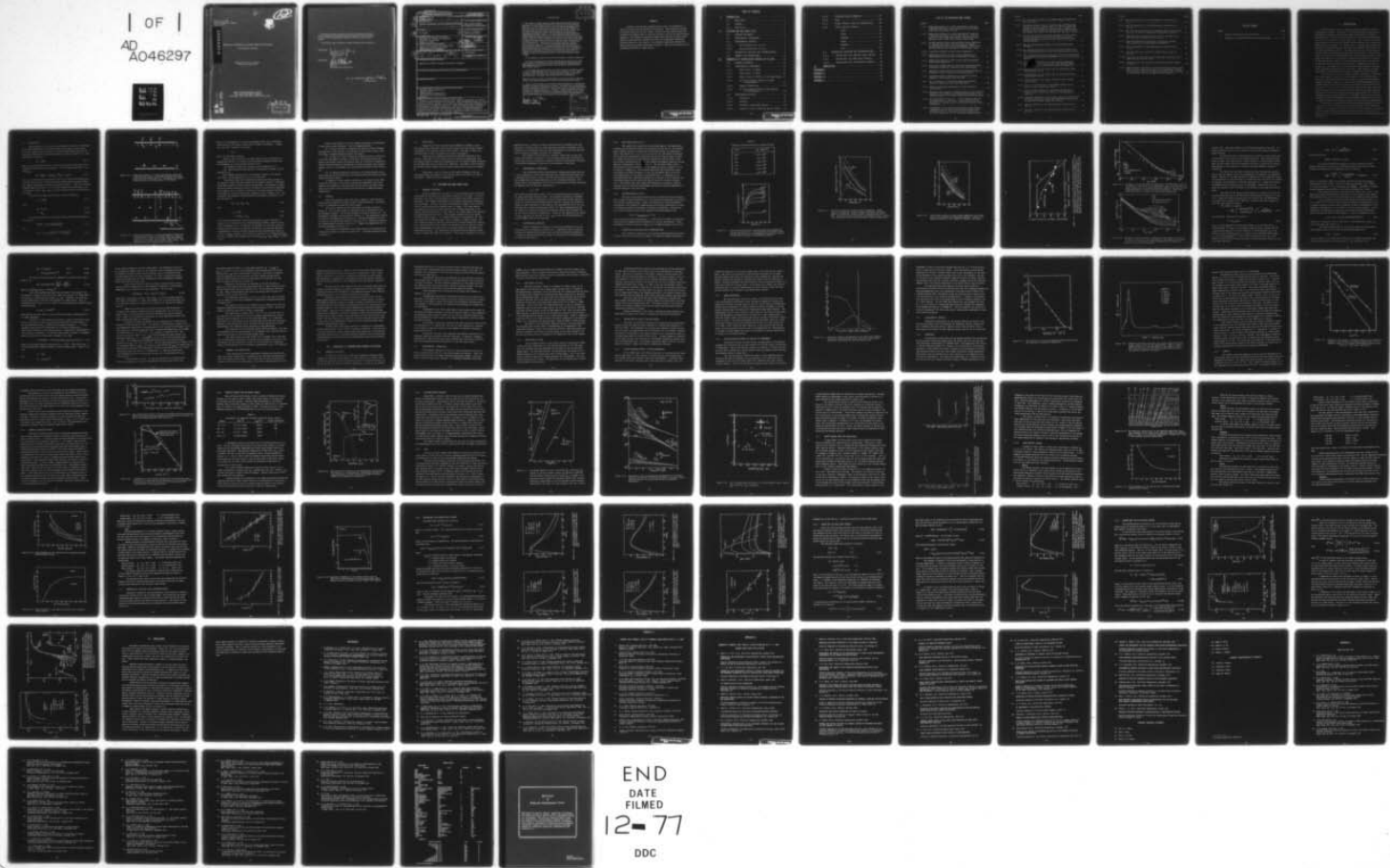
F19628-72-C-0199

UNCLASSIFIED

RADC-TR-77-295

NL

| OF |
AD
A046297



END
DATE
FILED
12-77
DDC

RADC-TR-77-295
Final Technical Report
August 1977



12

AD A 046297

STUDIES OF EXTRINSIC SILICON INFRARED DETECTORS

University of Illinois

Approved for public release;
distribution unlimited.

ROME AIR DEVELOPMENT CENTER
AIR FORCE SYSTEMS COMMAND
GRIFFISS AIR FORCE BASE, NEW YORK 13441

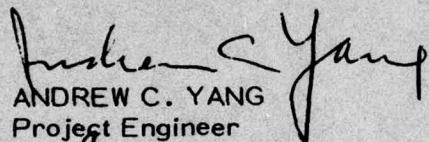
AD No. _____
DDC FILE COPY:

D D C
REF ID: A65117
NOV 9 1977
RECEIVED
D

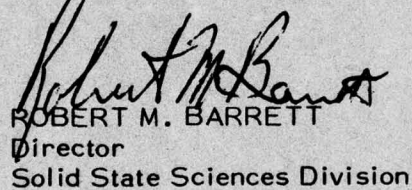
This report has been reviewed by the RADC Information Office (OI) and is releasable to the National Technical Information Service (NTIS). At NTIS it will be releasable to the general public, including foreign nations.

This technical report has been reviewed and approved for publication.

APPROVED:


ANDREW C. YANG
Project Engineer

APPROVED:


ROBERT M. BARRETT
Director
Solid State Sciences Division

FOR THE COMMANDER:


John P. Thuss
Plans Office

UNCLASSIFIED

SECURITY CLASSIFICATION OF THIS PAGE (When Data Entered)

(19) REPORT DOCUMENTATION PAGE			READ INSTRUCTIONS BEFORE COMPLETING FORM
1. REPORT NUMBER RADC-TR-77-295	2. GOVT ACCESSION NO.	3. RECIPIENT'S CATALOG NUMBER	
4. TITLE (and Subtitle) STUDIES OF EXTRINSIC SILICON INFRARED DETECTORS.	5. TYPE OF REPORT & PERIOD COVERED FINAL 01APR77-30MAR77		
6. AUTHOR(s) C. T. SAH	7. CONTRACT OR GRANT NUMBER(s) F19628-72-C-0199		
8. PERFORMING ORGANIZATION NAME AND ADDRESS Department of Electrical Engineering University of Illinois Urbana, IL 61801	9. PROGRAM ELEMENT, PROJECT, TASK AREA & WORK UNIT NUMBERS 61102F 23061203		
10. CONTROLLING OFFICE NAME AND ADDRESS Deputy for Electronic Technology (RADC) Hanscom AFB, Massachusetts 01731 Monitor/Andrew C. Yang/ETSD	11. REPORT DATE August 1977		
12. MONITORING AGENCY NAME & ADDRESS (if different from Controlling Office) Final rept. 1 Apr 72-30 Mar 73	13. NUMBER OF PAGES 89		
14. SECURITY CLASS. (of this report) Unclassified	15. DECLASSIFICATION/DOWNGRADING SCHEDULE		
16. DISTRIBUTION STATEMENT (of this Report) Approved for public release; distribution unlimited	17. DISTRIBUTION STATEMENT (of the abstract entered in Block 20, if different from Report)		
18. SUPPLEMENTARY NOTES			
19. KEY WORDS (Continue on reverse side if necessary and identify by block number) Extrinsic Silicon Detectors Impurity State Thermal Capture Emission Rate Photoionization Cross-Section Mobility	20. ABSTRACT (Continue on reverse side if necessary and identify by block number) Studies of the material parameters which limit the performance of silicon extrinsic infrared detectors are reported. These parameters include the carrier mobilities and the thermal, optical and Auger-impact generation-recombination-trapping rates at impurity and defect centers and impurity-defect complexes. The transient capacitance methods have been used to obtain these material characterization parameters as well as the generation annealing-diffusion kinetics of the centers. The transient capacitance methods are refined to give concentration profiles of recombination centers.		

D D C

RECEIVED
NOV 9 1977
RECORDED
D

EVALUATION

1. This report is a final report covering research studies during the five year period, 1 April 1972 to 30 March 1977, on extrinsic silicon infrared detectors. The main objective was to study the material parameters which limit and control the performance of silicon extrinsic infrared detectors. These parameters include carrier mobilities and the thermal, optical, and generation-recombination-trapping rates at impurity (sensing levels) compensation and defect centers. The experimental approach made use of and extended transient junction current and capacitance measurement techniques to determine photo-ionization cross sections, and thermal capture and emission rates as a function of temperature, electric field, and concentration of impurity and defect centers as well as to determine the concentration profile of these centers. Theoretical interpretation included calculations of photo-ionization cross sections and ion scattering mobilities using the pseudo-impurity potential. A new objective added during the fifth year of the contract became the central force of the follow-on contract (F19628-77-C-0138); namely, the study of the physical mechanism and circuit model of low frequency 1/f noise generated at the SiO₂-Si interface states which are relevant to signal processing applications. Some of the important results include:

- a) The absence of impurity ion position correlation in mobility scattering.
- b) Further development of transient capacitance technique so as to detect and characterize minute amount of impurities and defects introduced during high temperature processing as well as to fine probe the concentration profiles of these centers.
- c) The study and characterization of numerous impurity and defect centers in silicon including phosphorous, bismuth, gold, magnesium, silver, cobalt, chromium, sulfur, tantalum, zinc, aluminum-oxygen complexes, thermally generated donors, and defect centers generated by ion implantation.

Support from this contract was acknowledged in 6 master's theses, 7 doctoral theses, and 51 papers published in the open literature during its duration.

2. Silicon extrinsic detectors are finding rapidly widening use in surveillance, guidance, and optical communication systems. This study has contributed basic information needed in extending the range of applicability of IR detectors through the use of new sensing impurities. In addition, it has provided basic material parameters on shallow and deep level impurity and defect centers which control and limit the sensitivity, uniformity and bandwidth of presently used detectors and projected large scale arrays based on these detectors.

Andrew C. Yang
ANDREW C. YANG
Project Engineer

ACCESSION FOR	
NTIS	White Section <input checked="" type="checkbox"/>
DDC	Buff Section <input type="checkbox"/>
UNANNOUNCED <input type="checkbox"/>	
JUSTIFICATION.....	
BY.....	
DISTRIBUTION/AVAILABILITY CODES	
Dist.	AVAIL. AND/or SPECIAL
A	

SUMMARY

Studies of the material parameters which limit the performance of silicon extrinsic infrared detectors are reported. These parameters include the carrier mobilities and the thermal, optical and Auger-impact generation-recombination-trapping rates at impurity and defect centers and impurity-defect complexes. The transient capacitance methods have been used to obtain these material characterization parameters as well as the generation-annealing-diffusion kinetics of the centers. The transient capacitance methods have been extended and refined during this contract to allow for fine probing of the concentration profile of these centers.

TABLE OF CONTENTS

I.	INTRODUCTION	1
1.1	OBJECTIVES	2
1.2	CONTENT	5
1.3	STATISTICS	6
II.	ELECTRON AND HOLE MOBILITIES	6
2.0	PROBLEM STATEMENT	6
2.1	EXPERIMENTAL TECHNIQUES	7
2.2	EXPERIMENTAL RESULTS	7
2.2.1	Hole Conductivity in p-Si	8
2.2.2	Electron Mobility in n-Si	8
2.3	THEORETICAL ANALYSIS AND INTERPRETATION . . .	8
2.4	SUMMARY AND SUGGESTIONS	18
III.	PROPERTIES OF IMPERFECTION CENTERS IN SILICON . . .	19
3.0	PROBLEM STATEMENT	19
3.1	EXPERIMENTAL TECHNIQUES	20
3.1.1	Edge Effect in TSCAP	21
3.1.2	Edge Effect in VSCAP	21
3.1.3	Capture Rate by VSCAP in the Edge Region .	22
3.1.4	Series Resistance Effect in VSCAP Measurements	22
3.1.5	Sample Preparation	23
3.1.6	On-Line Computer Control and Analysis of Experiments	23
3.2	EXPERIMENTAL RESULTS	25
3.2.1	Phosphorus	25
3.2.2	Bismuth	28
3.2.3	Thermally Generated Centers	30
3.2.4	Impurity Centers from the Boron+ Source .	32

3.2.5	Aluminum-Oxygen Complexes	34
3.2.6	Gold	34
3.2.7	Defect Centers from Ion Implantation . .	38
3.2.8	Other Impurity Centers	40
	Silver	40
	Cobalt	42
	Chromium	42
	Sulfur	42
	Tantalum	43
	Zinc	45
3.3	THEORETICAL ANALYSES AND INTERPRETATIONS. . .	45
3.3.1	Coulomb Well for Shallow Level Centers .	48
3.3.2	Square Well for Deep Level Centers. . . .	52
3.3.3	Coulomb Well for Two-Electron Centers . .	55
IV.	CONCLUSIONS	59
REFERENCES		61
APPENDIX A		65
APPENDIX B		67
APPENDIX C		73

LIST OF ILLUSTRATIONS AND FIGURES

Figure	Page
1.1.1 Energy band diagram of a n-type semiconductor doped with a shallow level acceptor with energy level E_A and shallow level donor with energy level E_D	3
1.1.2 Energy lavel diagram of a n-type semiconductor doped with a shallow level acceptor with energy level E_A , a shallow level donor with energy level E_D and a deep recombination impurity, such as gold, with an energy level of E_{Au}	3
2.2.1 Ionized impurity and hole concentrations versus temperature for devices used in [3]. Dots are values of impurity concentration obtained from C-V measurements. Solid curves are hole concentration corrected for deionization effects.	9
2.2.2 Conductivity mobility of holes versus temperature.	10
2.2.3 Conductivity mobility of holes versus temperature for devices used in [3] corrected for deionization effects	11
2.2.4 Conductivity mobility of holes versus impurity concentration at room temperature.	12
2.2.5 Theoretical ionized impurity scattering electron mobilities in silicon at 300°K as a function of ion concentration	13
2.2.6 Theoretical ionized impurity scattering electron mobility in silicon at 77°K as a function of ion concentration.	13
3.1.1 Normalized frequency dependence of C and G/W of device 96D1p5 at 2 volts reverse bias and 23.9K.	24
3.2.1 The conductance of a n+/n/n+ phosphorus-doped silicon diode as a function of reciprocal temperature.	26
3.2.2 Thermally stimulated capacitance for sulfur doped p ⁺ -n silicon diode	27
3.2.3 Reciprocal time constant or thermal emission rate of electrons trapped at the phosphorus and bismuth impurity atoms in the depletion region of the reverse biased Schottky Barrier diode. .	29
3.2.4 The concentration of Bi as a function of distance from the pn junction which is 0.5 micron from the surface for the diffused p+/r labeled (2) and for the Schottky Barrier diode labeled (1).	31
3.2.5 A comparison of the electron concentration calculated from experimental data of high frequency SB capacitance versus temperature with the theoretical electron concentration of silicon doped with 3.0×10^{14} Bi/cm ³ with $E_C - E_D = 70.90$ mev. .	31

Figure	Page
3.2.6 The concentration profile of the aluminum N_{Al} , and $E_V + 392$ meV hole trap, N_{392}	33
3.2.7 The thermal emission rates of electrons, e_{n1}^t , and holes, e_{p0}^t , trapped at the gold acceptor center, $E_C - 547$ mV or $E_V + 590$ mV, and the thermal emission rates of holes, e_{p-1}^t , trapped at the gold donor center, $E_V + 345$ mV, obtained from the dark transient measurements, the latter for time constants less than 1 second .	35
3.2.8 The electric field and temperature dependences of the thermal capture coefficients of electrons and holes at the gold acceptor and donor centers in silicon from the photo capacitance experiments.	36
3.2.9 c_{n0}^t for a gold doped p+n diode, at a field between 0 and 6.7 KV/cm.	37
3.2.10 The outdiffusion profile of gold in the silicon surface layer into an aluminum sink in an Al on n-Si Schottky barrier diode. .	39
3.2.11 The concentration profile of gold near the silicon surface from dark transient capacitance measurements on a Al on n-Si Schottky barrier diode.	39
3.2.12 The reciprocal emission rate or the transient capacitance decay constants of the energy levels generated during ionization as a function of reciprocal temperature	41
3.2.13 Field dependence of the capture rate of electrons by singly ionized sulfur centers	41
3.2.14 Field dependence of the capture rate of electrons by doubly ionized sulfur centers	44
3.2.15 Field dependence of the impact ionization rate of neutral sulfur centers	44
3.2.16 Electric field dependence of the thermal capture rate of holes at singly ionized zinc centers	46
3.2.17 Electric field dependence of the thermal capture rate of holes at doubly ionized zinc centers at the temperatures indicated	46
3.2.18 Temperature dependence of the thermal capture rate of electrons at singly ionized zinc centers and Auger-impact emission rate of electrons at doubly ionized zinc centers.	47
3.3.1 Spectral dependence of the photoionization cross-section of B in Si.	49
3.3.2 Spectral dependence of the photoionization cross-section of Al in Si	49

Figure		Page
3.3.3	Spectral dependence of the photoionization cross-section of Ga in Si	50
3.3.4	Spectral dependence of the photoionization cross-section of In in Si	50
3.3.5	The effective radii versus the ionization energy for the ground states of the Group-III and Group-V impurities in silicon.	51
3.3.6	Photoionization cross-section spectra of the s-bound state of spherical square potential well of radius a.	51
3.3.7	Hole photoionization cross-section of the $E_T - E_V = 207$ meV defect generated by one-MeV electron irradiation	54
3.3.8	Spectral dependence of the photoionization cross-section of In in Si.	54
3.3.9	Photoionization cross section of neutral sulfur centers in silicon.	56
3.3.10	Linear plot of the 0.285-eV peak, indicating a Lorentzian line shape with half-width of 6 meV.	56
3.3.11	Photoionization cross section of singly ionized sulfur centers in silicon.	58
3.3.12	Highly sensitive measurement of the photoionization cross section from the optical emission rate data of the capacitance transient from electrons trapped at the deep sulfur donor center in silicon at 613 meV below the silicon conduction band edge [34].	58

LIST OF TABLES

Table	Page
1 Impurity Concentration of p-type Silicon	9
2 Parameters of Impurity Centers from the Boron+ Source	32

I. INTRODUCTION

Infrared detector is one of the most important elements in optical communication receivers. Many types of solid state detectors (particularly semiconductor detectors) have been developed to meet specific system requirements.[1,2] Both the junction (photovoltaic, PV) and bulk (photoconductive, PC) type of devices have been widely used. The p-n junction type generally operates as an intrinsic detector (optical generation of electron-hole pairs across the band gap). The Schottky barrier junction type operates by collecting the optically excited electrons from the metal Fermi surface over the metal-semiconductor barrier. The photoconductive type can be either an intrinsic detector, employing interband optical generation of electron-hole pairs in relatively pure semiconductor bulk, or an extrinsic detector, using a doped semiconductor in the deionization temperature range where a fraction of the impurities are neutral so that the trapped electrons (or holes) can be optically excited in the detection process. Germanium, doped with Au, Zn, Hg, etc., was widely used as cooled extrinsic photoconductive detectors in the intermediate infrared range in the past. More recently, intrinsic photovoltaic and photoconductive detectors in HgCdTe have been developed.

From the point of view of ultimate detector sensitivity or detectivity D*, and the signal to noise ratio, there appears to be little differences among the various materials when the detector is operated under background limited conditions. However, in order to reach the photon background noise limited condition, the intrinsic noise sources within the detector must be minimized. It is felt that silicon extrinsic detectors may offer some advantages in reducing and controlling the noise sources in individual detector devices and in array and integrated structure applications due to the well developed silicon process technology. In addition, there are also some advantages in radiation hardening from the knowledge accumulated on the effect of ionizing radiation and radiation defects on silicon device characteristics.

This study is concerned with the theoretical and experimental investigation of recombination-generation-trapping kinetics and the fundamental properties of the material parameters such as the thermal capture and emission rates of trapped electrons and holes and photoionization cross-sections of impurity centers in silicon materials useful for extrinsic infrared photodetector applications.

1.1 OBJECTIVES

The performance of an extrinsic photoconductive detector is determined by the photoconductivity and the detectivity or the signal to noise ratio. As a first example, let us consider an n-type silicon without deep level recombination centers whose energy level diagram is given in Figure 1.1.1. The photocurrent is given by

$$J_S = q\mu_n E \Delta N \quad (1.1)$$

where μ_n is the electron mobility, E is the bias electric field and ΔN is the steady-state photoelectron concentration. For low steady-state level, i.e., $\Delta N \ll N_{dark}$,

$$\Delta N = e^0 N_D \tau_n = \sigma^0 \phi_s N_D \tau_n = \alpha^0 \phi_s \tau_n = n \phi_s \tau_n / L \quad . \quad (1.2)$$

Here, ϕ_s is the photon flux (photons/cm²-sec), σ^0 is the average photoionization cross section over the photon spectrum and the detector spectral range, $\alpha^0 = \sigma^0 N_D$ is the average absorption coefficient (1/cm), $n = \alpha^0 L$ is the average internal quantum efficiency, L is the sample length in the direction of the illumination, and $N_D = N_{DD} - N_{AA}$ is the dark trapped electron concentration at the donors.

The low level steady-state electron lifetime is given by

$$\tau_n = 1/c_n^t P_D \quad (1.3)$$

where

$$P_D = N_{DD} - N_D \quad (1.4)$$

$$= N_{AA} \quad (1.4a)$$

For the ideal example, the signal-to-noise ratio and the detectivity are given by

$$\sqrt{\Delta f S/N} = (n \phi_s / 2) \sqrt{N_{DD} \tau_n A / P_D N_D L} \quad (1.5)$$

and

$$D^* = (n \mu_n / 2 h v_s) \sqrt{(c_n^t / L) (1 - 1/c_n^t \tau_n N_{DD})^{-1}} \quad (1.6)$$

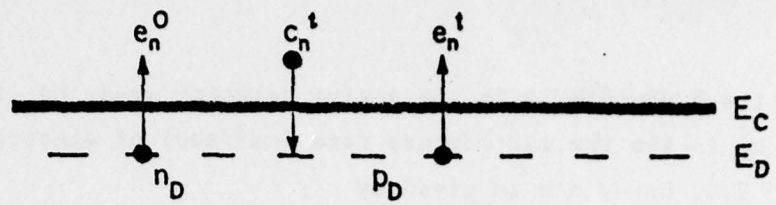


Figure 1.1.1 Energy band diagram of a n-type semiconductor doped with a shallow level acceptor with energy level E_A and shallow level donor with energy level E_D . The thermal and optical transition rates are indicated next to the arrows.

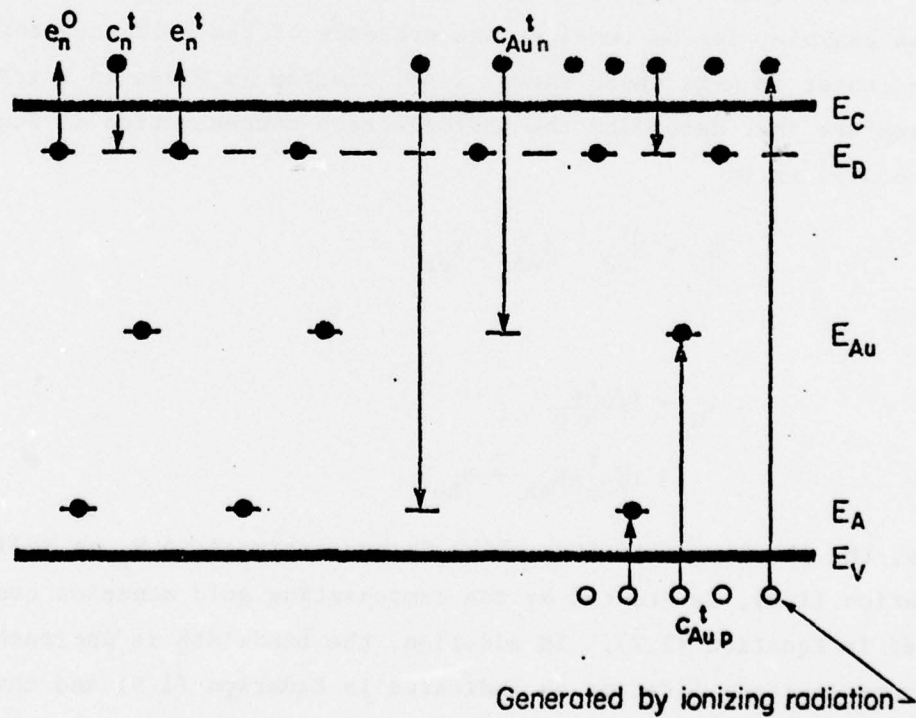


Figure 1.1.2 Energy level diagram of a n-type semiconductor doped with a shallow level acceptor with energy level E_A , a shallow level donor with energy level E_D and a deep recombination impurity, such as gold, with an energy level of E_{Au} . The transition rates are indicated next to arrows.

Here Δf is the bandwidth, A is the active detector area, $h\nu_s$ is the photon energy and c_n^t is the thermal capture rate (cm^3/sec) of electrons. In addition, the 3 d.b. bandwidth is given by

$$\omega\tau_n = 1$$

where ω is the signal frequency.

Based on these results for an ideal detector with no deep-level recombination centers, it is evident that the material parameters which limit the performance of n-type extrinsic detectors are:

- (i) Mobility of majority carriers, μ_n [see Equation (1.1)].
- (ii) Photoionization cross-section of the majority carriers, σ_n^o [see Equation (1.2)].
- (iii) Thermal capture rate of the majority carriers at the shallow level donor, c_n^t [see Equations (1.3), (1.5), and (1.6)].

In practice, deep level recombination centers are always present in the detector, either from those present in the original crystal or introduced during high temperature device fabrication processes. The presence of these deep level centers drastically affects the detector sensitivity and bandwidth. As an example, let us consider the presence of the gold acceptor recombination center in n-Si whose energy level diagram is given in Figure 1.1.2. The parameters that determine the photoelectron concentration in Equation (1.2) are now given by

$$N_D = N_{DD} - N_{AA} - N_{Au} \quad (1.7)$$

and

$$\tau_n = 1/c_n^{tp} D \quad (1.8)$$

$$= 1/c_n^t (N_{AA} + N_{Au}) \quad (1.9)$$

Thus, the photoconductivity, which is proportional to N_D as indicated in Equation (1.2), is reduced by the compensating gold acceptor centers as indicated in Equation (1.7). In addition, the bandwidth is increased by both the shorter electron lifetime as indicated in Equation (1.9) and the additional recombination of electron and hole through the gold recombination centers at a rate of $c_{Au}^t N_{Au}$, giving a total reciprocal lifetime of $\tau^{-1} = c_n^t (N_{AA} + N_{Au}) + c_{Au}^t N_{Au}$. Here c_{Au}^t is signal level dependent and reaches $c_{Au n}^t c_{Au p}^t / (c_{Au n}^t + c_{Au p}^t)$ at high levels.

Based on the analyses of the two examples just given, the objectives of this contract were delineated. They are summarized below:

(1) To study the effect of majority and minority carrier lifetimes and mobilities in the presence of recombination centers such as gold, radiation damage, thermally generated defects and others;

(2) To make use of and to extend the transient junction current and capacitance measurement techniques to determine the photoionization cross section, and thermal capture and emission rates as a function of temperature, electric field and impurity concentration at shallow and deep level impurity centers, as well as to determine the concentration profiles of these centers; and

(3) To perform theoretical calculations and interpretations of the photoionization cross sections and ion scattering mobilities using the pseudo-impurity potential models.

In addition to these original objectives, a new objective was added during the fifth year on the study of the physical mechanisms and circuit models of low-frequency 1/f noise generated at the SiO₂-Si interface states which are relevant to MOS transistors and CCD devices in image processing applications.

1.2 CONTENT

This final technical report will give a summary of those projects which have been reported as journal articles in open literature. A detailed account of unpublished results will also be given.

The work on electron and hole mobilities in silicon is given in chapter II. The following format of subsections will be followed for this and subsequent chapters. The problem statement is given in section 2.0. The experimental techniques are described in section 2.1. The experimental results are given in the subsections of section 2.2. The electron mobility is given in section 2.2.1 and the hole mobility in section 2.2.2. Theoretical analysis and interpretation are given in section 2.3. Summary and suggestions for future work are given in section 2.4.

The work on the measurements and interpretation of the properties of recombination centers is covered in chapter III. Concluding remarks are made in chapter IV.

1.3 STATISTICS

During the five-year contract period (01APR72 to 31MAR77), twelve (12) post-doctoral associates were partially supported by the contract and have contributed to the technical results reported here. The names of these associates and their current affiliations are given in Appendix A.

Twenty-one (21) graduate students were partially supported by this contract, resulting in six (6) master theses in electrical engineering, four (4) doctoral theses in electrical engineering, four (4) doctoral theses in physics, and two additional doctoral theses near completion. The names of these students, their thesis titles, degree dates and current affiliations are given in Appendix B.

There were a total of fifty-one (51) papers published in the open literature during the duration of this contract and one (1) before the date of this report. These are listed in Appendix C.

II. ELECTRON AND HOLE MOBILITIES

2.0 PROBLEM STATEMENT

We have already seen in section 1.1 that photoconductivity is directly proportional to the mobility of the majority carriers at low level. It is proportional to the sum of the mobilities of the majority and minority carriers at high level. Thus, higher photoconductivity and signal would result when mobilities are higher. However, the detector sensitivity is higher if the concentration of the optically active impurity center is higher. But large impurity concentration will reduce carrier mobility due to Coulomb scattering by the randomly located impurity ions. Thus, there is an optimum impurity concentration for maximum detector sensitivity. This optimum concentration may be further affected by three factors: (1) Maximum solubility of the impurity, (2) Position correlation of impurity atoms, and (3) Mobility in impurity bands. The first factor may make the impurity concentration at maximum sensitivity unreachable. The second factor will increase the sensitivity but is limited by fundamental thermodynamic and statistical fluctuations during the high temperature fabrication processes. The third factor is important when the impurity concentration is higher than about 10^{18} atoms/cm³. This range is important in certain

applications (e.g., emitter or bipolar transistor) but is unlikely to be very important in extrinsic detector unless substantial position correlation can be maintained to avoid impurity band when the concentrations of optically sensitive impurity centers are higher than about 10^{17} atoms/cm³.

The purpose of this study is to develop a theory that can take into account the position correlation of the scattering centers and to determine if there is any position correlation in samples prepared by conventional techniques. A new mobility measurement technique is also developed in this study.

2.1 EXPERIMENTAL TECHNIQUES

The conventional mobility determination technique gives Hall mobility. It is not possible to convert Hall mobilities into conductivity mobilities with a certainty better than a factor of 25% and often as much as 2 due to the unknown temperature and energy dependences of the scattering mechanisms. The problem lies in the measurement of the carrier concentration, N, when calculating the mobility from the measured conductivity, σ ,

$$\mu_n = \sigma/qN .$$

Hall coefficient measurement gives a carrier concentration which is subject to the large uncertainty discussed above. An alternative technique is developed to measure the carrier concentration, using the capacitance-voltage characteristics of a reverse biased Schottky barrier diode.[3] However, this method is subject to some uncertainty at high impurity ion concentrations and at low temperatures due to impurity deionization effect.[4] What is measured from the C-V curves is the total net impurity concentration (donor minus acceptor) and not the carrier (electron) concentration. Unless all the impurities are ionized, $N = N_{DD} - N_{AA}$ does not hold but $N < N_{DD} - N_{AA}$ so that the calculated mobility would be higher than the true mobility.

2.2 EXPERIMENTAL RESULTS

The C-V technique is employed to obtain the hole mobility in p-type silicon and this is reported in section 2.2.1. Experimental data of electron mobility are obtained from the open literature which are mostly Hall mobility or effective conductivity mobility without the correction for the deionization and impurity band effects.

2.2.1 HOLE CONDUCTIVITY IN p-Si

The results were reported in two published papers. The experimental technique and the detailed results were given by Tsao and Sah.[3] The analyses made by Woodley and Sah, including the deionization effect, are summarized in Table 1 and Figures 2.2.1, 2.2.2, 2.2.3, and 2.2.4.[4] The effect of deionization on the hole concentration calculated from the C-V data is shown in Figure 2.2.1 where the dots are the net impurity concentration and the solid curves are the hole concentrations for five p-Si samples investigated whose net ionized impurity concentration is shown in Table 1. The corrected (solid curves) and uncorrected (dots) mobilities for two samples are shown in Figure 2.2.2 as a function of temperature. The corrected mobilities with deionization taken into account are shown in Figure 2.2.3 for all six samples where the lattice scattering mobility is also shown by the dashed curve. A comparison of the room-temperature hole conductivity mobility as a function of boron impurity concentration obtained in this work with those of Irvin [5] is given in Figure 2.2.4. The present data, after making the deionization correction, compares favorably with our previously unpublished data while it deviates significantly from the frequently used Irvin curve.

2.2.2 ELECTRON MOBILITY IN n-Si

The data of the electron mobility were collected from open literature. Most of these are Hall mobilities, e.g., the electron concentration is calculated from the Hall coefficient data. Some of the mobilities at very high impurity concentrations are obtained by assuming that the electron concentration is equal to the majority impurity (phosphorus or arsenic) concentration. The mobility due to ion scattering alone was then computed from the Matthiessen rule

$$1/\mu_I = 1/\mu_{\text{Experimental}} + 1/\mu_L$$

where the lattice scattering mobility, $\mu_L = 1330 \text{ cm}^2/\text{V-S}$ at 300°K, is the experimental mobility asymptotically extrapolated to low ion concentration. These experimental results are given in Figure 2.2.5 at 300K and Figure 2.2.6 at 77K.

2.3 THEORETICAL ANALYSIS AND INTERPRETATION

The conventional theories of ion scattering (Brook-Herring and Conwell-Weisskoff formulae) are based on the model of a completely random distribution

Table 1
Impurity Concentration of p-type Silicon

Device	$N_{AA} - N_{DD}$ (cm^{-3})
68C24	9.71×10^{14}
7412	5.52×10^{15}
7645	1.06×10^{16}
7735	2.27×10^{16}
7914	2.79×10^{16}
8053	4.71×10^{16}

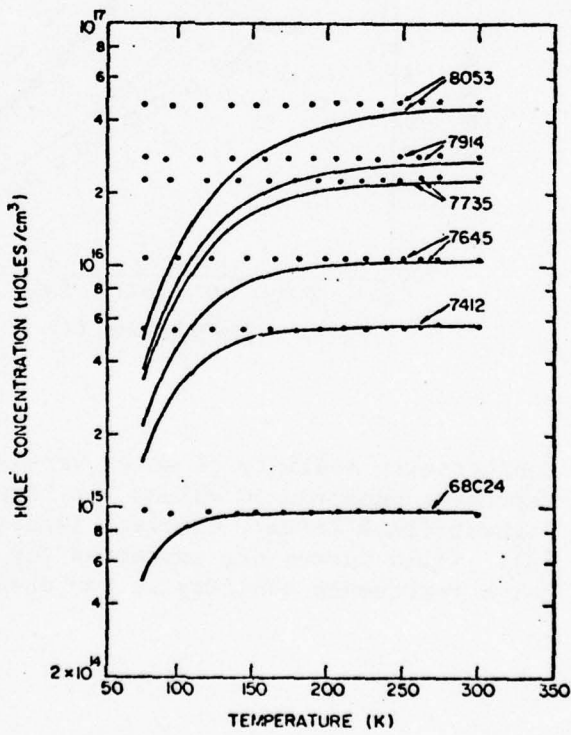


Figure 2.2.1 Ionized impurity and hole concentrations versus temperature for devices used in [3]. Dots are values of impurity concentration obtained from C-V measurements. Solid curves are hole concentration corrected for deionization effects.

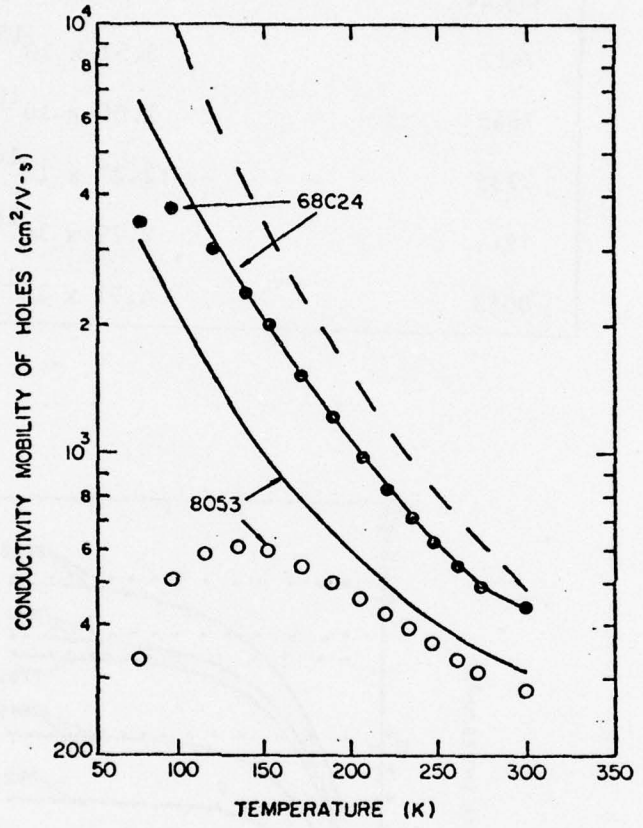


Figure 2.2.2 Conductivity mobility of holes versus temperature. Points represent uncorrected values for lowest (10^{15} B/cm³, dots) and highest (1×10^{16} B/cm³, circles) impurity concentrations used in [3]. Solid curves are corrected for deionization effects. Dashed curve represents mobility in the absence of impurity scattering.

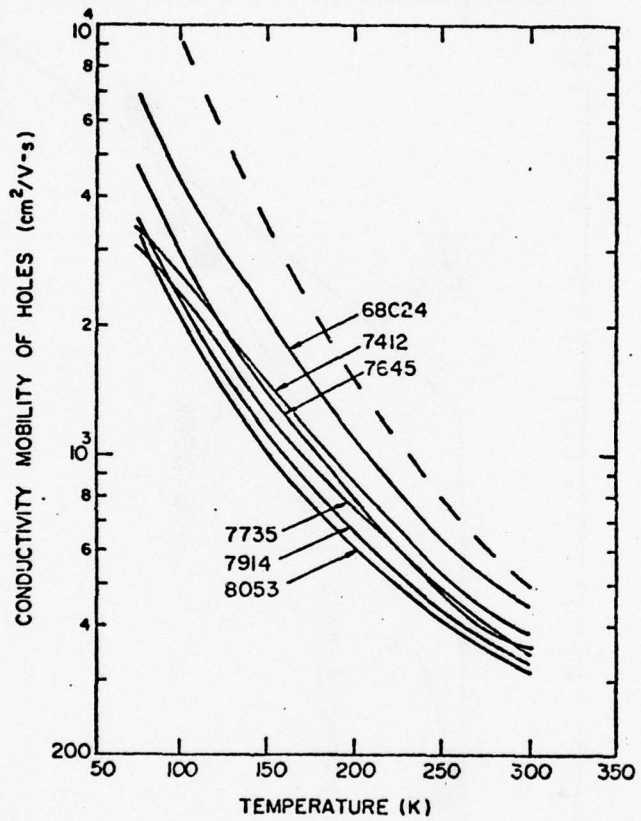
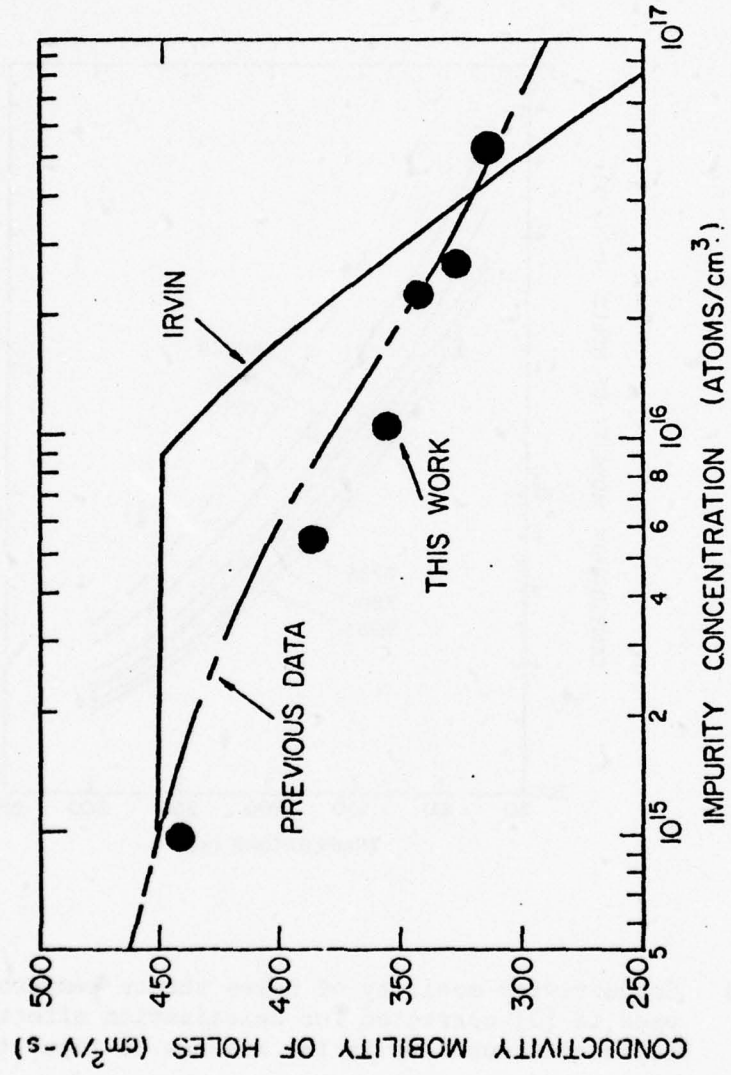


Figure 2.2.3 Conductivity mobility of holes versus temperature for devices used in [3] corrected for deionization effects. Dashed curve represents mobility in the absence of impurity scattering.



Conductivity mobility of holes versus impurity concentration at room temperature. Results of this work (points) compared to values calculated from fits to published resistivity versus impurity concentration data by Irvin [5] (solid curve) and previous data used by Sah (dashed curve). The estimated accuracy is about 15%.

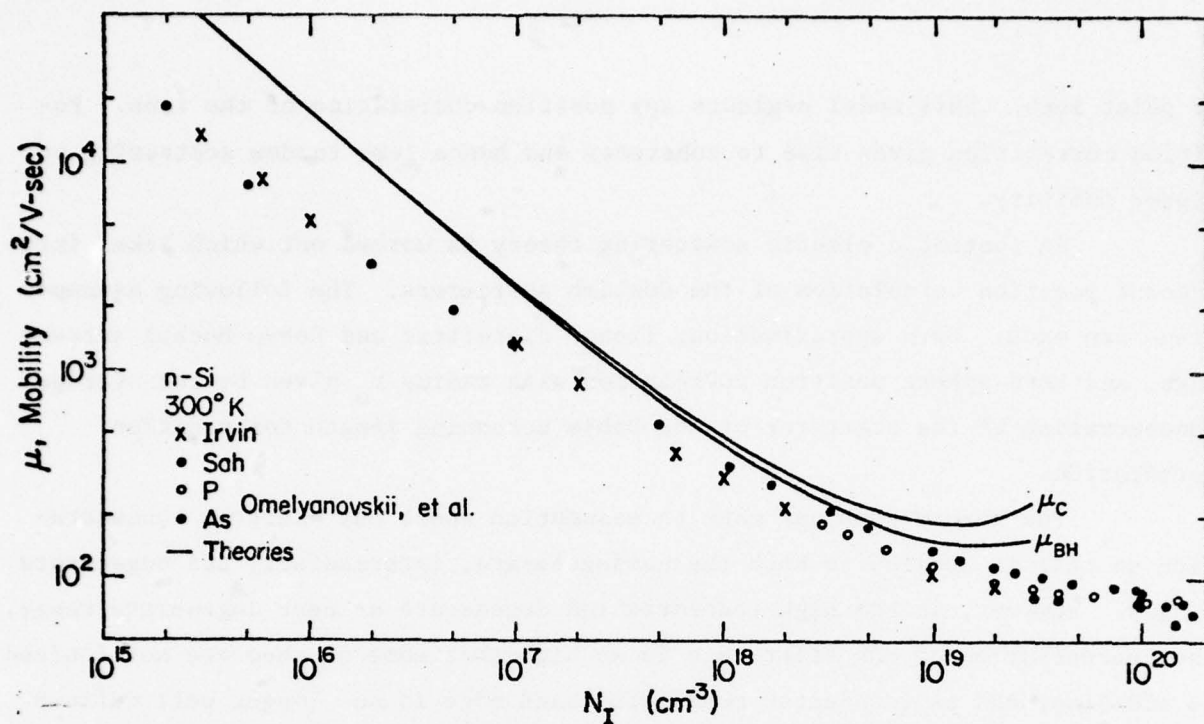


Figure 2.2.5 Theoretical ionized impurity scattering electron mobilities in silicon at 300°K as a function of ion concentration. μ_{BH} is the Brook-Herring theory without any ion position correlation and μ_C is the Brook-Herring theory modified to include ion position correlation. Debye-Hückel screening at 800°K is assumed for ion position correlation.

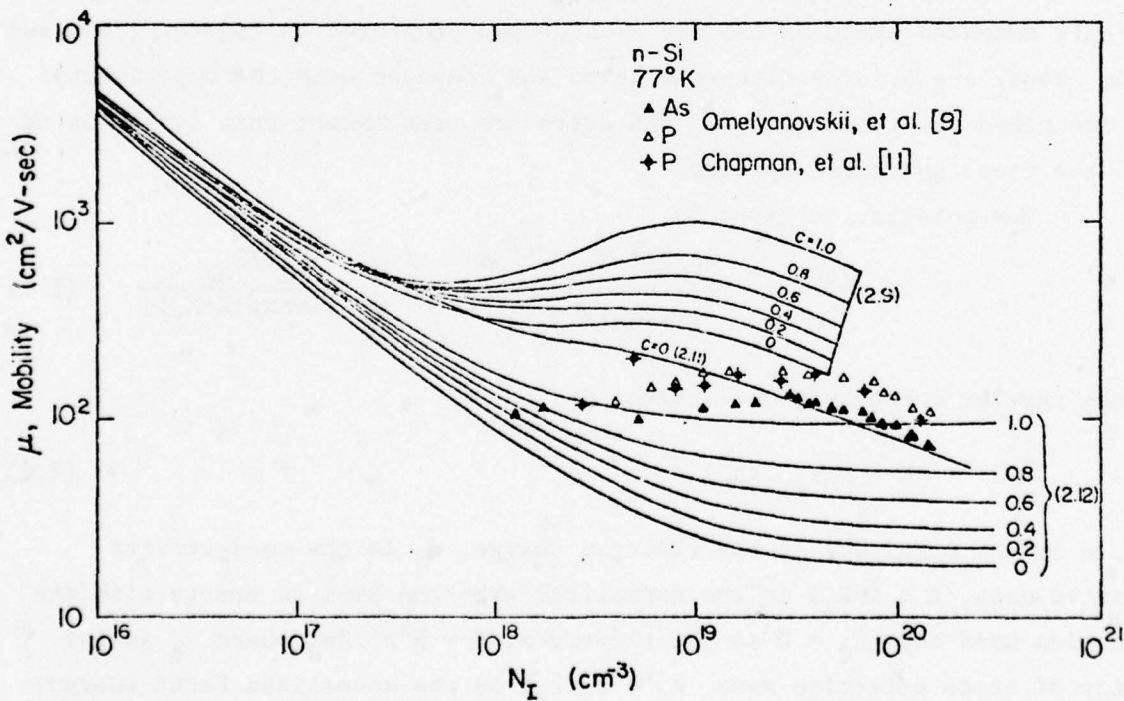


Figure 2.2.6 Theoretical ionized impurity scattering electron mobility in silicon at 77°K as a function of ion concentration. Hard sphere ion position correlation is assumed and electron screening given by equations (2.9), (2.11) and (2.12) are used.

of point ions. This model neglects any position correlation of the ions. Position correlation gives rise to coherency and hence less random scattering or higher mobility.

An isotropic elastic scattering theory is worked out which takes into account position correlation of the Coulomb scatterers. The following assumptions are made: Born approximation, linear dielectric and Debye-Huckel screenings, and hard sphere position correlation with radius r_0 given by the average concentration of the scatterer or the Debye screening length for position correlation.

The theory does not make an assumption about the electron concentration so that it applies to both the nondegenerate, intermediate, and degenerate ranges. However, in the high concentration degenerate or near degenerate range, the concentration of the scatterers is so high that some of them are not ionized. In addition, the semiconductor conduction band edge is no longer well defined and impurity band conduction may not be negligible. These factors are not taken into account so that the theory is not reliable in the high concentration range.

The result of the theory is given below and a family of curves is numerically computed using an IBM 360 machine and presented in Figures 2.2.5 and 2.2.6. These are briefly discussed below and compared with the experimental data described in section 2.2.2. MKS units are used except that length is in cm in the final numerical results.

The mobility is given by

$$\mu = \frac{2e}{3m_c} \left/ \int_0^{\infty} \frac{x \exp(x-x_F) x^{3/2} dx}{[1+\exp(x-x_F)]^2} \right/ \int_0^{\infty} \frac{x^{1/2} dx}{[1+\exp(x-x_F)]} \quad (2.1)$$

and the carrier concentration is given by

$$N = N_C F_{1/2}(x_F) \quad (2.2)$$

Here, e is the magnitude of the electron charge, m_c is the conductivity effective mass, $X = E/k_B T$ is the normalized electron kinetic energy with the conduction band edge $E_C = 0$ as the reference, $E = \hbar^2 k^2 / 2m_d$ where m_d is the density of state effective mass, $x_F = E_F/k_B T$ is the normalized Fermi energy, $N_C = (g_v / 4\pi^3) (2\pi m_d k_B T / \hbar^2)^{3/2}$ is the effective density of state, g_v is the number of conduction band valley and $F_S(x_F)$ is the Fermi-Dirac integral of the S-th order defined by

$$F_S(X_F) = \frac{1}{S!} \int_0^{\infty} \frac{x^S dx}{[1+\exp(X-X_F)]} \quad (2.3)$$

whose derivative is

$$F'_S(X_F) = dF_S/dX_F = F_{S-1}(X_F) \quad (2.4)$$

The reciprocal momentum relaxation time due to isotropic elastic Coulomb scattering of electrons by a partially random (finite position correlation) ion charge density inhomogeneity $n_i(X)$ is given by

$$\frac{1}{\tau(k)} = \frac{8\pi e^4 m_d k}{k^3} \int_0^{\pi} \frac{(1-\cos\theta)\sin\theta d\theta}{\epsilon^2(q)q^4} \langle n_i(q)n_i^*(q)v \rangle \quad (2.5)$$

Here, \vec{k} is the wave vector of the incident electron wave and the scatterer electron wave vector is $\vec{k}+\vec{q}$. Since the scattering is elastic, $|k| = |\vec{k}+\vec{q}|$ or $q = 2k \sin(\theta/2)$ where θ is the scattering angle $/\vec{k}+\vec{q}, \vec{k}$. Planewave or orthogonalized planewave representation of the electron wavefunction is used.

The dielectric function $\epsilon(q)$ contains two parts: $\epsilon(q) = \epsilon_v(q) + \epsilon_c(q)$ where $\epsilon_v(q)$ comes from dielectric screening of the ion charges by the valence band electrons and $\epsilon_c(q)$ from Debye screening by the conduction band electrons.

$\epsilon_v(q)$ is nearly given by the static dielectric constant [$\epsilon_v(0) \approx \epsilon_0 = 11.7 \times 8.85 \times 10^{-14}$ F/cm for silicon] since the dominant scattering events off a Coulomb scatterer are small angle scattering $\theta \approx 0$ and in nondegenerate or near degenerate semiconductors, $k \ll 2\pi/a$ where 'a' is the lattice constant. If it is necessary to consider large q events, $\epsilon_v(q)$ can be readily obtained from band theory calculations which are now available. It has the approximate form of

$$\epsilon_v(q) = 1 + (\epsilon_0 - 1)[1 + (q^2 + 2\vec{q} \cdot \vec{G} - 2\vec{q} \cdot \vec{k} + 2\vec{k} \cdot \vec{G})/G^2]^{-2} \quad (2.6)$$

where \vec{G} is a reciprocal vector of the lattice. This shows that $\epsilon_v(q) \approx \epsilon_0$ at $q \rightarrow 0$ or $q \ll G$ and $\epsilon_v(q) \rightarrow 1$ when $q \gg G$.

The Debye screening function, $\epsilon_c(q)$, from conduction band electron has an explicit form in the linear screening theory given by [6]

$$\epsilon_c(q) = \epsilon_0 (q_D/q)^2 \quad (2.7)$$

where the square of the Debye-Hückel-Thomas-Fermi screening wave number, q_D^2 , or the reciprocal Debye screening length $\lambda_D^{-2} = q_D^2$ is given by [7,8]

$$q_D^2 \rightarrow (e^2 / \epsilon_0 k_B T) N \quad X_F < -3 \quad (2.9)$$

$$\rightarrow (e^2 m_d / \pi \epsilon_0 \hbar^2) (3N/\pi)^{1/3} \quad X_F > 3 \quad (2.10)$$

If large q scattering cannot be neglected, an explicit form of q_D^2 is given by [6]

$$q_D^2 = [e^2 N / (2E_F / 3)] \left\{ \frac{1}{2} + \frac{4k_F^2 - q^2}{8k_F q} \ln \left| \frac{2k_F + q}{2k_F - q} \right| \right\} \quad (2.11)$$

where $E_F = \hbar^2 k_F^2 / 2m_d$ and $k_F = (3\pi^2 N / g_v)^{1/3}$.

One of the problems associated with the theory of screening of the ion charge by conduction electrons is the number of electrons in a Debye sphere of radius q_D^{-1} or Debye screening length, $\lambda_D = q_D^{-1}$. Evidently, the screening concept breaks down if there are few electrons in a Debye sphere. Thus, an alternative form for q_D^{-1} or λ_D is to take it as the average inter-conduction-band-electron spacing

$$\lambda_D = q_D^{-1} = (3/4\pi N)^{1/3} \quad (2.12)$$

This would be the lower limit of λ_D below which the simple screening model is no longer meaningful.

In (2.5) V is the volume of the crystal. $n_i(q)$ is the Fourier transform of $n_i(\vec{r})$ which is given by $n_I(\vec{r}) - N_I$ where $n_I(\vec{r})$ is the local density of the ion scatterers while $N_I = \langle n_I(\vec{r}) \rangle$ is the average ion density. $\langle \rangle$ is the ensemble average over all configurations of ion density distribution. $\langle \rangle$ could also be evaluated in the original form of a double sum of $\exp[iq \cdot (\vec{R}_i - \vec{R}_{i'})]$ over all \vec{R}_i ion coordinates. For the hard sphere model in which it is assumed that no two ions can be closer than a distance of r_o , then

$$\langle n_i(q) n_I^*(q) V \rangle = N_I [1 - 3V_o N_I (\sin qr_o - qr_o \cos qr_o) / (qr_o)^3] \quad (2.13)$$

where V_o is the hard sphere volume given by $V_o = 4\pi r_o^3 / 3$. The product $V_o N_I = C$ is the ion position correlation factor in the hard sphere model. When $C=1$, we have

$$V_o = 1/N_I$$

and

$$r_o = (3/4\pi N_I)^{1/3}$$

is the closest approach in the hard sphere model. The appropriate value of C for a particular sample depends on the condition (such as temperature and time of diffusion and drift) under which the impurity ions are introduced during the high temperature fabrication processes. C is only a qualitative measure since in an actual case, the exact distribution of the inhomogeneity probably differs from the hard sphere model.

To get a more realistic model, the linear screening theory is also applied to the ion distribution at the oxidation, diffusion or crystal growth temperature, T_o , at which the ions are introduced. For this case,

$$\langle n_i(q)n_i^*(q)\rangle = N_I \{1 - q_{oI}^2 / [q^2 + \sum_\alpha q_{o\alpha}^2]\} \quad (2.14)$$

where $q_{oI}^2 = (e^2 N_I / \epsilon_o k_B T_o)$ and $q_{o\alpha}^2 = e^2 N_\alpha / \epsilon_o k_B T_o$. N_α is the average concentration of the α -th species (α = donor ion, acceptor ion, electrons and holes) and ϵ_o is the static dielectric constant at the impurity ion introduction temperature T_o .

Numerical calculations are carried out using an IBM 360 machine. C is taken as the constant parameter and N_I is assumed equal to N in (2.11) in order to get a r_o which is valid only if all the impurity atoms are ionized. $\epsilon_v(q) = \epsilon_v(0) = \epsilon_o$ is assumed in (2.6) which is a good approximation since only small q scattering events are important.

Families of curves are computed for two temperatures to illustrate the magnitude of the correlation effect. For mobility at 300°K, given in Figure 2.2.5, the nondegenerate Debye-Hückel screening given by (2.9) is used for both $\epsilon_c(q)$ in (2.7) and ion position correlation given by (2.14). A "fabrication" temperature of $T_o = 800^\circ K$ is assumed where $p_o = n_o = 10^{17} \text{ cm}^{-3}$. $m_c = m$ and $m_d = 0.323m$ are used. The results are shown in Figure 2.2.5. μ_{BH} is the Brook-Herring theory without ion position correlation, i.e., $\langle n_i(q)n_i^*\rangle = N_I$, and μ_C is that with correlation given by (2.14). The nondegenerate approximation breaks down at an electron concentration of $N = N_{DD} \approx N_C = 2.8 \times 10^{19} \text{ cm}^{-3}$. The ion scattering mobility in Figure 2.2.5 are calculated from $\mu_I = (\mu_{data}^{-1} - \mu_L^{-1})$ where $\mu_L = 1330 \text{ cm}^2/\text{V-S}$ and μ_{data} are taken from (i) recent Hall mobility data of Omelyanovskii, Fistful and Milvidskii [9], (ii) Irvin's resistivity curve [5], and (iii) a conductivity v.s. impurity concentration curve obtained by Sah in 1959 which was fitted to all the published data up to that date [10].

Two points may be noted: (1) The two theoretical curves show little effect of correlation at impurity concentration less than about 10^{18} cm^{-3} and

correlation gives only about 1.5 times higher mobility ($\mu_C \approx 1.5\mu_{BH}$) at $N_{DD} = 2 \times 10^{19} \text{ cm}^{-3}$, and (2) the experimental data slightly favors the Brook-Herring model, μ_{BH} , which contains zero correlation. The latter is expected since the impurity ions are introduced into these samples during crystal growth ($\approx 1420^\circ\text{C}$) where the electron concentration is so high that all long range correlation effects are screened out.

Theoretical calculations are also made at 77K and are shown in Figure 2.2.6 and compare with some experimental data in open literature. [9,11] The hard sphere model, given by Equation (2.13), for ion position correlation is used. Three screening models are used in the theory which are given by Equations (2.9), (2.11), and (2.12).

The theoretical curves of $C = 0, 0.2, 0.4, 0.6, 0.8$, and 1.0 labeled (2.9) in Figure 2.2.6 use the nondegenerate Debye-Hückel screening model given by Equation (2.9).

The single theoretical curve labeled (2.11) in Figure 2.2.6 uses the degenerate Thomas-Fermi screening model given by Equation (2.11). This is included to illustrate the effect of large q scattering.

The third family of curves with $C = 0, 0.2, 0.4, 0.6, 0.8$, and 1.0 and labeled (2.12) in Figure 2.2.6 uses the average interconduction electron spacing, given by Equation (2.12) as the screening length. It is included again only as an illustration since this model does not include the long range property of the Coulomb force in the electron-electron interaction and hence underestimates the screening effect, resulting in lower mobilities.

The comparison of the theoretical results given by Equation (2.9) with the experimental data of Omelyanovskii [9] and Chapman, Tuft, Zook and Long [11] again favor the zero position correlation model ($C=0$).

The theory, given by curves labeled (2.9) in Figure 2.2.6, does show that if substantial ion position correlation can be achieved, such as $C=1$, then the mobility can be increased by a factor of four over that of a completely random ion distribution at an ion scatterer concentration of $N_I = 10^{19} \text{ ions/cm}^3$.

2.4 SUMMARY AND SUGGESTIONS

A new conductivity mobility measurement technique was introduced in which the carrier concentration is determined from capacitance-voltage measurements on Schottky barrier diodes. This method does not have the uncertainty inherent in the Hall effect measurement of the carrier concentration due to the

unknown scattering properties. However, the C-V curve gives the net ionized impurity concentration rather than the carrier concentration. Thus, a theoretical correction of the amount of impurity ion deionization must be made. This correction is negligible at room temperature and low impurity concentration but becomes appreciable at low temperatures and high impurity concentrations.

The hole mobility data obtained from the C-V technique shows that the currently accepted values due to Irvin are significantly in error at impurity concentrations above 10^{15} Boron/cm³ at room temperature where a small impurity deionization effect can be corrected accurately in our data.

Additional experimental work using the Schottky barrier C-V techniques appears desirable for p-type as well as for n-type silicon, the latter not studied during this contract, in order to obtain a reliable set of conductivity mobility versus impurity concentration curves over the practical temperature range of -55°C to 125°C and the theoretically interesting range of 4°K to 400°K. These data would provide further insight into the scattering model and the possibility of position correlation effects which would give high mobility due to reduced random ion scattering as well as high detector sensitivity. The more reliable data would also stimulate additional detailed theoretical work in the mathematical description of the scattering models using impurity pseudo-potential theory.

Further studies also appear desirable to determine the experimental methods and conditions to give large ion position correlation. Large ion position correlation would reduce scattering and hence permit the use of materials with high concentrations of optically sensitive impurity ions to achieve high infrared detector sensitivity as well as high mobility which further improves photo signal.

III. PROPERTIES OF IMPERFECTION CENTERS IN SILICON

3.0 PROBLEM STATEMENT

It was shown in section 1.1 that the fundamental parameters which characterize optically active impurity or defect centers for detector applications are the thermal capture and emission rates of electrons and hole, c_n^t , e_n^t , c_p^t , and e_p^t ; the thermal activation energies, $E_C - E_T$ and $E_T - E_V$; and the

photoionization rate or the optical emission rates of electrons and holes, e_n^o and e_p^o or their corresponding photoionization cross sections, σ_n^o and σ_p^o . In addition, the concentration of the optically sensitive centers directly affects the detector sensitivity.

The detector sensitivity and bandwidth are also affected by the presence of deep level recombination centers in the semiconductor detector material or device structures. The most important parameters for these deep levels are the thermal capture and emission rates, thermal activation energies and concentrations which were listed above for the optical sensitive centers.

These parameters were illustrated in the energy level diagrams in Figures 1.1.1 and 1.1.2.

Although many experimental studies have been made on the energy level positions of the imperfection centers in silicon, neither precise data on energy level nor on the kinetic capture and emission rate parameters indicated above are available. These parameters are essential in determining the optimum detector performance.

The purpose of the studies undertaken in this project was to apply the transient capacitance techniques to obtain the precise values of these parameters for potentially useful optical centers and the process introduced impurity and defect recombination centers under a wide range of temperature, electric fields, and optical spectra.

The transient capacitance techniques have been reviewed in seven invited lectures given by C. T. Sah.[12-18] The texts of these lectures are published in four papers in the open literature with emphasis on different application aspects.[12,15,18,19]

During this five-year study, important and powerful extensions of the transient capacitance techniques have been developed. In addition, extensive applications of the transient capacitance technique were also made to study the diffusion and generation-annealing kinetics of the deep level centers.

3.1 EXPERIMENTAL TECHNIQUES

The transient capacitance techniques, first extensively used by Sah and his students since 1965 [12], have been extended and improved. These techniques include [18,19] the *Voltage Stimulated Capacitance* (VSCAP), previously known as the dark capacitance transient; the *Thermally Stimulated Capacitance*

(TSCAP); and the *Light Stimulated Capacitance* (LSCAP), previously known as the photocapacitance. These, together with material preparation (growth of impurity-doped crystal) and on-line computer control of experiments and analysis of experimental data are described in this section.

3.1.1 EDGE EFFECT IN TSCAP

Electrons and holes trapped at an impurity or defect center in the edge region of the junction space charge region can give rise to a change in the high-frequency capacitance of the junction when the trapped electrons and holes are released either thermally by increasing the sample temperature or optically with a monochromatic light. The effect was first discovered and used by Walker and Sah in 1973 [20] and it was shown that one can observe energy levels as shallow as 60 meV from a band edge during heating from 77K to 300K in a TSCAP experiment. On the other hand, the VSCAP method which is used to discharge or charge the traps in the space charge region, can only reach levels no shallower than about 150 meV from one of the two band edges at 77K. Thus, the edge effect TSCAP provides a convenient method to determine the presence of shallow levels in the band gap without having to use a liquid helium dewar. However, temperatures lower than 77K is still needed to obtain the kinetic parameters of very shallow levels, i.e., the capture and emission rates, using the VSCAP or LSCAP methods.

The theory of the edge-effect TSCAP was carefully verified experimentally by Wang [21]; in particular, the dependences of the magnitude of the capacitance change on reverse bias voltage was verified. Wang also applied the method to determine the thermal activation energy of electrons trapped at the Bi level in silicon, which is reported in the subsection on Bi in this chapter.

3.1.2 EDGE EFFECT IN VSCAP

In the original theory of the voltage stimulated capacitance (VSCAP) or dark transient capacitance of a p/n junction described in our 1970 paper [22], the staircase depletion approximation was made for the junction space charge region. For many applications, this approximation was found to be inadequate because of the contributions from the edge region. Two of the situations in which the edge effect becomes important are investigated. This subsection describes one of these: the edge effect at low reverse bias in profiling the impurity concentrations.

A detailed theoretical analysis was undertaken by Sah and Neugroschel in 1975 [23] to provide a first order theory of the contribution of the edge region. With such an extension of the theory, impurity profiles within 0.25 micron from the metal-semiconductor interface of a Schottky barrier or the junction boundary of a p+/n junction can be obtained with good reliability. The impurity concentration profiles are obtained from the total transient capacitance change with reverse bias voltage. In order to get the concentration profile near the junction interface, VSCAP data at low reverse or even small forward bias are needed. The effect of the edge region is large at low reverse bias voltage and it significantly reduces the computed variation of the impurity concentration with position from the depletion theory which completely neglects the edge region.

The first order theory has been further improved by Marchand [24], which removed the approximation of constant impurity concentrations in the edge region used by Sah and Neugroschel [23]. The improved theory is now used routinely in a computer program to evaluate the shallow and deep level impurity concentration profiles in silicon.

Further improvement of the theory, including the Debye length in the quasi-neutral region, will be made to complete the theoretical development.

3.1.3 CAPTURE RATE BY VSCAP IN THE EDGE REGION

The effect of incomplete filling of the traps which were subsequently emptied to give the VSCAP was first observed as a filling time dependence of the total VSCAP. This phenomenon has recently been analyzed in detail and the theory verified with experimental data by Marchand. [24] It provides a powerful new method of measurement of the thermal capture rate of electrons and holes in the edge region where the electric field is low. A proper asymptotic expansion of the theory can give the zero-field or near-thermal equilibrium capture rates from the experimental data. The thermal equilibrium capture rates are the parameters necessary to compute the carrier recombination lifetimes.

3.1.4 SERIES RESISTANCE EFFECT IN VSCAP MEASUREMENTS

At low temperatures, the series resistance of the quasi-neutral region and the edge layer of a p/n junction or Schottky barrier space charge region will greatly affect the transient capacitance measurements. A detailed investigation of the series resistance effect was undertaken by Woodley [25], who

divided the edge region of the space charge layer of the junction into several lumps. Each lump is represented by an RC parallel equivalent circuit model. The small-signal capacitance and conductance versus temperature, frequency and junction reverse bias voltage are obtained and compared with the lump circuit models. Excellent agreement has been obtained at 24K as indicated in Figure 3.1.1 using one RC lump for the edge region. By including such a model, the transient capacitance data at very low temperatures can now be reduced to give the emission and capture rate constants at the shallow level centers.

3.1.5 SAMPLE PREPARATION

Two unconventional as well as a number of conventional device fabrication techniques were developed to give the desired samples for studying the properties of shallow and deep levels in silicon. One of the two unconventional methods was the development of crystal growth and doping techniques to provide silicon crystals which are doped with a shallow and a deep level impurity. The *doubly* doped crystal of most concern to this study was the silicon crystal doped with both phosphorus and bismuth with the latter at a lower concentration to study the thermal capture and emission and optical emission of electrons trapped at the Bi center. The second development was the successful search for a metal which would provide a good rectifying Schottky barrier on p-type silicon from 77 to 300K. After trials with many impurities, it was found by Tsao that Mg gives a very good Schottky barrier even at room temperature.[3] Encapsulation or storage in inert ambient was found to be necessary to prevent deterioration of the Mg on p-Si Schottky barrier.

3.1.6 ON-LINE COMPUTER CONTROL AND ANALYSIS OF EXPERIMENTS

During the five-year contract period, two generations of minicomputer equipment were installed and put into operation for on-line control and analyses of experiments. The on-line computer approach is necessary to relieve the point by point data recording and analysis methods, which are tedious, time-consuming, and frequently prone to human error.

The first generation (acquisition began in 1970) automatic data acquisition and analysis equipment put into operation in our laboratory was a programmable desk calculator (Wang 720C) with a 500K Byte disc and a printer-plotter terminal. Part of the A/D and D/A interface cards as well as the entire

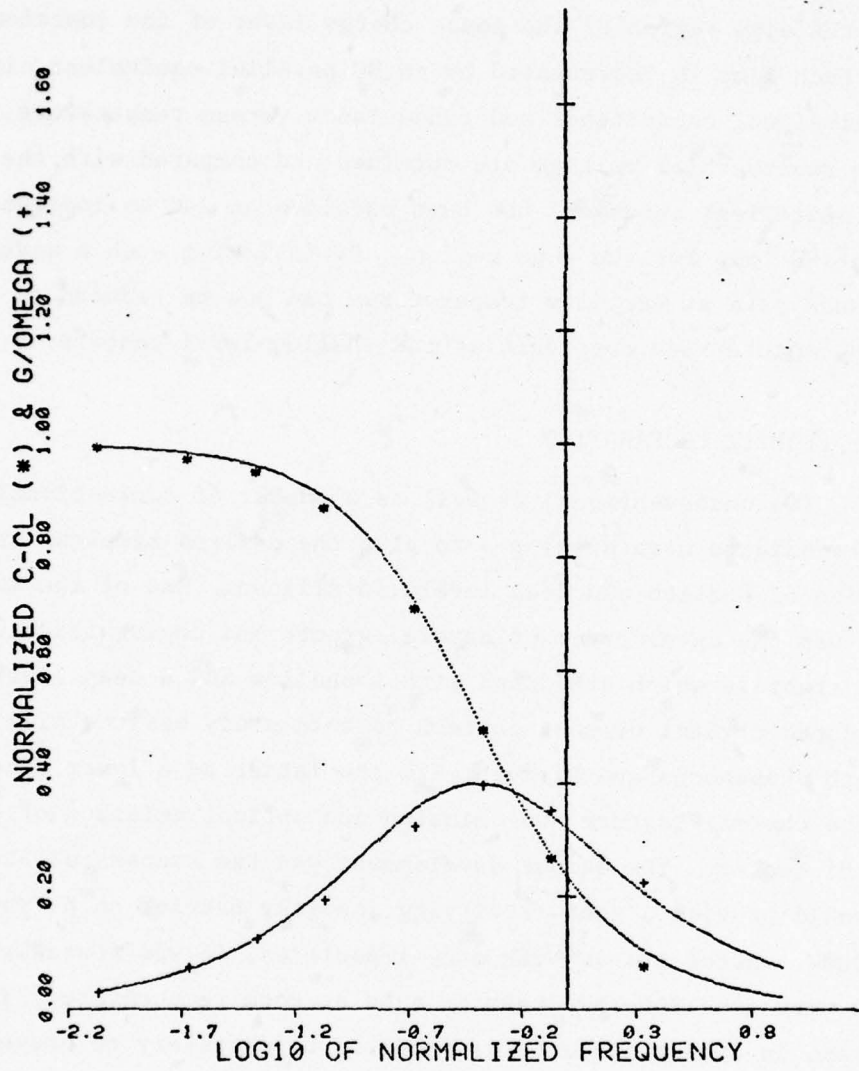


Figure 3.1.1 Normalized frequency dependence of C and G/W of device 96D1p5 at 2 volts reverse bias and 23.9K. Fit is for $C_W=16.421\text{pF}$, $L/W=39.92$, $\tau_d=8.63\times 10^{-8}$ sec and $X-W=3.97\times 10^{-3}$ cm.

measurement control circuits were designed and built by T. Y. Lo from scratch, which is reported in his doctoral thesis. After successfully installing and operating this system, it became evident that further development of the application programs of this system was impractical due to the extremely long time (\approx one year and four graduate students) required to write and debug a program. This drawback came from the low-level calculator language used by the Wang 720C computer and it was further exemplified by the limited disk storage available.

A second generation minicomputer-controlled data acquisition and analyses system was selected to provide both high level language (FORTRAN IV), multiprogramming-multiuser and comprehensive instrument-control capabilities. A Hewlett-Packard 21MX minicomputer system was purchased with a 5M Byte disk, a 45 ips tape drive, and a Versatec printer-plotter. A number of instrumentation interfaces have been or are being added to control digital voltmeters and d.c. power supplies. An Intel 8080 microcomputer was also designed and built by T. Y. Lo to serve as a stand-along data collection terminal but programmed by the HP21MX minicomputer in FORTRAN IV. This microcomputer will enable us to free the minicomputer for other tasks while a long-duration experiment is being run by the microcomputer.

3.2 EXPERIMENTAL RESULTS

Experimental measurements of the thermal emission and capture rates and optical emission rates are described for phosphorus centers, bismuth centers, thermally generated centers, impurity centers from the Boron+ source, gold centers and a number of other impurity centers (Ag, Co, Cr, S, Ta and Zn).

3.2.1 PHOSPHORUS

The phosphorus energy level and the thermal emission rate are measured by the transient capacitance method while the energy level was also obtained from conductance measurements of a N+/N/N+ diode. The conductance data from 20 to 33K was obtained by Ning and Fu (Figure 3.2.1) and fitted to the Arrhenius equation $G = A \exp(-\Delta E/kT)$ and to give a thermal activation energy of $E=42$ meV. The difference between this and other thermal and optical energy measurements which gave 44 meV was probably due to the inaccuracy in our temperature calibration and measurements. The conductivity measurement is a classical method and can give accurate thermal activation energy at thermal equilibrium or zero

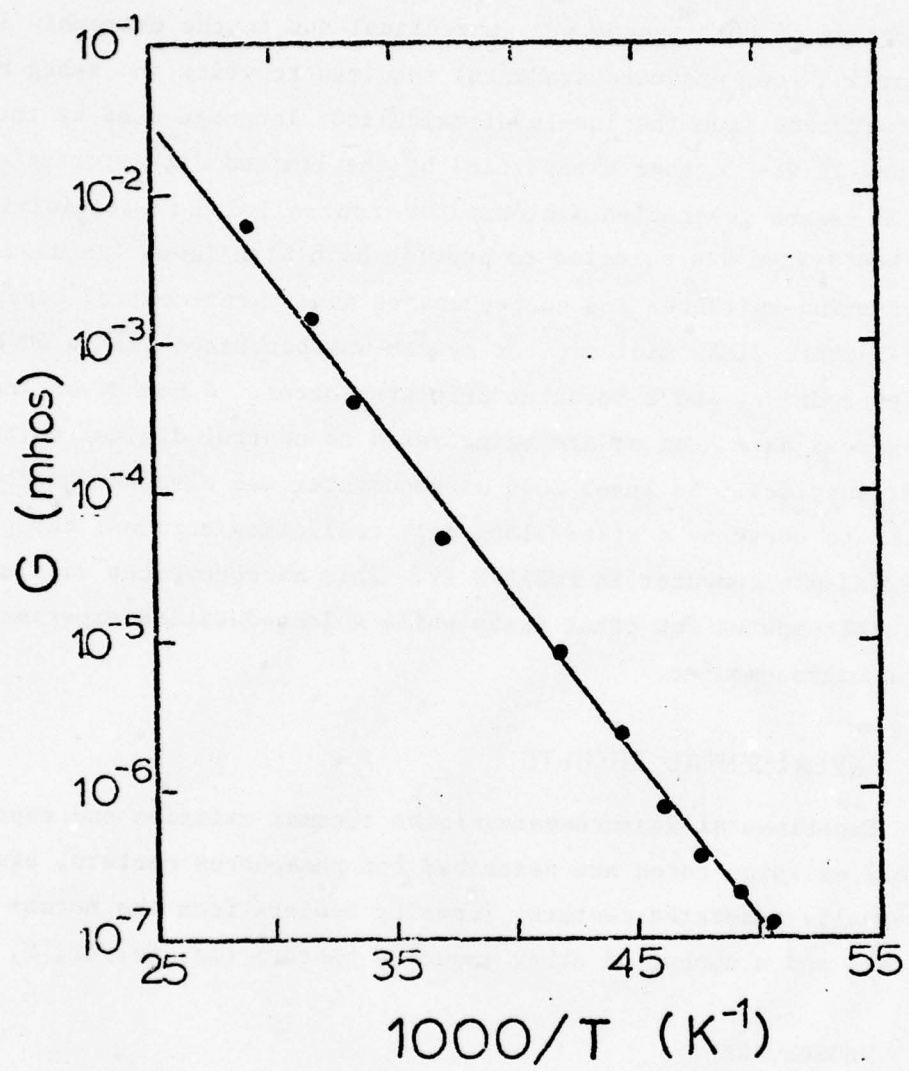


Figure 3.2.1 The conductance of a $n+/n/n+$ phosphorus-doped silicon diode as a function of reciprocal temperature.

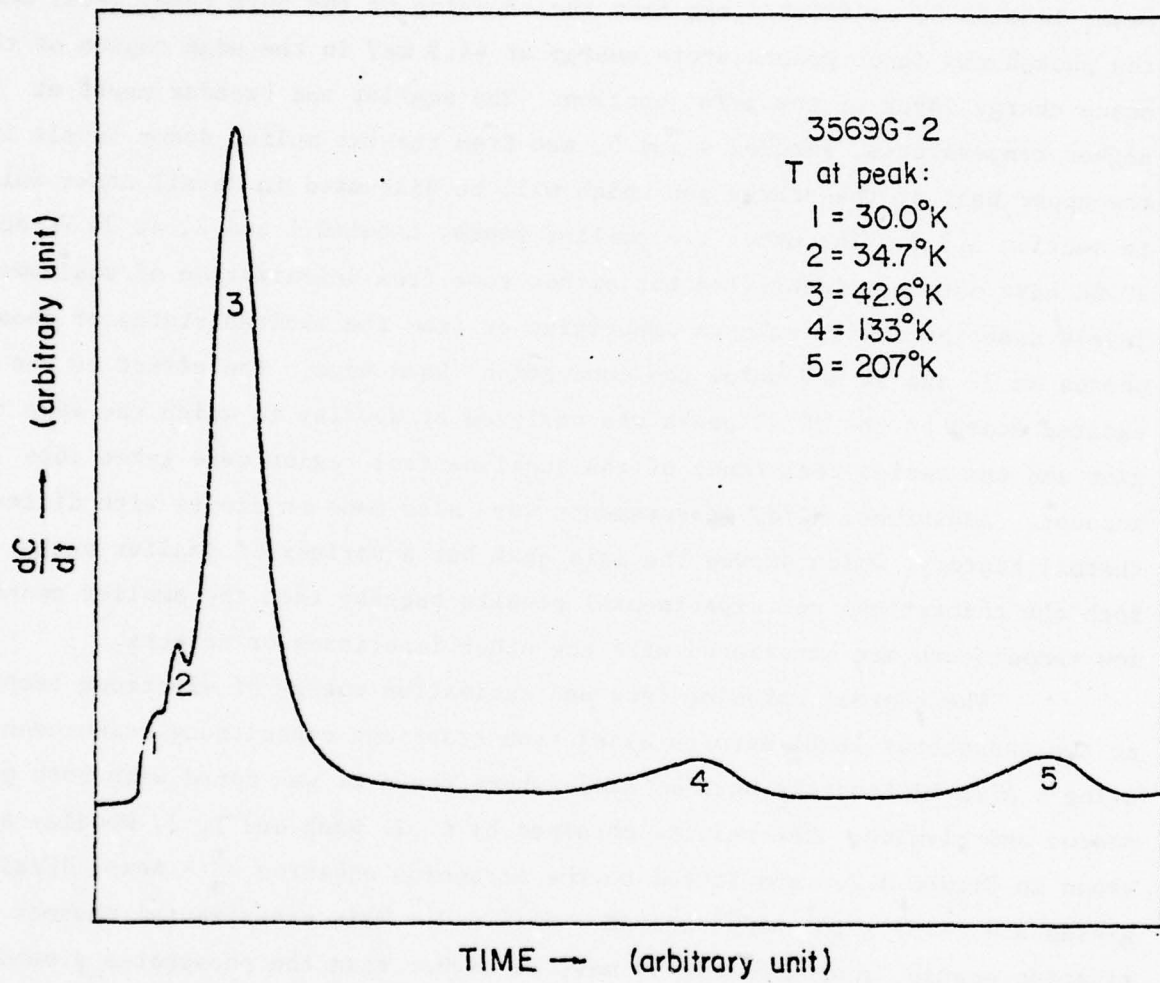


Figure 3.2.2 Thermally stimulated capacitance for sulfur doped p^+-n silicon diode. Peaks 1 and 2 are yet unidentified. Peak 3 is due to phosphorus donors in the edge region of the junction. Peaks 4 and 5 are due to neutral and singly ionized sulfur centers in the depletion region of the junction.

electric field when experimental errors are eliminated.

The phosphorus energy level was also measured by the TSCAP method applied to a p+/n junction on phosphorus doped silicon substrate. The derivative of TSCAP with respect to temperature is shown in Figure 3.2.2. The major peak, labeled 3, at 42.6K comes from the crossing of the bulk Fermi level and the phosphorus donor ground state energy at 44.5 meV in the edge region of the space charge layer of the p+/n junction. The smaller and broader peaks at higher temperatures, labeled 4 and 5, are from the two sulfur donor levels in the upper half of the energy gap which will be discussed in detail under Sulfur in section 3.3.7. The other two smaller peaks, labeled 1 and 2, at 34.7K and 30.0K have not been identified but either come from deionization of shallower levels associated with unknown impurities or from the excited states of phosphorus at 32 and 34 meV below the conduction band edge. The effect of the excited state on the dC/dT peaks was analyzed by Woodley in which the edge region and the series resistance of the quasi-neutral region were taken into account. Additional dC/dT measurements were also made on diodes with different thermal history, which showed the main peak but a variety of smaller peaks. Both the theoretical and experimental results suggest that the smaller peaks at low temperature are associated with the other impurities or defects.

The thermal emission rate and activation energy of electrons trapped at the phosphorus level were obtained from transient capacitance measurements using a Al/n-Si Schottky barrier diode where the n-Si was doped with both phosphorus and bismuth. The results obtained by C. T. Wang and T. J. Woodley are shown in Figure 3.2.3 and fitted to the Arrhenius equation $e_n^t = A \exp(-\Delta E/kT)$, giving $A = (4 \pm 5) \times 10^5 \text{ sec}^{-1}$ and $\Delta E = 53 \pm 5 \text{ meV}$. This experimental thermal activation energy, approximately 53 meV, is higher than the phosphorus ground state energy of 44.5 meV. The discrepancy is probably due to the deionization effect of the quasi-neutral region of the diode resulting in a high series resistance which distorts the capacitance transient considerably.

3.2.2 BISMUTH

The thermal activation energy of Bi in Si was first measured by the VSCAP method using a Al/n-Si Schottky barrier diode which was doubly doped with phosphorus and bismuth. The results are shown in Figure 3.2.3 giving a pre-exponential factor of $(2 \pm 2) \times 10^7 \text{ sec}^{-1}$ and a thermal activation energy of 67.1 meV compared with the published value of 70.9 meV. The thermal emission rate

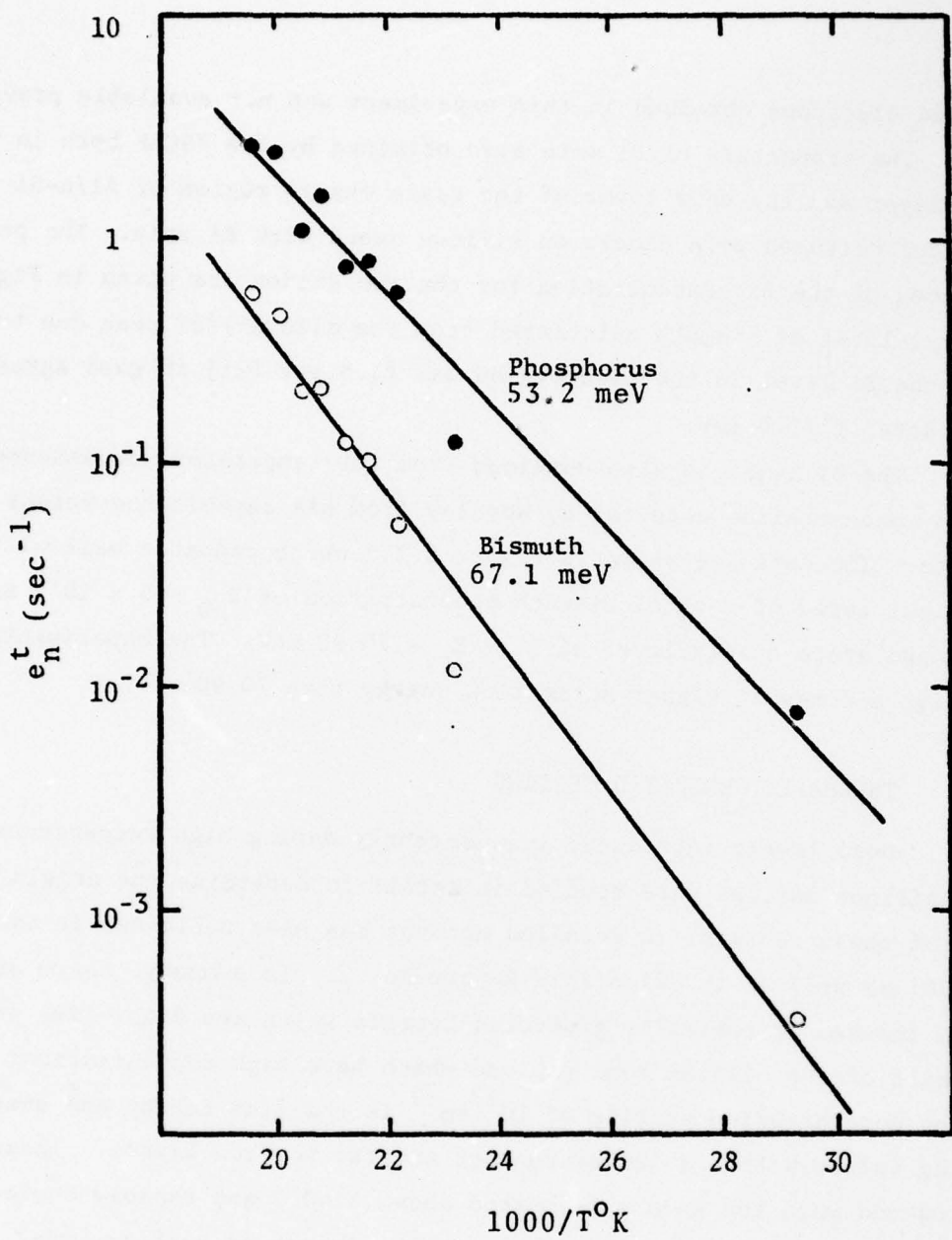


Figure 3.2.3 Reciprocal time constant or thermal emission rate of electrons trapped at the phosphorus and bismuth impurity atoms in the depletion region of the reverse biased Schottky Barrier diode.
Device No. 101D2 pin 1, $V_R = 20$ Volts.

of trapped electrons obtained in this experiment was not available previously.

The properties of Bi were also obtained by the VSCAP both in the depletion layer and the edge layer of the space charge region of Al/n-Si Schottky barrier and diffused p+/n diodes on silicon doped with Bi only. The position dependences of the Bi concentration for the two diodes are given in Figure 3.2.4. The energy level of bismuth calculated from the $d(TSCAP)/dT$ peak due to ionization of the Bi level in the edge region was 74.5 meV [21] in good agreement with optical data of 70.9 meV.

The Bi level is also obtained from the temperature dependence of the electron concentration computed by Woodley from his capacitance versus temperature data. The data are shown in Figure 3.2.5 which compares well with the theoretical curve of a total bismuth concentration of $N_{DD} = 3 \times 10^{14}$ Bi/cm³ and a Bi ground state energy level of $E_C - E_D = 70.90$ meV. The experimental data again give a somewhat higher activation energy than 70.90 meV.

3.2.3 THERMALLY GENERATED CENTERS

Deep levels introduced inadvertently during high temperature processing of silicon devices were studied in detail to determine the origin and the source of these centers. A detailed account has been published in the open literature [26] as well as in Scientific Report No. 2. In summary, there are four process induced or thermally generated centers which are donor-like and in the upper half of the silicon band gap and which have high concentrations with a U-shaped concentration profile of 10^{13} cm⁻³ in the flat region and sharply increasing values within a few microns of the two surface layers. These centers are produced when the sample is heated above 1100°C and rapidly cooled to room temperature provided that there is a highly disordered surface layer on the silicon slice. The disordered surface layer serves as the source of these recombination centers. It can be either a lapped surface or a surface with a high concentration diffused boron or phosphorus layer. Experimental evidence showed that these centers are vacancy or vacancy-impurity complexes and that they can be annealed out only after prolonged and slow cooling from 1100°C to 600°C. A few other centers were also observed during the thermal generation and quenching experiments [26] but they are at much lower concentrations and are generally gettered readily by the n+ phosphorus diffused layer. These levels are thought to be associated with residual impurities introduced during the high temperature processes.

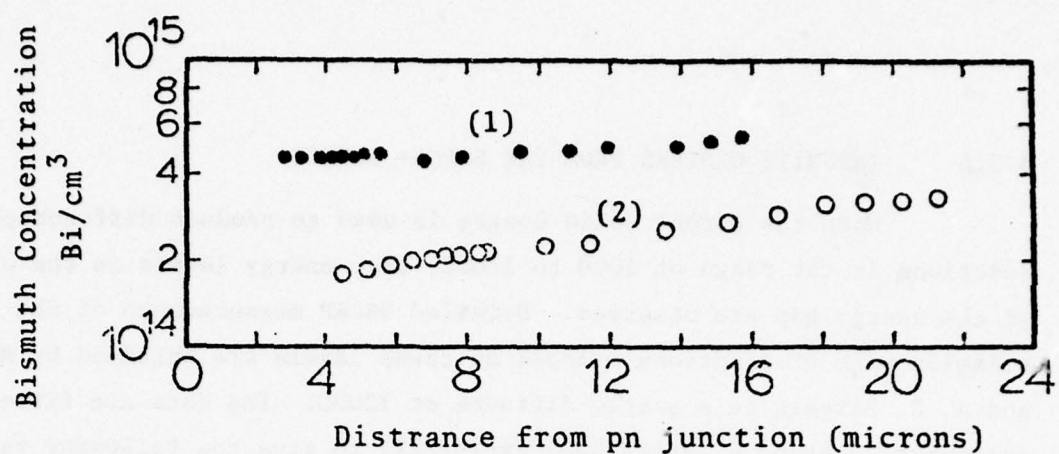


Figure 3.2.4 The concentration of Bi as a function of distance from the pn junction which is 0.5 micron from the surface for the diffused p+/n labeled (2) and for the Schottky Barrier diode labeled (1).

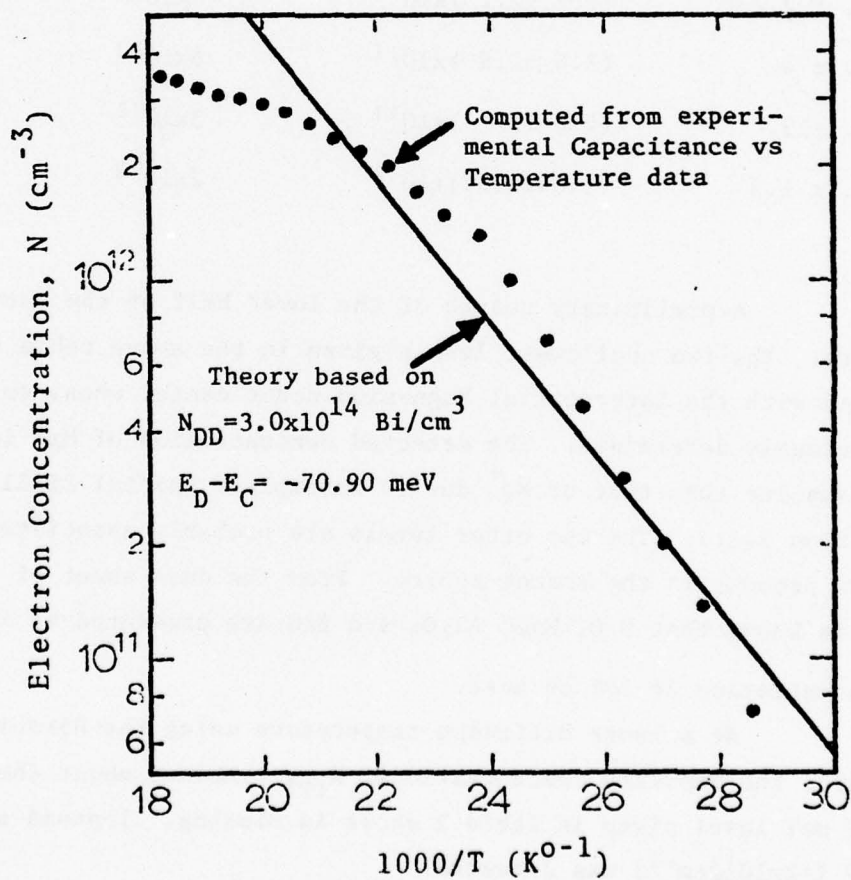


Figure 3.2.5 A comparison of the electron concentration calculated from experimental data of high frequency SB capacitance versus temperature with the theoretical electron concentration of silicon doped with $3.0 \times 10^{14} \text{ Bi/cm}^3$ with $E_D - E_C = 70.90 \text{ meV}$.

3.2.4 IMPURITY CENTERS FROM THE BORON+ SOURCE

When the Boron+ solid source is used to produce diffused p+/n silicon junctions in the range of 1000 to 1200C, four energy levels in the upper half of the energy gap are observed. Detailed VSCAP measurements of the thermal emission rate of electrons trapped at these levels are obtained by R. L. Marchand and A. R. Stivers in a sample diffused at 1200C. The data are fitted to the Arrhenius equation $e_n^t = A(T/300)^2 \exp(-E/kT)$ to give the following results:

Table 2

Parameters of Impurity Centers from the Boron+ Source

E(meV)	A(sec ⁻¹)	N _{TT} (cm ⁻³)	Origin (Tentative)
93. ± 2.2	(7.7 ± 2.1) × 10 ⁴	>6 × 10 ¹¹	Mg ⁰
256. ± 4.	(7.6 ± 2.8) × 10 ¹¹	6 × 10 ¹²	Mg ⁺
279. ± 13.	(5.0 ± 6.) × 10 ¹¹	3 × 10 ¹²	?
534.7 ± 1.3	(1.04 ± 0.07) × 10 ¹²	2 × 10 ¹³	?

A preliminary search of the lower half of the band gap gave null results. The two shallowest levels given in the above table appear to be associated with the interstitial Magnesium donor center whose energy levels were previously determined. The detected concentration of Mg⁰ level, N_{TT} > 6 × 10¹¹, is smaller than that of Mg⁺ due to incomplete initial filling discussed in section 3.1.3. The two other levels are probably associated with the impurities present in the Boron+ source. From the data sheet of the Boron+ source, it is known that SrO, MgO, Al₂O₃ and BaO are presented as impurities at a concentration of 10% or more.

At a lower diffusion temperature using the Boron+ source, such as 1100C, the impurity concentrations, N_{TT}, remained about the same. However, the 279 meV level given in Table 2 above is missing. Instead a new level at 335 ± 3 meV (=2 × 10¹³ cm⁻³) was detected.

Detailed studies are continuing on the origin and generation-annealing-diffusion kinetics of these centers as well as the feasibility of using such a multi-impurity diffusion source to introduce deep and shallow level impurity centers with potentially useful properties in detector applications.

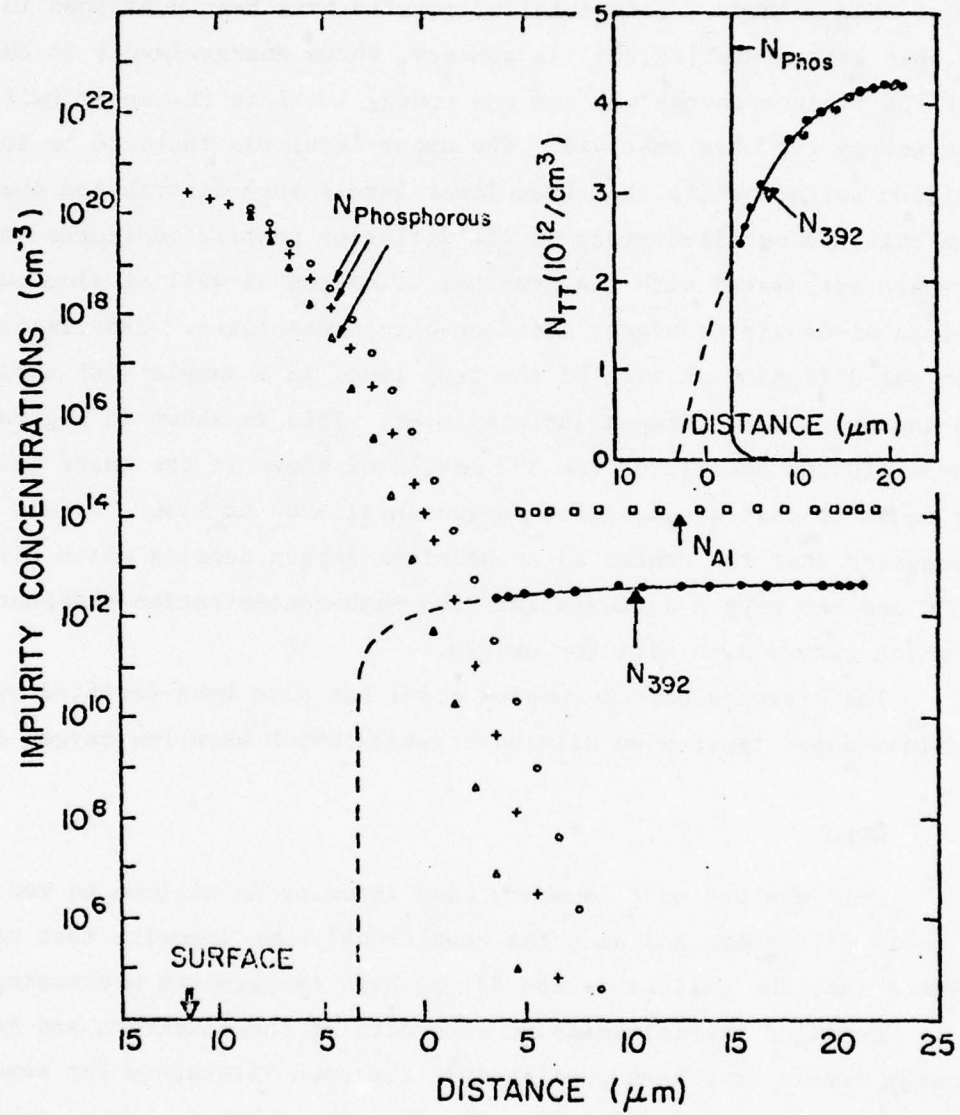


Figure 3.2.6 The concentration profile of the aluminum N_{Al} , and $E_V + 392$ meV hole trap, N_{392} . The phosphorus concentration profiles are computed from $\exp(-x^2/4Dt)$ using three slightly different values for the phosphorus diffusivity D .

3.2.5 ALUMINUM-OXYGEN COMPLEXES

Using VSCAP, a detailed study was made on the centers thermally generated in aluminum-doped silicon crystals, grown both by the Czochralski and the float zone methods. Some detailed results have been published in two papers in the open literature.[27,28] In summary, three energy levels in the lower half of the silicon energy gap and one energy level in the upper half of the silicon energy gap were observed. The upper level was found to be located near the silicon surface while the three lower levels were distributed deep into the silicon bulk. A detailed study of the diffusion profile indicates that these centers are associated with the presence of oxygen as well as aluminum in the form of an Al-O pair or higher aluminum-oxygen complexes. Experiments at 1150C gave an out-diffusion profile of the deep level in a sample with a high phosphorus-concentration diffused surface layer. This is shown in Figure 3.2.6. The out-diffusion profile of the 392 meV level shown in the inset gave a diffusivity equal to that observed for oxygen in silicon at 1150C, $4.4 \times 10^{-11} \text{ cm}^2/\text{sec}$. This suggests that the center is an aluminum-oxygen complex which dissociates at 1150C and the oxygen diffuses into the high-concentration phosphorus diffused layer which serves as a sink for oxygen.

The oxygen-aluminum complex model has also been verified by experiments on aluminum-doped float-zone silicon crystals which have low oxygen concentration.

3.2.6 GOLD

Gold was the most commonly used impurity in silicon to reduce the minority carrier lifetime and also the most troublesome impurity that can be easily introduced into the silicon device during high temperature processing.

Detailed thermal emission rate data of the electrons and holes at the two energy levels have been published in the open literature for some time and are reproduced in Figure 3.2.7.[18,19] However, the thermal capture rates had not been obtained until a preliminary set of data were published recently.[18,19] This is given in Figure 3.2.8. Preliminary capture rate data has also been obtained by the edge effect method discussed in section 3.1.3. This is given in Figure 3.2.9. One of the main problems in the capture rate measurement is that the observed capture process occurs in a high electric field region where the hot electron (or hole) effect is appreciable while the capture process that controls the usual electron-hole recombination lifetime occurs in a low field

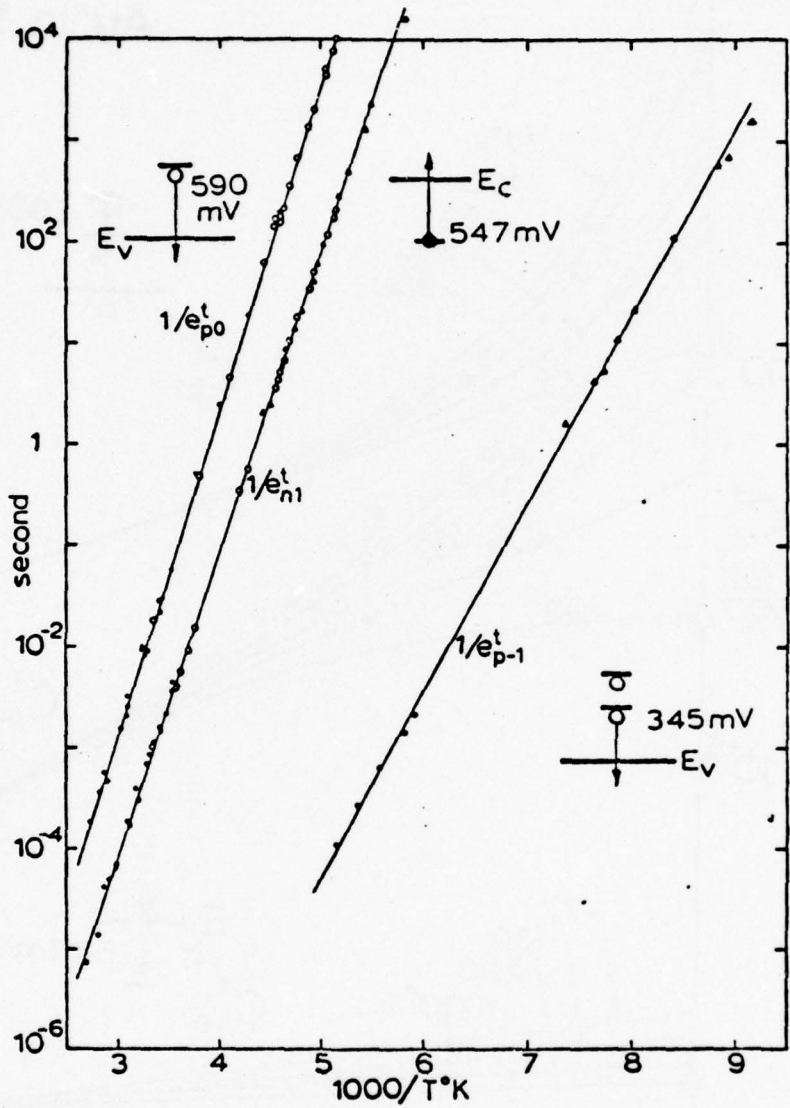


Figure 3.2.7 The thermal emission rates of electrons, e_{n1}^t , and holes, e_{p0}^t , trapped at the gold acceptor center, $E_C - 547 \text{ mV}$ or $E_V + 590 \text{ mV}$, and the thermal emission rates of holes, e_{p-1}^t , trapped at the gold donor center, $E_V + 345 \text{ mV}$, obtained from the dark transient capacitance measurements as well as the dark current transient measurements, the latter for time constants less than 1 second.

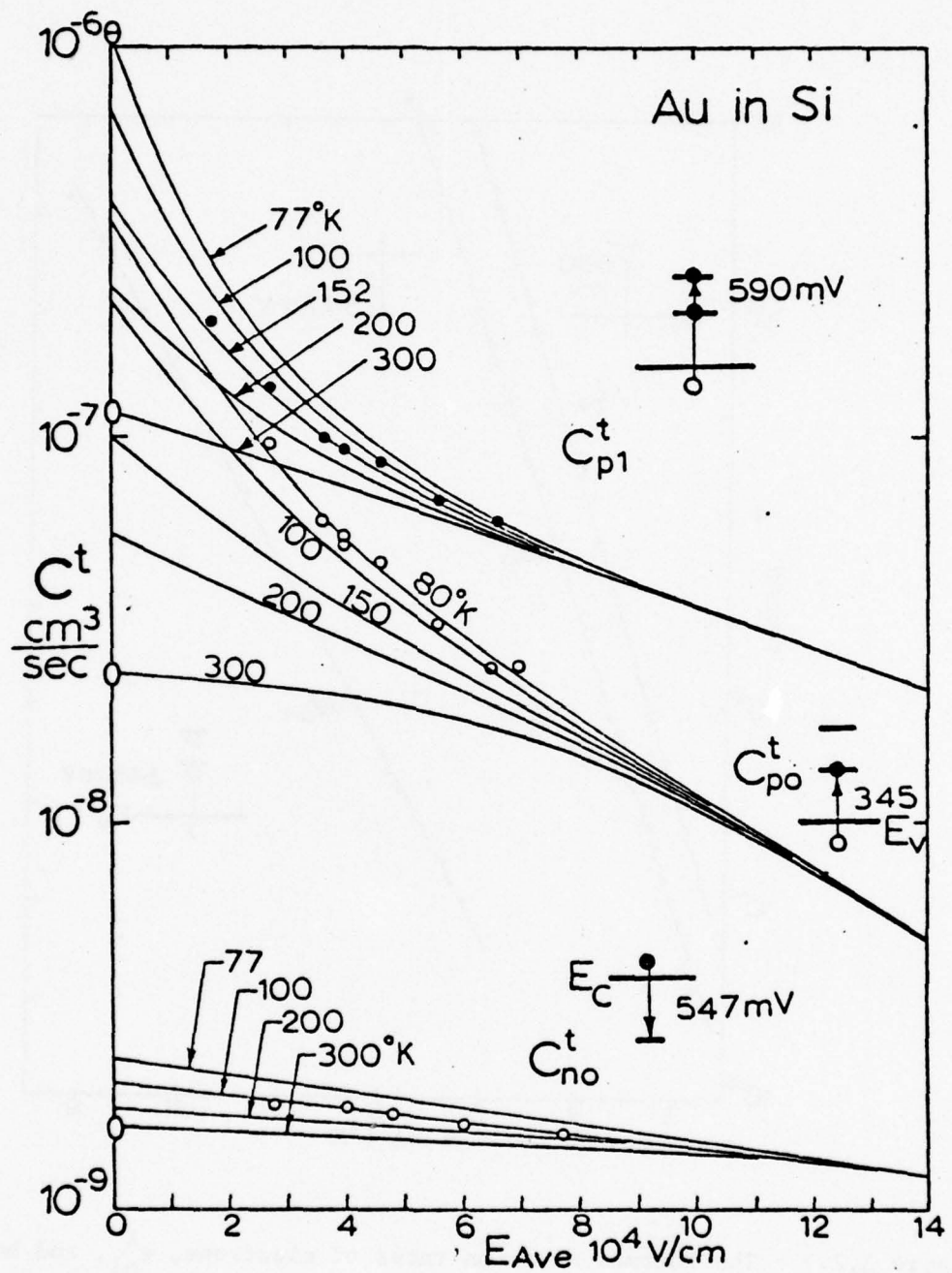


Figure 3.2.8 The electric field and temperature dependences of the thermal capture coefficients of electrons and holes at the gold acceptor and donor centers in silicon from the photo capacitance experiments.

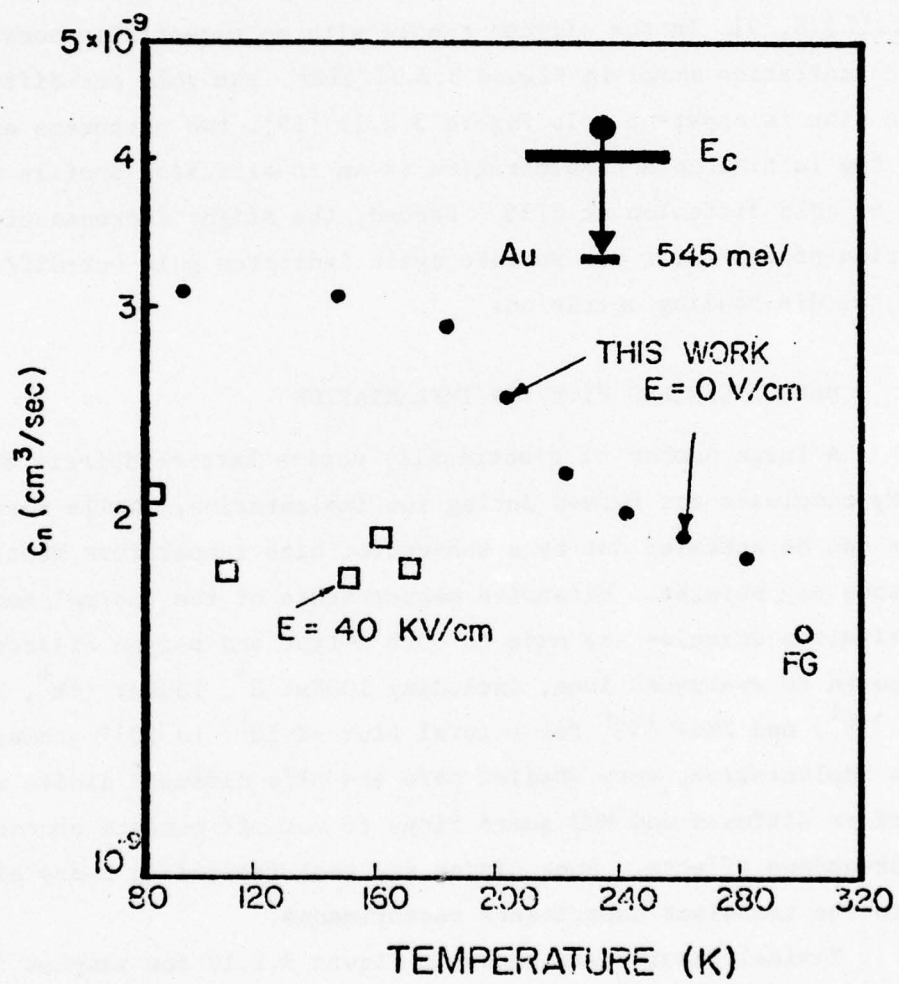


Figure 3.2.9 c_{n0}^t for a gold doped p+n diode, at a field between 0 and 6.7 KV/cm.
 $N_{DD} = 5 \times 10^{14}/\text{cm}^3$; $N_{TT} = 3 \times 10^{12}/\text{cm}^3$.

or quasi-neutral region which is essentially at thermal equilibrium. The edge effect method for measurement of the capture rate discussed in section 3.1.3 gives essentially the thermal equilibrium capture rate.

The concentration profiles of gold have been measured within a few micron of the silicon surface of the Al-Si interface of a Schottky barrier. A substantial amount of gold out-diffusion into the aluminum sink has been discovered at temperatures as low as 450 C during a 180 sec die-bond heating of the silicon chip on a TO-18 header. Illustrative examples are shown in Figures 3.2.10 and 3.2.11 [18,19]. In the silicon sample with an essentially constant initial gold concentration shown in Figure 3.2.10 [18], the gold out-diffusion into a surface sink is apparent. In Figure 3.2.11 [19], two phenomena are evident. First, the initial gold concentration is an in-diffusion profile which is obtained by gold diffusion at 875C. Second, the slight decrease of the gold concentration profile near the surface again indicates gold out-diffusion at 450C during the die-bonding operation.

3.2.7 DEFECT CENTERS FROM ION IMPLANTATION

A large number of electrically active lattice defects and vacancy-impurity complexes are formed during ion implantation. While most of these centers can be annealed out by a subsequent high temperature heating above about 900C, some may persist. Extensive measurements of the thermal emission rates and activation energies are made on both n-type and p-type silicon after they are exposed to energetic ions, including 100KeV H⁺, 150KeV ¹¹B⁺, 300KeV ²⁸Si⁺, 1.3MeV ³⁴S⁺, and 2MeV ¹⁰O⁺ for a total flux of 10^{11} to 10^{16} atoms/cm². Prior to the ion implantation, very shallow p+/n and n+/p diffused diodes were made with appropriate diffused and MOS guard rings to cut off surface channels and perimeter breakdown effects. Some diodes are heat treated in a dry nitrogen ambient prior to the transient capacitance measurements.

Typical results are shown in Figure 3.2.12 for samples implanted with 10^{12} O/cm². The labels are as follows. The labels 0, 01, and 04, at the top of the curve, indicate a subsequent anneal of 90 seconds at 150°C for 01, 400°C for 04 and no annealing for label 0. The numerical labels on the side of these curves are the peak temperatures of the d(TSCAP)/dT curve and the thermal activation energies relative to the indicated band edge using m=0 in the Arrhenius equation given by $e = A \exp(-E/kT)$. The concentration of these centers is also

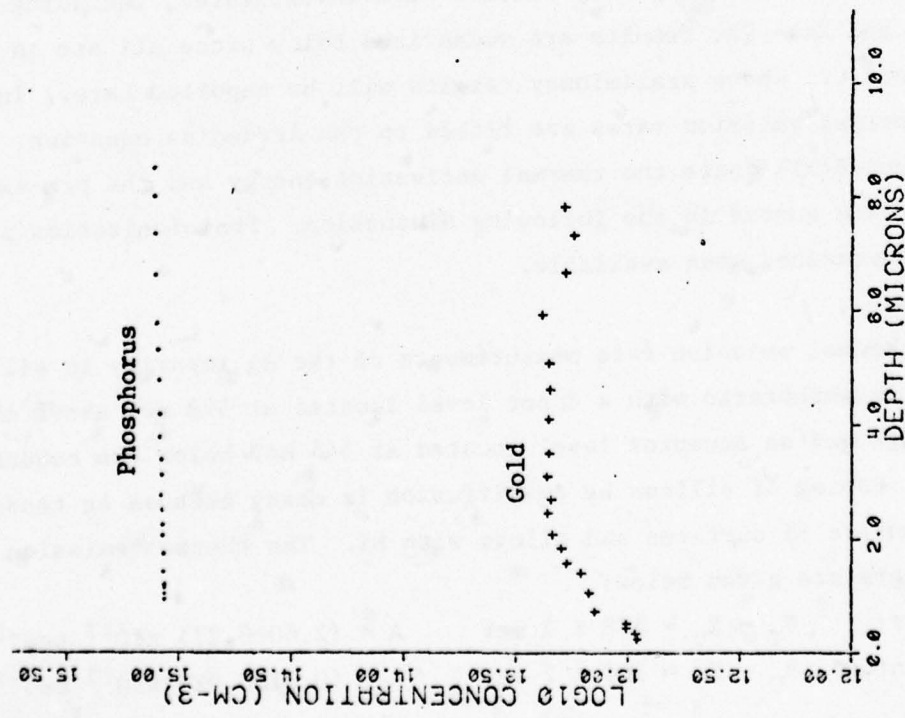


Figure 3.2.10 The outdiffusion profile of gold in the silicon surface layer into an aluminum sink in an Al on n-Si Schottky barrier diode.

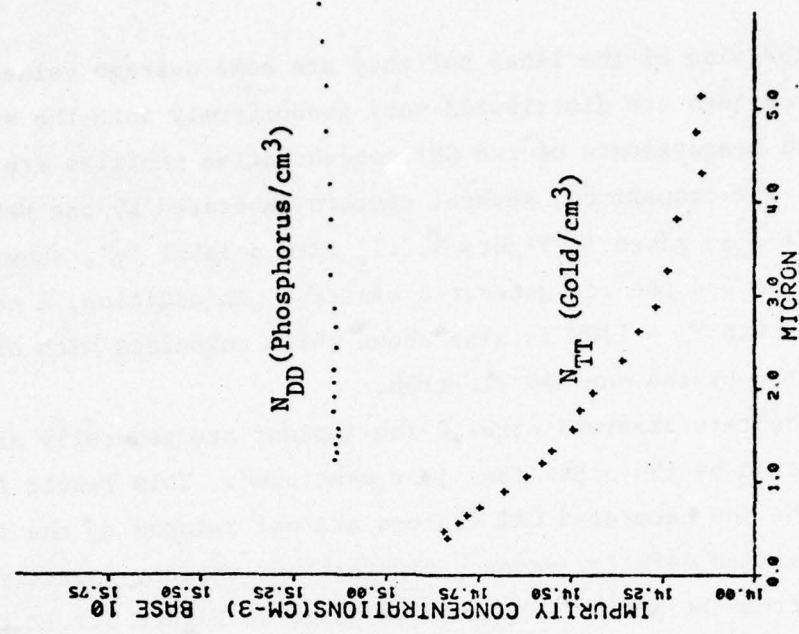


Figure 3.2.11 The concentration profile of gold near the silicon surface from dark transient capacitance measurements on a Al on n-Si Schottky barrier diode. Gold is diffused into the n-type silicon at 875°C. (From the doctoral dissertation of Tom Y. Lo.)

indicated on the side of the lines but they are some average values since ion generated GRT centers are distributed very nonuniformly into the silicon surface. Detailed measurements of the GRT concentration profiles are incomplete at this time. For comparison, several centers generated by one MeV electron irradiation are also given in Figure 3.2.12 with a label 'e', showing similarities between them and the ion generated centers. In addition, a center generated by Si ion with $T_M = 170K$ is also shown which coincides with one of the centers generated by the one MeV electron.

The centers observed after 0 ion implant are generally also observed after implantation by the other ions just mentioned. This result indicates that most of the ion generated GRT centers are not related to the ion species used but are lattice defects, vacancy clusters and vacancy-impurity complexes. It is evident from the preliminary results given in Figure 3.2.12 that there is much interesting and very application-relevant work, such as integrated IR detector arrays, that needs to be done by detailed measurements of the thermal activation energy and emission rates as well as the concentration profiles of the centers generated by energetic ions during ion implantation processes.

3.2.8 OTHER IMPURITY CENTERS

A number of other impurity centers were investigated, including Ag, Co, Cr, S, Ta, and Zn. The results are summarized below since all are in open literature except Cr, whose preliminary results will be reported here. In this summary, the thermal emission rates are fitted to the Arrhenius equation, $e = A(T/300)^2 \exp(-E/kT)$ where the thermal activation energy and the pre-exponential factor, A, are quoted in the following discussion. Photoionization properties are also summarized when available.

Silver

The thermal emission rate measurements of the Ag impurity in silicon showed that it is amphoteric with a donor level located at 378 meV above the valence band edge and an acceptor level located at 544 meV below the conduction band edge.[29] Doping of silicon by Ag diffusion is messy because Ag tends to flow over the entire Si surfaces and alloys with Si. The thermal emission rates of the two centers are given below:

$$\begin{array}{lll} \text{Donor Center: } E_T - E_V = 378 \pm 2 \text{ meV} & A = (2.60 \pm 0.27) \times 10^{13} \text{ sec}^{-1} \\ \text{Acceptor Center: } E_C - E_T = 544 \pm 2 \text{ meV} & A = (0.31 \pm 0.026) \times 10^{13} \text{ sec}^{-1} \end{array}$$

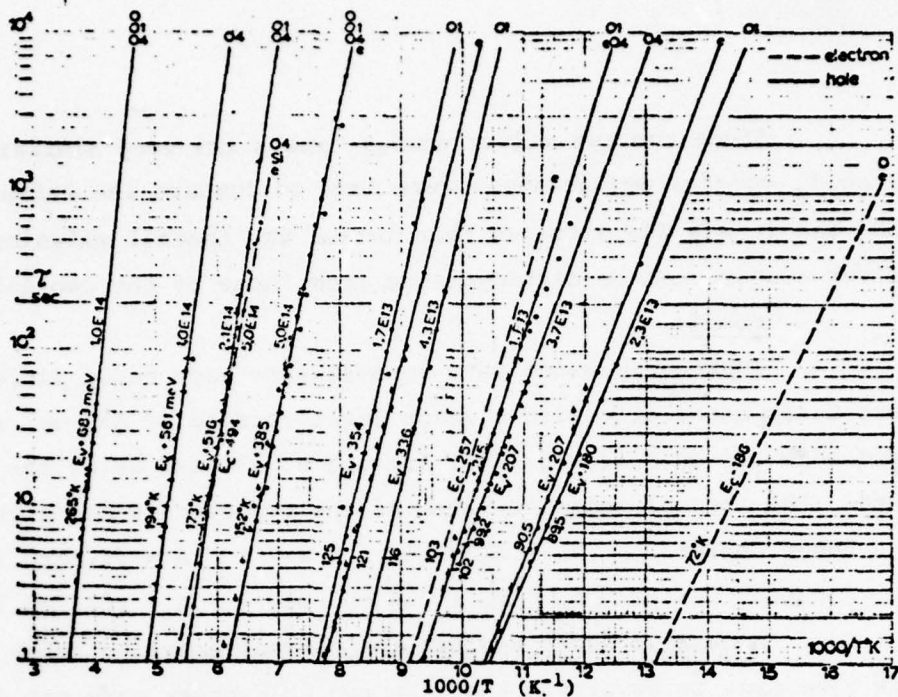


Figure 3.2.12 The reciprocal emission rate or the transient capacitance decay time constants of the energy levels generated during ion implantation as a function of reciprocal temperature. The data are fitted to the Arrhenius equation $e = A \exp(-E/kT)$.

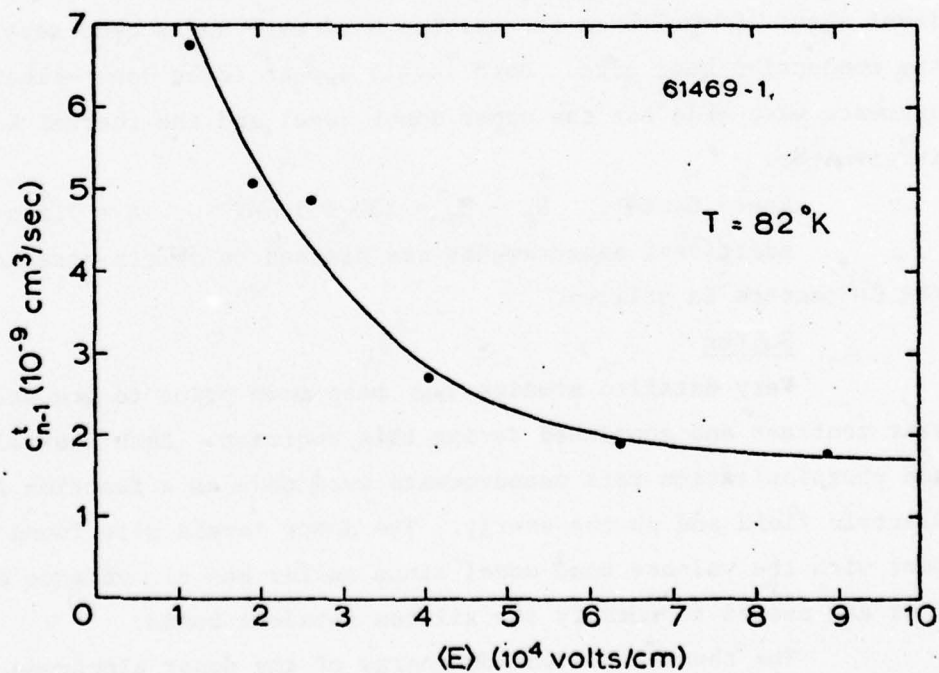


Figure 3.2.13 Field dependence of the capture rate of electrons by singly ionized sulfur centers.

Since the two silver energy levels are very similar to those of gold, careful measurements were made to compare the emission rate results [30] and it was demonstrated that indeed the thermal emission rates at the two silver centers can be distinguished from those of the two gold centers.

Cobalt

Thermal emission rate measurements made on Co diffused silicon showed that Co is amphoteric with a donor level located at 352 meV above the valence band edge and an acceptor level located at 534 meV below the conduction band edge. The thermal emission rates of the two centers are given below:[30,31]

$$\text{Donor Center: } E_T - E_V = 352 \pm 1 \text{ meV} \quad A = (2.46 \pm 0.19) \times 10^{13} \text{ sec}^{-1}$$

$$\text{Acceptor Center: } E_C - E_T + 534 \pm 3 \text{ meV} \quad A = (0.77 \pm 0.10) \times 10^{13} \text{ sec}^{-1}$$

A careful check against the thermal emission rates of the gold centers was also made to ascertain that the two Co centers were not due to gold contaminations.[30]

Chromium

Chromium was introduced into silicon during Czochralski crystal growth with a segregation coefficient of about 10^{-6} at the silicon melting point. From thermal emission rate measurements, it was found that Cr appears to introduce two energy levels into silicon. Preliminary data indicates that there is a shallow level about 180 meV from the valence band edge and a deep level at 232 meV from the conduction band edge. Both levels appear to be donor-like. Accurate measurements were made for the upper donor level and the thermal emission rate data is given by:

$$\text{Donor Center: } E_C - E_T = 232 \pm 3 \text{ meV} \quad A = 7.6 \times 10^{13} \text{ sec}^{-1}$$

Additional measurements are planned to obtain more accurate data on the Cr centers in silicon.

Sulfur

Very detailed studies had been made prior to the start of this five-year contract and continued during this contract. Both thermal emission rate and photoionization rate measurements were made as a function of temperature, electric field and photon energy. Two donor levels were found which are consistent with the valence bond model since sulfur has six valence electrons and only four are needed to satisfy the silicon covalent bonds.

The thermal activation energy of the donor electrons at the two S centers are given below.[32]

$$\text{First Donor: } E_C - E_T = 276 \pm 1 \text{ meV} \quad A = (1.64 \pm 0.12) \times 10^{10} \text{ sec}^{-1}$$

$$\text{Second Donor: } E_C - E_T = 528 \pm 4 \text{ meV} \quad A = (1.03 \pm 0.22) \times 10^{12} \text{ sec}^{-1}$$

Electric field dependences of the thermal capture rates of electrons at both of the sulfur donor centers were measured and these are given in Figures 3.2.13 and 3.2.14. In addition, impact ionization rates of the neutral sulfur center by electrons was also measured and shown in Figure 3.2.15.

The fine details of the photoionization rates were first obtained for the second donor by Rosier [33,34], indicating a strong photothermal ionization process below the ground state threshold of 613 meV, a value obtained from absorption measurements. The photothermal ionization process is a two step process in which the electron is first optically excited from the 613 meV ground state to an excited state and then thermally released from the excited state into the conduction band. Fine structures were observed as follows: [see Figure 3.3.12 in section 3.4.3 for the experimental data]

524 meV	$1s(A_1) \rightarrow 1s(T_2)$
570 meV	$1s(A_1) \rightarrow 2p_0$
574 meV	$1s(A_1) \rightarrow 2s(T_2)$
591 meV	$1s(A_1) \rightarrow 2p_{\pm}$

where the ground state, $1s(A_1)$, is located at 613 meV below the conduction band edge.

Detailed photoionization rate measurements were also carried out for the first donor center which contains two electrons.[35] The low temperature threshold obtained by extrapolating the data of 59.8K. appears to reach 280 meV, which is nearly that of the thermal activation energy from thermal emission rate measurements at high temperatures, 276 meV. An absorption peak was observed at 285.4 meV which is attributed to the $[1s(A_1), 1s(A_1)] \rightarrow [1s(A_1), 1s(T_2)]$ optical transition while the continuum is 315 meV above the ground state $[1s(A_1), 1s(A_1)]$. The broadening of the absorption line at 285.4 meV was shown to be due to lattice or phonon scattering and follow a Lorentzian line shape (See section 3.3.3).

Tantalum

Thermal emission measurements on Ta-doped silicon crystals indicated that there are two donor levels below the silicon conduction band edge with the following parameters:

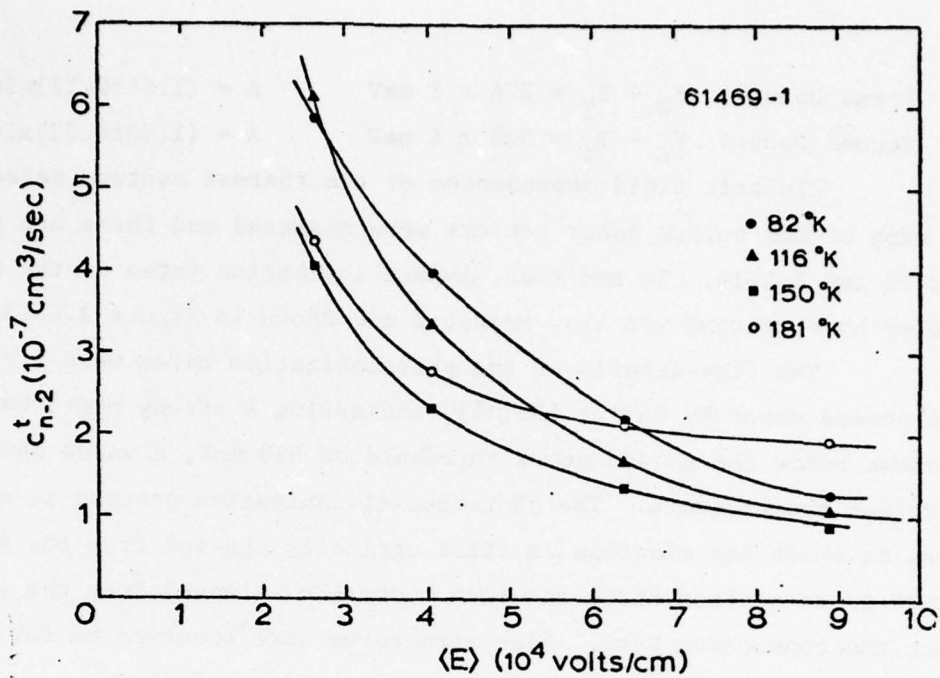


Figure 3.2.14 Field dependence of the capture rate of electrons by doubly ionized sulfur centers.

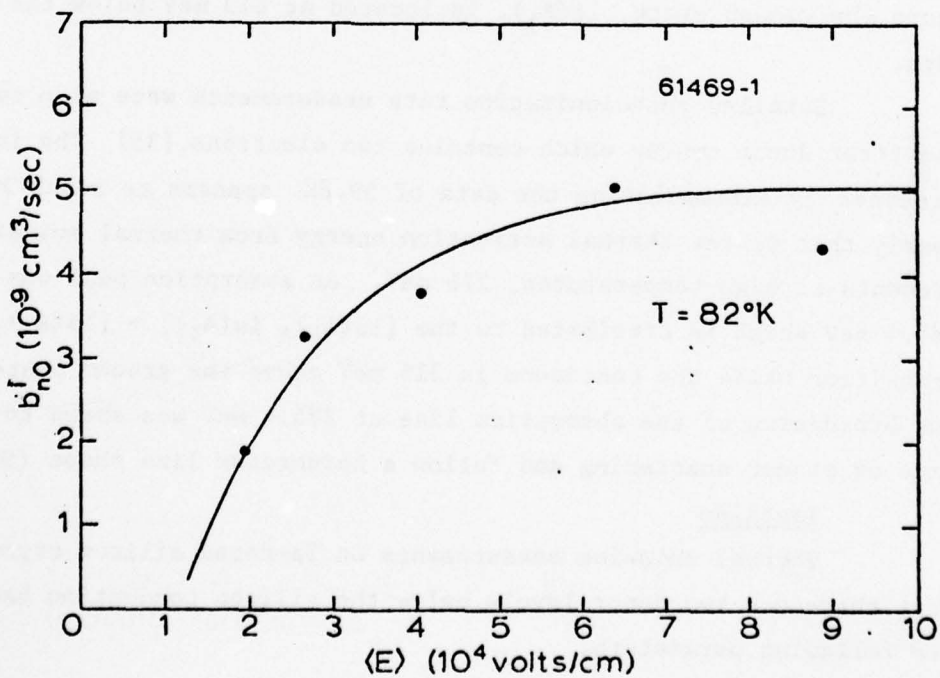


Figure 3.2.15 Field dependence of the impact ionization rate of neutral sulfur centers.

First Donor: $E_C - E_T = 232 \pm 5$ meV $A = (1.50 \pm 0.83) \times 10^{10} \text{ sec}^{-1}$

Second Donor: $E_C - E_T = 472 \pm 8$ meV $A = (1.47 \pm 0.78) \times 10^{10} \text{ sec}^{-1}$

There were serious difficulties in getting sufficient concentration of Ta into Si during crystal growth due to the very low segregation coefficient, estimated at 10^{-8} or less.

Zinc

Detailed measurements of the thermal emission rates, thermal capture rates and photoionization cross sections were made on Zn-diffused silicon n+/p and p+/n junctions [36,37,38] because of the considerable interest shown by previous workers in Zinc as a possible IR detection center in silicon.

Thermal emission rate measurements indicated that zinc gives two acceptor levels in the silicon band gap, located at 297 and 571 meV above the valence band edge. These are consistent with the valence bond model since zinc has only two valence electrons and needs two additional electrons to complete the tetrahedral covalent bond of the silicon lattice. A shallow level at 150 meV from the valence band edge is also observed in zinc diffused and boron-doped silicon crystal which was shown to be a BZn_3 complex. The thermal emission parameters are listed below.

First Acceptor: $E_T - E_V = 297 \pm 1$ meV $A = (6.78 \pm 0.68) \times 10^{12} \text{ sec}^{-1}$

Second Acceptor: $E_T - E_V = 571 \pm 1$ meV $A = (0.14 \pm 0.002) \times 10^{12} \text{ sec}^{-1}$

BZn_3 Acceptor: $E_T - E_V = 167 \pm 10$ meV $A = (1.5 \pm 2.) \times 10^{10} \text{ sec}^{-1}$

The thermal capture rates measured in high electric field and the electron impact ionization rate are also measured and these are given in Figures 3.2.16, 3.2.17, and 3.2.18.

The photoionization cross sections show some temperature and field dependences below the continuum threshold but no distinct structures or peaks such as those observed for the two sulfur donor levels.

3.3 THEORETICAL ANALYSES AND INTERPRETATIONS

Theoretical analyses of the photoionization cross sections of impurity centers were carried out for the following cases: the Coulomb and the square three-dimensional impurity potential wells with one bound electron (or hole) and the Coulomb potential well with two bound electrons. The results are summarized in the following subsections and compared with some available experimental data.

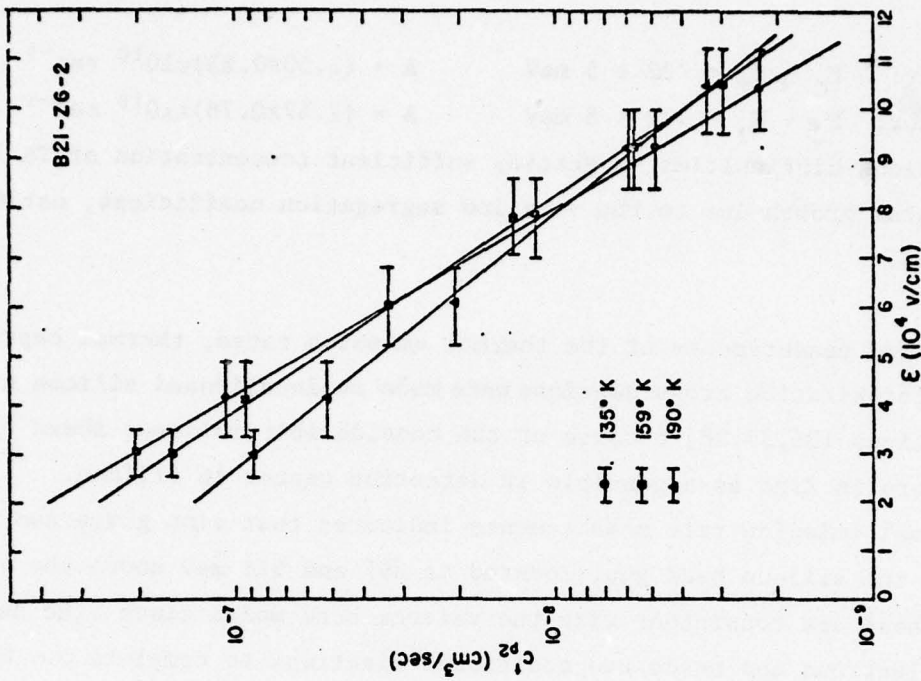


Figure 3.2.17 Electric field dependence of the thermal capture rate of holes at doubly ionized zinc centers at the temperatures indicated

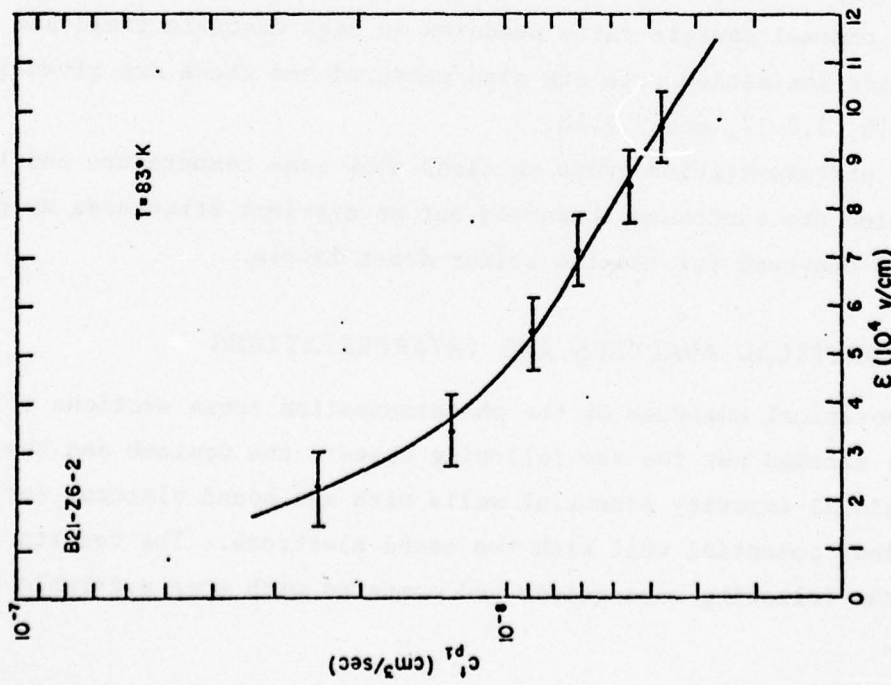


Figure 3.2.16 Electric field dependence of the thermal capture rate of holes at singly ionized zinc centers.

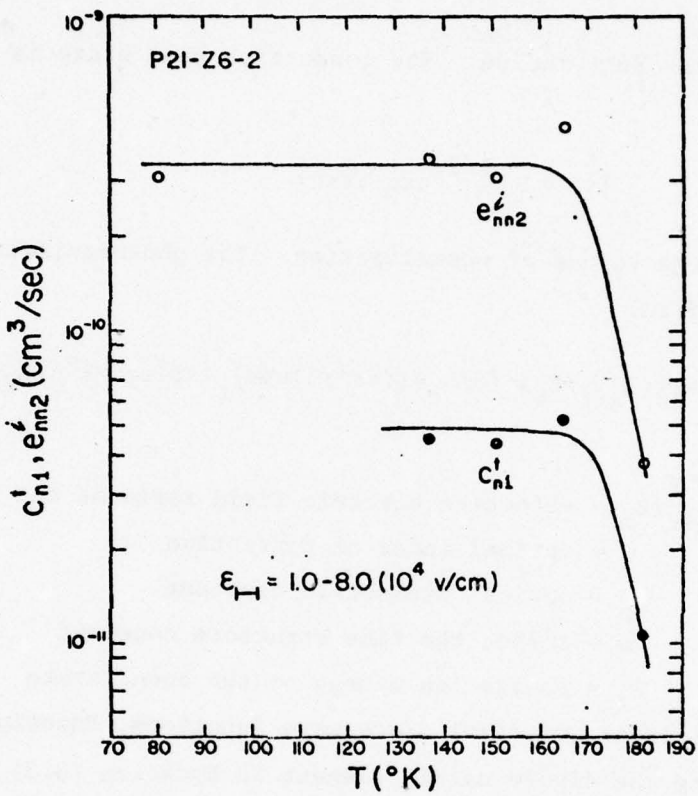


Figure 3.2.18 Temperature dependence of the thermal capture rate of electrons at singly ionized zinc centers and Auger-impact emission rate of electrons at doubly ionized zinc centers.

3.3.1 COULOMB WELL FOR SHALLOW LEVEL CENTERS

The bound-state wavefunction is given by

$$|i\rangle = (\pi a^3)^{-1/2} \exp(-r/a) \quad (3.1)$$

where a is the Bohr radius. The conduction band state is given by the plane wave

$$|f\rangle = V^{-1/2} \exp(i\vec{k}\cdot\vec{r}) \quad (3.2)$$

where V is the volume of normalization. The photoionization cross-section is calculated from

$$\sigma(h\omega) = [(E_{\text{eff}}/E_0)^2(n/\epsilon_0)](4\pi^2/3)a\hbar\omega \sum_f |\langle f | \vec{r} | i \rangle|^2 \delta(E_f + E_I - \hbar\omega) \quad (3.3)$$

where

E_{eff}/E_0 = effective electric field ratio at the impurity ion center

n = optical index of refraction

ϵ_0 = optical dielectric constant

$\alpha = e^2/hc$, the fine structure constant

E_I = ionization energy of the bound state

Using the initial and final state wave functions, Equations (3.1) and (3.2), to calculate the dipole matrix element in Equation (3.3), the photoionization cross-section is given by

$$\sigma(h\omega) = [(E_{\text{eff}}/E_0)^2(n/\epsilon_0)](4\pi\alpha/3)a^2 S(h\omega) \quad (3.4)$$

Here the dimensionless shape function is given by

$$S(X) = 256AX[A(X-E_I)]^{3/2}[1+A(X-E_I)]^{-6} \quad (3.5)$$

where $X = \hbar\omega$, $A = 2m^*a^2/\hbar^2$ and the spherical band $E = \hbar^2k^2/2m^* = \hbar\omega - E_I$ is used. This was obtained previously.[39]

Equations (3.4) and (3.5) are fitted to the published photoionization spectra of group III acceptors in silicon using the Bohr radius ' a ' as the adjustable parameter. These are shown in Figures 3.3.1 to 3.3.4.

The effective radii ' a ' thus determined are plotted in Figure 3.3.5 as a function of E_I . In Figure 3.3.5, the ' a ' from variational calculations of the group V donors in silicon are also plotted. All the ' a ' values thus

Figure 3.3.1

Spectral dependence of the photoionization cross-section of B in Si. The theory is based on a Coulomb potential well.

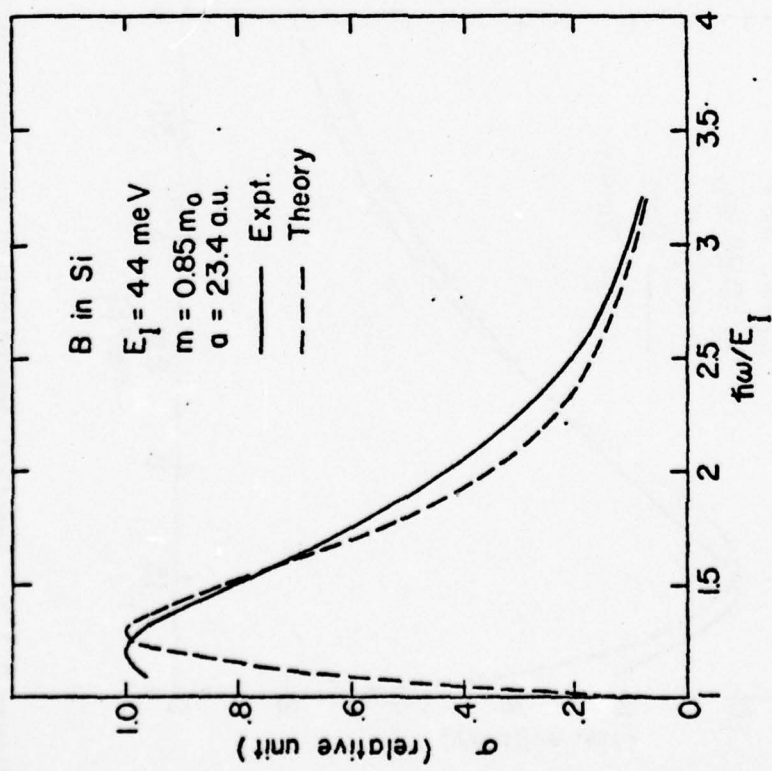


Figure 3.3.2

Spectral dependence of the photoionization cross-section of Aluminum in Silicon (Al in Si). The theory is based on a Coulomb potential well.

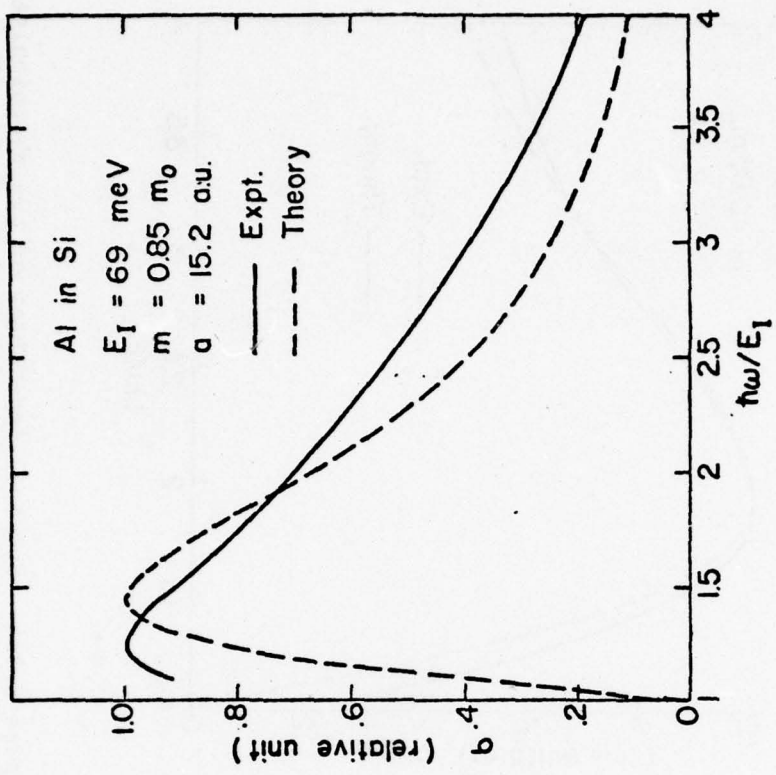


Figure 3.3.3 Spectral dependence of the photoionization cross-section of Ga in Si. The theory is based on a Coulomb potential well.

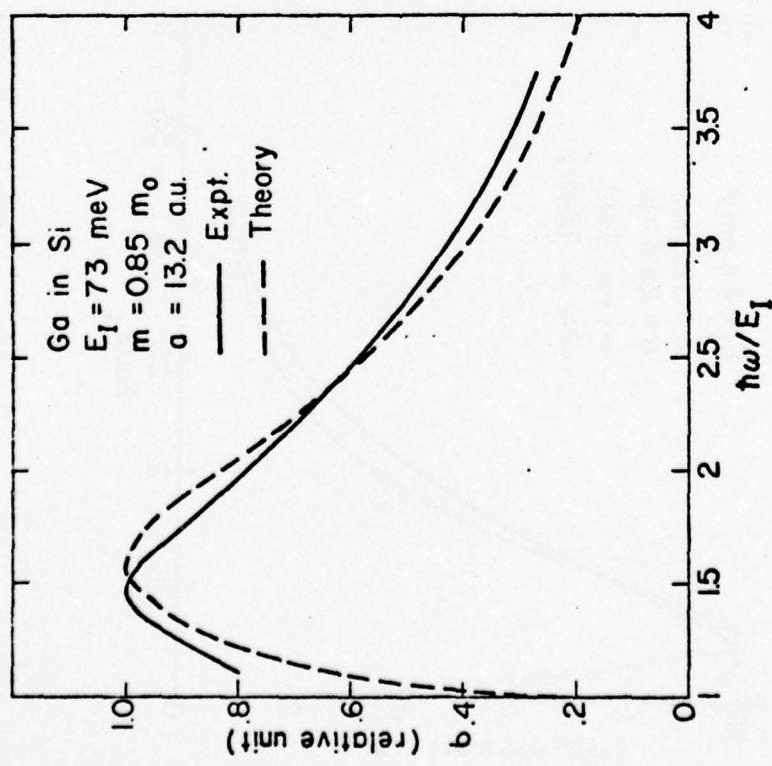
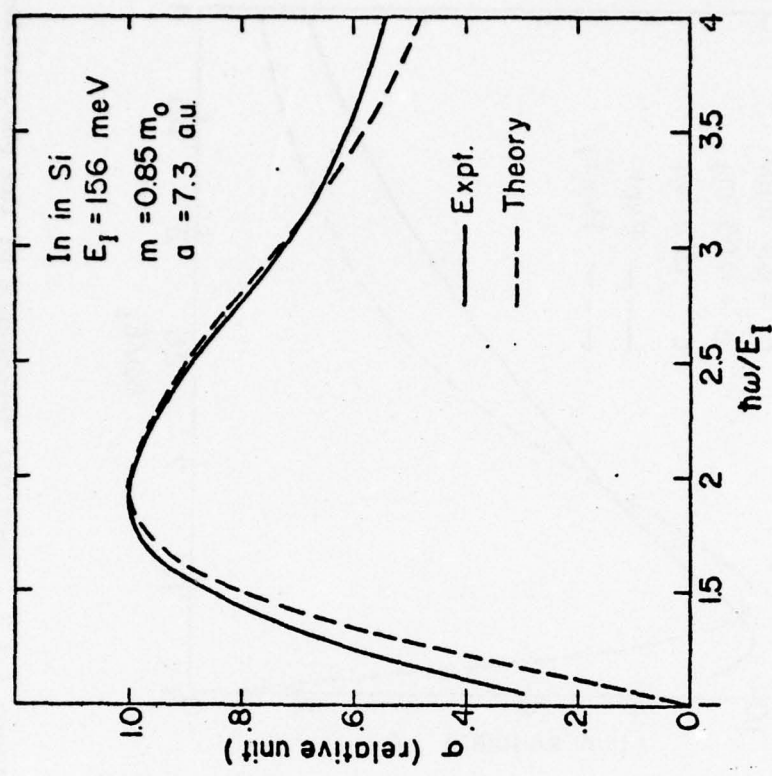


Figure 3.3.4

Spectral dependence of the photoionization cross-section of In in Si. The theory is based on a Coulomb potential well.



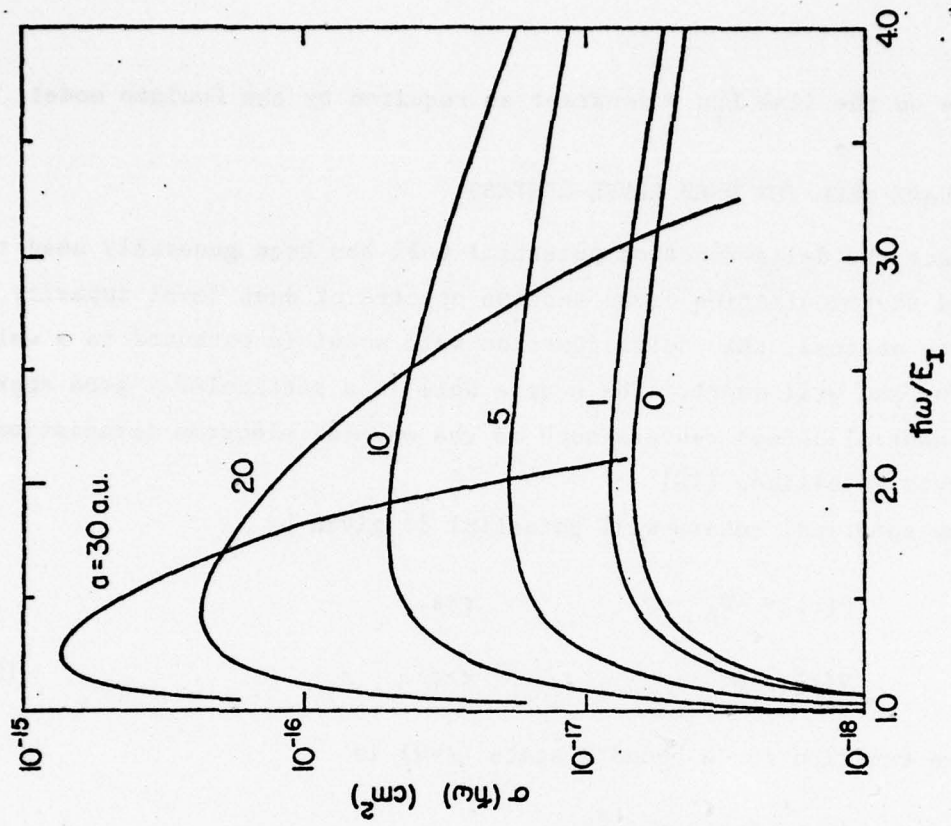


Figure 3.3.5 The effective radii versus the ionization energy for the ground states of the Group-III and Group-V impurities in silicon. The theory is based on a Coulomb potential well.

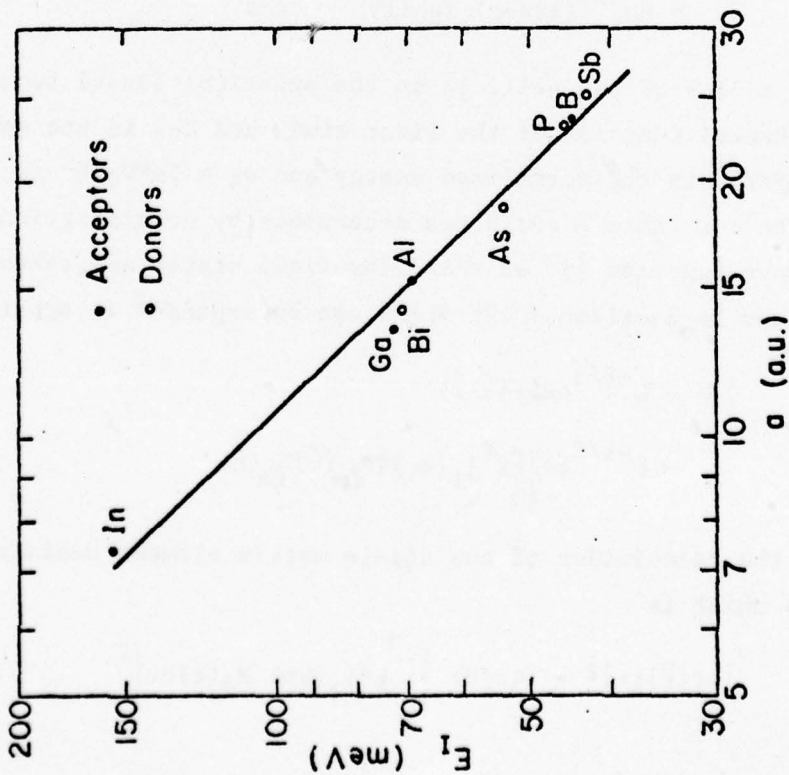


Figure 3.3.6 Photoionization cross-section spectra of the s-bound state of spherical square potential well of radius a . $E_I = 0.5$ eV, $m^* = m$, $\epsilon_0 = 12$ and $(E_{eff}/E_0) = 1$ are assumed.

obtained are on the line $E_I a = \text{constant}$ as required by the Coulomb model.

3.3.2 SQUARE WELL FOR DEEP LEVEL CENTERS

Since the delta-function potential well has been generally used to fit the observed photoionization cross-section spectra of deep level impurity with only moderate success, this delta function well model is extended to a well of finite radius and well depth. The square well is a particularly good approximation for neutral defect centers such as the one-MeV electron irradiation generated centers in silicon.[40]

The spherical square-well potential is given by

$$\begin{aligned} V(r) &= -V_0 & r < a \\ V(r) &= 0 & r > a \end{aligned} \quad (3.6)$$

and the wave function for a bound S state ($\ell=0$) is

$$\begin{aligned} |i\rangle &= R_0(\vec{r}) Y_{00}(\vec{r}) \\ &= Aj_0(r\sqrt{\epsilon+v_0}) Y_{00}(\vec{r}) & r < a \\ &= Bh_0^{(1)}(ir\sqrt{-\epsilon}) Y_{00}(\vec{r}) & r > a \end{aligned} \quad (3.7)$$

where a is the radius of the well, j_0 is the spherical Bessel function, $h_0^{(1)}$ is the spherical Hankel function of the first kind, and Y_{00} is the spherical harmonic. $\epsilon = 2m^*E/\hbar^2$ is the normalized energy and $v_0 = 2m^*V_0/\hbar^2$ is normalized well depth. The constants A and B are determined by normalization and continuity of the wave function $|i\rangle$ at $r=a$. The final states are taken to be plane wave states given by Equation (3.2) which can be expanded in spherical harmonics

$$\begin{aligned} |f\rangle &= v^{-1/2} \exp(i\vec{k}\cdot\vec{r}) \\ &= v^{-1/2} 4\pi \sum_{\ell m} i^\ell j_\ell(kr) Y_{\ell m}^*(\vec{r}) Y_{\ell m}(\vec{r}) \end{aligned} \quad (3.8)$$

to facilitate the calculation of the dipole matrix element contained in Equation (3.3) which is

$$|\langle f | \vec{r} | i \rangle|^2 = (4\pi/v) \left| \int_0^\infty r^3 j_1(kr) R_0(r) dr \right|^2 \quad (3.9)$$

The final result of the photoionization cross-section after integrating over all k of the final states in Equation (3.3) is given again by Equation (3.4) and the shape function is now

$$S(\hbar\omega) = \left(2m^*\hbar\omega k/\hbar^2 a^2\right) \left| \int_0^\infty r^3 j_1(kr) R_0(r) dr \right|^2 \quad (3.10)$$

where $k^2 = (2m^*/\hbar^2)(\hbar\omega - E_I)$. In the limit of $ka \rightarrow 0$.

$$S(\hbar\omega) = (4\hbar^2/m^*a^2) E_I^{1/2} (\hbar\omega - E_I)^{3/2} / (\hbar\omega)^3 \quad (3.11)$$

and the photoionization cross-section becomes

$$\begin{aligned} \sigma(\hbar\omega) &= \sigma_L(\hbar\omega) \\ &= [(E_{eff}/E_o)^2 (n/\epsilon_o)] (16\pi a h^2/3m^*) E_I^{1/2} (\hbar\omega - E_I)^{3/2} / (\hbar\omega)^3 \end{aligned} \quad (3.12)$$

which is the familiar result of the delta-function well given by Lucovsky. [17]

The integral of Equation (3.9) can be evaluated in close form but is long and complicated. A family of normalized curves is shown in Figure 3.3.6 to illustrate the shape of the photoionization spectra as a function of well size. It is evident that the spectra becomes more sharply peaked and the peak moves toward the threshold as the well radius is increased. Such a sharply peaked spectra has been observed for some one-MeV electron irradiation induced centers in silicon as indicated in Figure 3.3.7. This is consistent with the model that these electron irradiation induced centers are extended lattice defects which are electrically neutral and can be characterized by a square well. [40]

In Figure 3.3.8, the photoionization data of In in silicon is fitted to a square well. This is as good a fit as the Coulomb well, shown in Figure 3.3.4 and both the square well and the Coulomb well fit much better than the delta-function well. This result illustrates that the photoionization spectra is mainly influenced by the bound state wave function away from the imperfection center and it does not probe the central cell part of the imperfection potential and cannot distinguish a Coulomb well from a square well. It does show that the commonly used delta-function well is oversimplified and too compact for most imperfection centers.

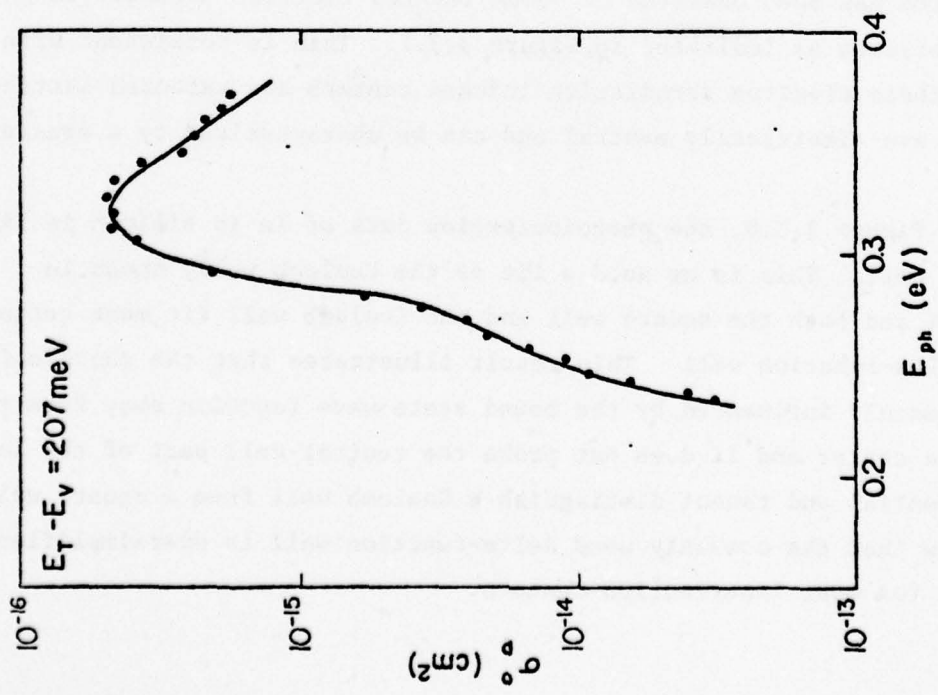


Figure 3.3.7 Hole photoionization cross-section of the $E_T - E_V = 207$ meV defect generated by one-Mev electron irradiation.

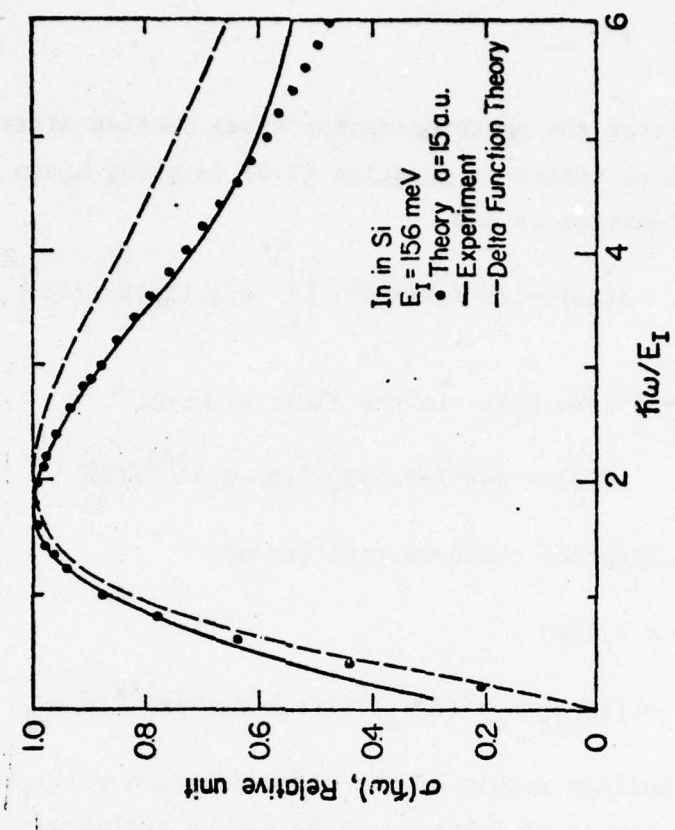


Figure 3.3.8 Spectral dependence of the photoionization cross-section of In in Si. The theory (solid dots) is based on a spherical square potential well of radius $a=15$ a.u. (1 a.u.=0.529 Å) and the theory (dashed curve) is based on the delta function potential well of Lucovsky.

3.3.3 COULOMB WELL FOR TWO-ELECTRON CENTERS

The photoionization cross-section for a two-electron center was obtained using the Helium-like model.[35] It was shown that the experimental data exhibit a Lorentzian line shape.

In the electric dipole approximation the photoionization cross-section for a two electron neutral center is given by an equation similar to (3.3):

$$\sigma_I^{(0)}(\hbar\omega) = [(\mathbf{E}_{\text{eff}}/\mathbf{E}_0)^2(n/\epsilon_0)](4\pi^2a/3)\hbar\omega \sum_{\mathbf{f}} |\langle \mathbf{f} | \vec{\mathbf{r}}_1 + \vec{\mathbf{r}}_2 | i \rangle|^2 \delta(\mathbf{E}_f - \mathbf{E}_i - \hbar\omega) \quad (3.13)$$

where n is the optical index of refraction, ϵ_0 is the optical dielectric constant, $\mathbf{E}_{\text{eff}}/\mathbf{E}_0$ is the effective electric field at the center, $a=e^2/hc$ is the fine structure constant. Here $|i\rangle$ is the initial state or ground state of the neutral center, and $|\mathbf{f}\rangle$ is the final state where one of the electrons is in the continuum state and the other electron is in the ground state of the singly ionized center. In the helium-like model, the initial ground state for the two-electron center is assumed to be

$$|i\rangle = (1/\pi a^3) \exp[-(\mathbf{r}_1 + \mathbf{r}_2)/a] \quad (3.14)$$

and the final continuum state is written as

$$|\mathbf{f}\rangle = |\vec{k}\rangle = (2\pi b^3 v)^{-1/2} \{ \exp[(-\mathbf{r}_1/b) + i\vec{k} \cdot \vec{\mathbf{r}}_1] + \exp[(-\mathbf{r}_2/b) + i\vec{k} \cdot \vec{\mathbf{r}}_2] \} \quad (3.15)$$

where a is the effective Bohr radius of the two-electron neutral center, and b is the radius of the one-electron singly ionized center. v is the volume of normalization and \vec{k} is the wave vector which characterizes the electron in the continuum. The summation in Equation (3.13) then becomes a sum over all the \vec{k} values. Using Equations (3.14) and (3.15) to calculate the electric dipole matrix elements in Equation (3.13), then

$$\sigma_I^{(0)}(\hbar\omega) = (\mathbf{E}_{\text{eff}}/\mathbf{E}_0)^2(n/\epsilon_0)(4\pi a/3)a^2 S^{(0)}(\hbar\omega) \quad (3.16a)$$

where the spectral dependence is contained in the dimensionless shape function

$$S^{(0)}(\hbar\omega) = 512 \left(\frac{2m*a^2}{h^2} \right) \hbar\omega \left(\frac{b}{a} \right)^3 \left[\frac{2}{(b/a+1)} \right]^6 \frac{[(2m*a^2/h^2)(\hbar\omega - E_I^{(0)})]^{3/2}}{[1 + (2m*a^2/h^2)(\hbar\omega - E_I^{(0)})]^6} \quad (3.16b)$$

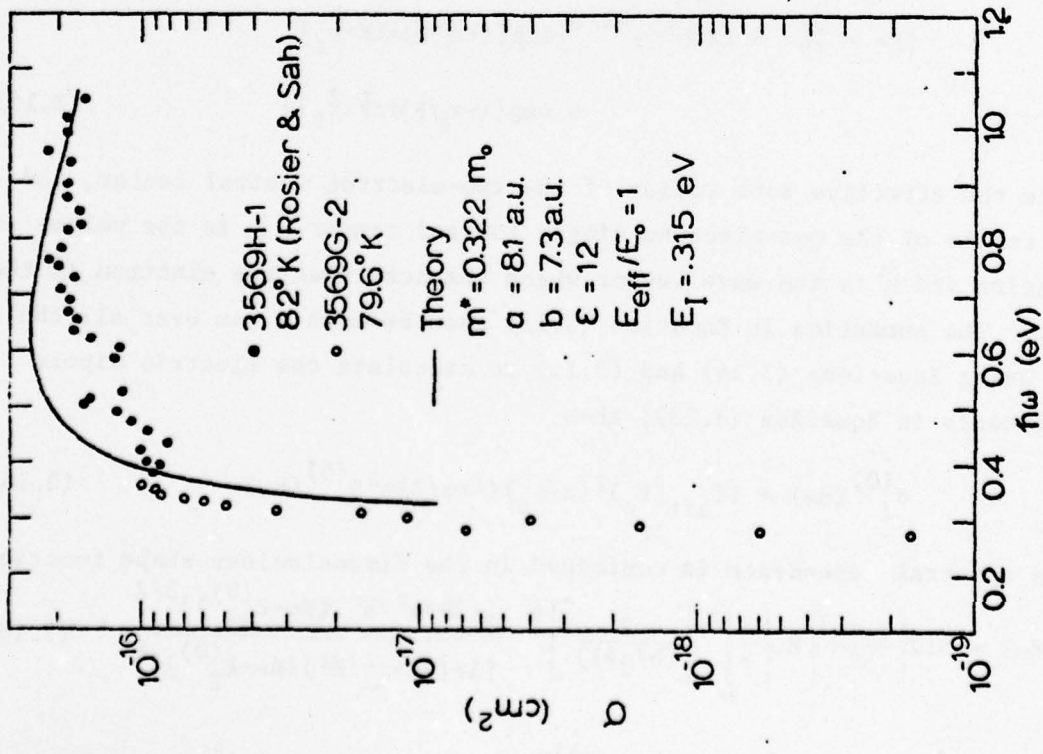


Figure 3.3.9 Photoionization cross section of neutral sulfur centers in silicon. The solid dots were taken from Ref. 33.

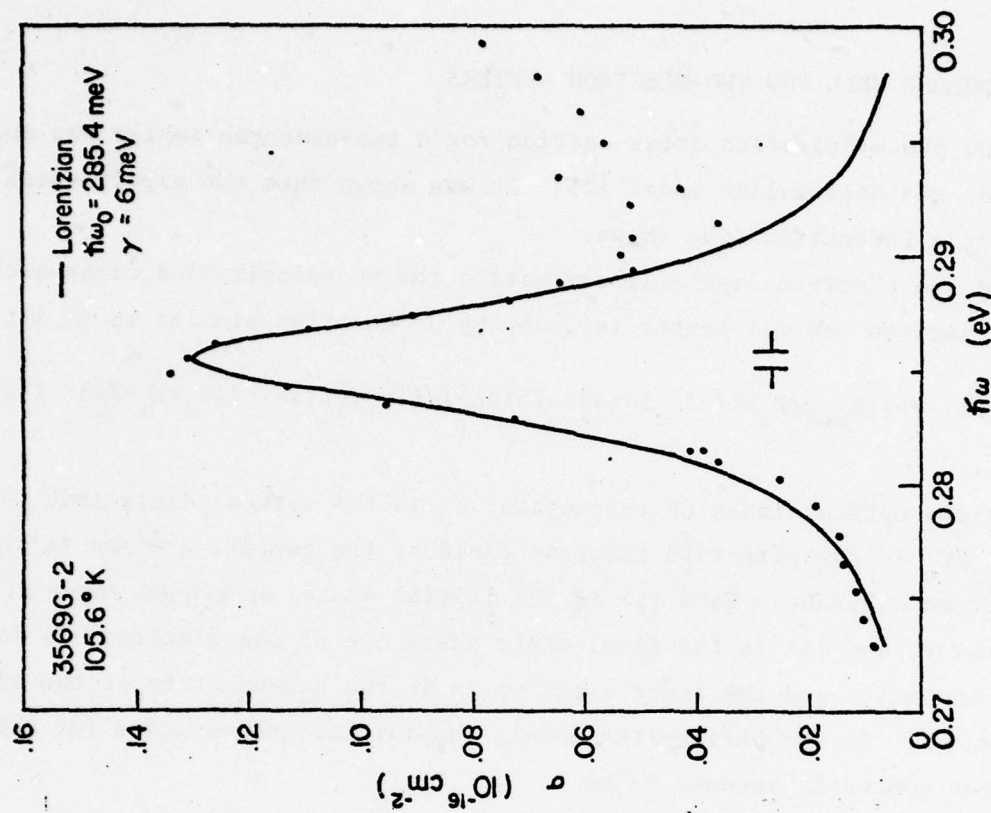


Figure 3.3.10 Linear plot of the 0.285-eV peak, indicating a Lorentzian line shape with half-width of 6 meV.

Here $E_I^{(0)}$ is the one-electron ionization energy of the neutral center.

After the ionization of one of the electrons from the helium-like neutral center, the center becomes singly ionized and is hydrogen-like. The photoionization cross-section for the singly ionized or one-electron center can be calculated from Equation (3.3) using $|i\rangle = \sqrt{1/\pi b^3} \exp(-r/b)$ for the initial ground state, and $|f\rangle = |\vec{k}\rangle = \sqrt{1/8} \exp(\pm i\vec{k}\cdot\vec{r})$ for the final continuum state. The results were given by Equations (3.4) and (3.5) and with proper notation changes we have

$$\sigma_I^{(+)}(\hbar\omega) = \left[\left(\frac{E_{\text{eff}}}{E_0} \right)^2 \frac{n}{\epsilon} \right] \frac{4\pi a}{3} b^2 S^{(+)}(\hbar\omega), \quad (3.17a)$$

with

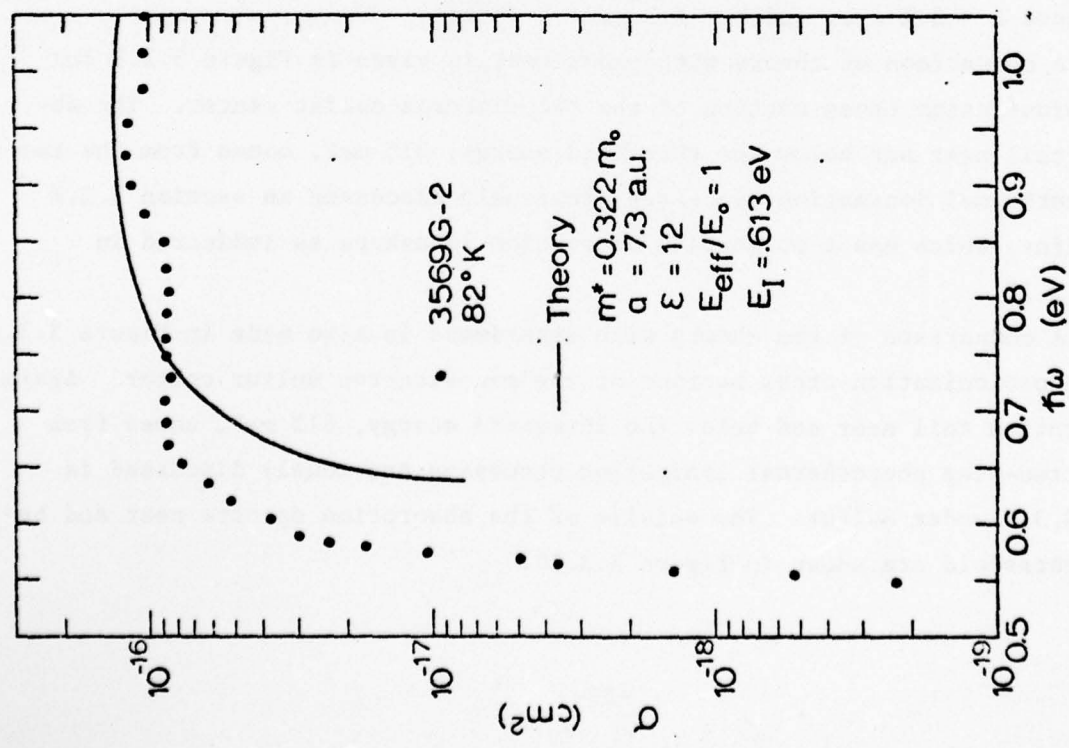
$$S^{(+)}(\hbar\omega) = 256 \left(\frac{2m*b^2}{h^2} \right) \hbar\omega \frac{[(2m*b^2/\hbar^2)(\hbar\omega - E_I^{(+)})]^{3/2}}{[1 + (2m*b^2/\hbar^2)(\hbar\omega - E_I^{(+)})]^6} \quad (3.17b)$$

where $E_I^{(+)}$ is the ionization energy of the singly ionized center.

In order to evaluate the cross-sections from Equations (3.16) and (3.17) for a given center, we need to know the effective Bohr radii a and b for the neutral and the singly ionized centers. At present these values are available only for sulfur centers in silicon.[42] From variational calculations of the energy levels, the effective Bohr radii for sulfur centers in silicon were $a = 8.1$ a.u. and $b = 7.3$ a.u.

A comparison of theory with experiment is given in Figure 3.3.9 for the photoionization cross section of the two-electron sulfur center. The absorption tail near and below the threshold energy, 315 meV, comes from the two-step photothermal ionization processes previously discussed in section 3.3.7 under Sulfur, which has a Lorentzian absorption lineshape as indicated in Figure 3.3.10.

A comparison of the theory with experiment is also made in Figure 3.3.11 for the photoionization cross section of the one-electron sulfur center. Again the absorption tail near and below the threshold energy, 613 meV, comes from the many two-step photothermal ionization processes previously discussed in section 3.3.7 under Sulfur. The details of the absorption spectra near and below the threshold are shown in Figure 3.3.12.



-58-

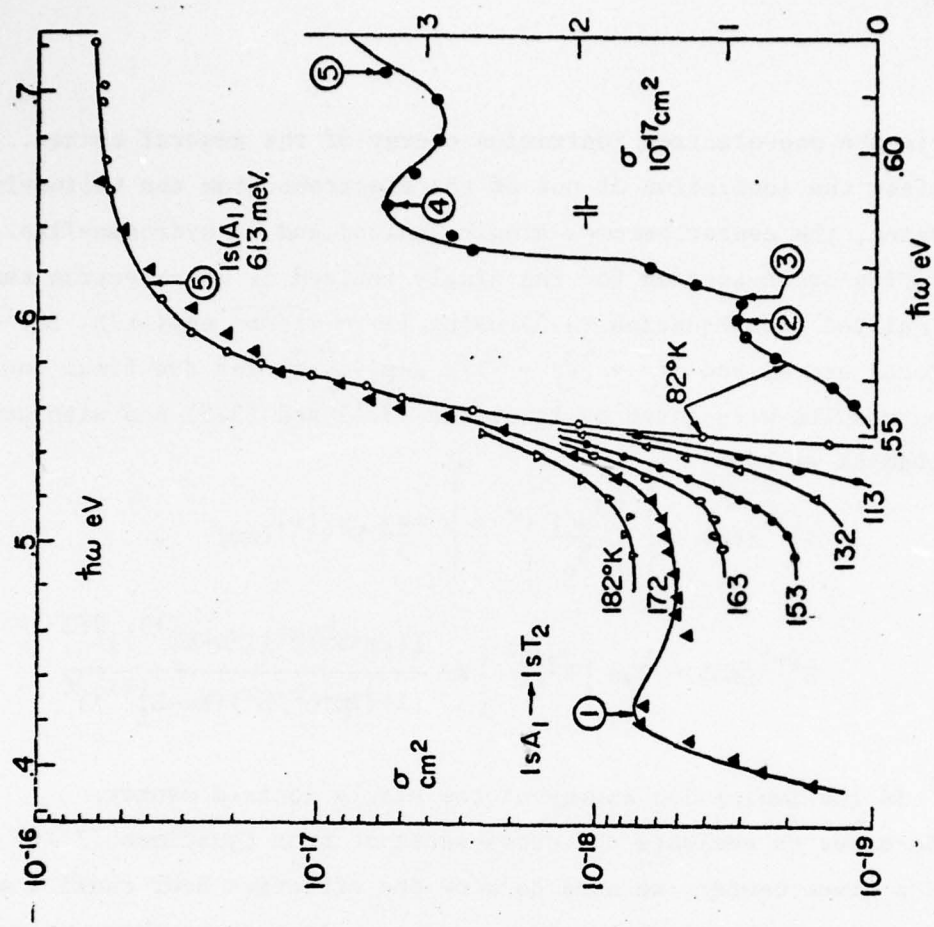


Figure 3.3.11 Photoionization cross section of singly ionized sulfur centers in silicon. The experimental values were taken from Ref. 33.

Figure 3.3.12 Highly sensitive measurement of the photoionization cross section from the optical emission rate data of the capacitance transient from electrons trapped at the deep sulfur donor center in silicon at 613 meV below the silicon conduction band edge [34].

IV. CONCLUSIONS

The material parameters which control the performance of an extrinsic semiconductor IR detector are delineated. These are: (i) the carrier mobilities, (ii) the thermal capture and emission rates and the optical emission rates or photoionization cross-sections of electrons and holes trapped at the recombination and optical centers, and (iii) the concentration of these centers. These centers are either impurities, defects, or impurity-defect complexes.

Mobility studies described in chapter II of this report show that electron and hole mobilities at high impurity concentrations are limited by scattering of the randomly located impurity ions. A comparison of the experimental data with several theoretical models indicated that there is no ion position correlation. Position correlation would reduce random scattering and increase mobility, allowing the use of high concentrations of optically active ions to increase IR detector sensitivity.

Fabrication of silicon extrinsic IR detectors requires high temperature processing during which impurities and defects are inevitably introduced. The presence of minute amounts of impurities and defects will drastically affect the detector characteristics such as detection sensitivity, bandwidth or response speed, radiation sensitivity and life. Previous classical techniques, such as the Hall effect and the photoconductivity methods, are not sensitive nor unambiguous enough to detect the presence of these impurity and defect centers. New methods, using the transient capacitance measurement of a semiconductor space charge layer, have been developed to detect and characterize these new centers. A summary of these methods is given in section 3.1.

Many impurity and defect centers in silicon have been studied and reported in section 3.2, including phosphorus, bismuth, gold, magnesium, silver, cobalt, chromium, sulfur, tantalum, zinc, aluminum-oxygen complexes, thermally generated donors, and defect centers generated by energetic ions. In principle, the impurity centers can be introduced or eliminated in controlled ways during device fabrication. However, the impurity-oxygen complexes and the centers generated thermally during high temperature fabrication processes and the centers generated during ion implantation, if not eliminated or controlled, may become detrimental to the silicon extrinsic IR detector performance. Thus, it

seems highly desirable to undertake a systematic measurement program to characterize these impurity and defect centers using the highly sensitive capacitance transient techniques. Such a study may provide not only information on new optical centers useful in extrinsic silicon detector applications, but also indicate fabrication conditions to make their introduction and elimination predictable.

REFERENCES

1. H. Melchior, M. B. Fisher and F. R. Arams, "Photodetectors for optical communication systems," Proc. IEEE, v48, 1466-1486, 1 October 1970.
2. R. J. Keyes and T. M. Quist, "Low-level coherent and incoherent detection in the infrared," Semiconductors and Semimetals, v5, 321-359, Chapter 8, edited by Willardson and Beer, Academic Press, 1970.
3. K. Y. Tsao and C. T. Sah, "Temperature dependence of resistivity and hole conductivity mobility in p-type silicon," Solid-State Electronics, v19, 949-953, 01 November 1976.
4. Thomas J. Woodley and C. T. Sah, "Deionization effect on the evaluation of hole mobility in p-Si," Solid-State Electronics, v20, no. 4, April 1977.
5. J. C. Irvin, "Resistivity of bulk silicon and of diffused layers in silicon," Bell Syst. Tech. J., v41, 387-397 (1962); S. M. Sze and J. C. Irvin, "Resistivity, mobility and impurity levels in GaAs, Ge, and Si at 300°K," Solid-State Electronics, v11, 599-605 (1958).
6. J. M. Ziman, Principles of the Theory of Solids, Cambridge University Press (1964), Chapter 5.
7. R. B. Dingle, "Scattering of electrons and holes by charged donors and acceptors in semiconductors," Phil. Mag. v46, 831-840, 1 August 1955.
8. R. Mansfield, "Impurity scattering in semiconductors," Proc. Phys. Soc. (London) B, v69, 76-82, 1956.
9. E. M. Omelyanovskii, V. I. Fistful and M. G. Milvidskii, "Electron mobility in heavily doped silicon," Soviet Phys.-Solid State, v5, 676-680, 1 September 1963.
10. C. T. Sah, unpublished.
11. P. W. Chapman, O. N. Tuft, J. D. Zook and D. Long, "Electrical properties of heavily doped Si," J. Applied Phys., v34, 3291-3295, 1 November 1963.
12. C. T. Sah, "Studies of bulk and interface imperfections in semiconductors," Sherman Fairchild Lecture, Lehigh University, November 7, 1973; C. T. Sah, "Bulk and interface imperfections in semiconductors," Solid-State Electronics, v19, 975-990, December 1976.
13. C. T. Sah, "Studies of recombination centers in silicon," Invited Seminar, Bell Telephone Laboratory, Allentown, November 8, 1973.
14. C. T. Sah, "Electron-hole recombinations in semiconductors," Graduate Seminar in Electrical Engineering, University of Leuven, Belgium, February 5, 1975.

15. C. T. Sah, "Detection of recombination centers from the transient response of the space charge layer capacitance," Invited Tutorial Paper, National Workshop on Low Cost Polycrystalline Silicon Solar Cells, Southern Methodist University, Dallas, May 18, 1976, published in the conference proceedings.
16. C. T. Sah, "Detection of recombination centers in solar cells from junction capacitance transients," Graduate Seminar, Institute of Energy Conversion, University of Delaware, October 15, 1976.
17. C. T. Sah, "Detection of recombination centers in semiconductors by junction current and capacitance transient techniques," IEEE Professional Society on Electron Devices, Minneapolis Chapter, January 26, 1977.
18. C. T. Sah, "Detection of defect and impurity centers in semiconductors by steady-state and transient junction capacitance and current techniques," Silicon Materials Science and Technology Symposium, The Electrochemical Society, May 13, 1977, Philadelphia, PA, Published in Semiconductor Silicon 1977, Proceedings, 868-893, The Electrochemical Society.
19. C. T. Sah, "Detection of recombination centers in solar cells from junction capacitance transients, IEEE Trans. on Elect. Dev., vED-24, no. 4, 410-419, April 1977.
20. C. T. Sah and J. W. Walker, "Thermally stimulated capacitance for shallow majority-carrier traps in the edge region of semiconductor junctions," Appl. Phys. Letts., v22, no. 8, 384-385, 15 April 1973.
21. C. T. Sah, C. T. Wang and S. H. Lee, "Junction edge region thermally stimulated capacitance (TSCAP) of n -Si doped with phosphorus and bismuth," Appl. Phys. Letts., v25, no. 9, 523-524, 1 November 1974.
22. C. T. Sah, L. Forbes, L. L. Rosier and A. F. Tasch, Jr., "Thermal and optical emission and capture rates and cross sections of electrons and holes at imperfection centers in semiconductors from photo and dark junction current and capacitance experiments," Solid-State Electronics, v13, 759-788, June 1970.
23. A. Neugroschel and C. T. Sah, "Concentration profiles of recombination centers in semiconductor junction evaluated from capacitance transients," IEEE Trans. on Elect. Dev., vED-23, no. 9, 1069-1074, September 1976.
24. R. L. Marchand and C. T. Sah, submitted for publication.
25. This will be detailed in a future Scientific Report.
26. C. T. Sah and C. T. Wang, "Experiments on the origin of process-induced recombination centers in silicon," J. Appl. Phys., v46, no. 4, 1767-1776, April 1975.
27. R. L. Marchand and C. T. Sah, "Studies of thermally induced deep levels in Al-doped silicon," J. Appl. Phys., v48, no. 1, 336-341, 01 January 1977.
28. R. L. Marchand, A. R. Stivers and C. T. Sah, "Recombination centers in aluminum-doped silicon diffused in high phosphorus concentration," J. Appl. Phys., v48, no. 6, 2576-2580, 01 June 1977.

29. L. D. Yau, C. F. Smiley and C. T. Sah, "Thermal emission rates and activation energies of electrons and holes at silver centers in silicon," Phys. Stat. Sol. (a) v13, 457-464, 16 October 1972.
30. L. D. Yau and C. T. Sah, "Measurement of trapped-minority-carrier thermal emission rates from Au, Ag, and Co traps in silicon," Appl. Phys. Letts., v21, no. 4, 157-158, 15 August 1972.
31. L. D. Yau, W. W. Chan, and C. T. Sah, "Thermal emission rates and activation energies of electrons and holes at cobalt centers in silicon," Phys. Stat. Sol. (a) v14, 655-662, 16 December 1972.
32. L. L. Rosier and C. T. Sah, "Thermal emission and capture of electrons at sulfur centers in silicon," Solid-State Elect., v14, 41-54, January 1971.
33. L. L. Rosier and C. T. Sah, "Photoionization of electrons at sulfur centers in silicon," J. Appl. Phys., v42, no. 10, 4000-4005, September 1971.
34. C. T. Sah, T. H. Ning, L. L. Rosier, and L. Forbes, "Photothermal ionization via excited states of sulfur donor in silicon," Solid State Communications, v9, 917-920, 15 June 1971.
35. T. H. Ning and C. T. Sah, "Photoionization cross sections of a two-electron donor center in silicon," Phys. Rev. B, v14, no. 6, 2528-2533, 15 September 1976.
36. J. M. Herman, III and C. T. Sah, "Thermal ionization rates and energies of holes at the double acceptor zinc centers in silicon," Phys. Stat. Sol. (a) v14, 405-415, 16 December 1972.
37. J. M. Herman, III and C. T. Sah, "Photoionization cross sections of holes at zinc centers in silicon," J. Appl. Phys., v44, no. 3, 1259-1262, March 1973.
38. J. M. Herman, III and C. T. Sah, "Thermal capture of electrons and holes at zinc centers in silicon," Solid-State Electronics, v16, 1133-1139, 1 October 1973.
39. T. H. Ning and C. T. Sah, "Multivalley effective-mass approximation for donor states in silicon I. Shallow-level group-V impurities," Phys. Rev. B, v4, no. 10, 3469-3481, 15 November 1971.
40. J. W. Walker and C. T. Sah, "Properties of one-MeV-electron-irradiated defect centers in silicon," Phys. Rev. B, v7, 4587-4605, 15 May 1973; "Spherical-square-well defect-potential model for one MeV electron irradiated defects in silicon," Phys. Rev. B, v8, 5597-5603, 15 December 1973.
41. G. Lucovsky, "On the photoionization of deep impurity centers in semiconductors," Solid-State Communications, v3, 299-302, 1 September 1965.
42. T. H. Ning and C. T. Sah, "Multivalley effective-mass approximation for donor states in silicon II. Deep-level group-VI double-donor impurities," Phys. Rev. B, v4, no. 10, 3483-3488, 15 November 1971.

APPENDIX A

FORMER AND CURRENT FACULTY MEMBERS ASSOCIATED WITH C, T, SAH

1. Shuichi Sato, Research Associate, 1967-1969
Formerly at Research Laboratory, Sony Corporation, Japan; Currently with Tektronix, Oregon.
2. Leonard Forbes, Research Associate, 1969
Currently Associate Professor of Electrical Engineering, University of California, Davis
3. L. D. Yau, Assistant Professor, 1971-1973
Currently member of Technical Staff, Bell Telephone Laboratories, Murray Hill, NJ
4. Hisao Katto, Visiting Fellow, 1971-1972
Currently at Central Research Laboratory, Hitachi Corporation, Japan
5. H. S. Fu, Research Assistant Professor, 1972-1973
Currently member of Technical Staff, Central Research Laboratory, Texas Instruments, Inc., Dallas, Texas
6. T. H. Ning, IBM Postdoctoral Fellow, 1972 and Assistant Professor, 1972-1973
Currently member of Technical Staff, Thomas J. Watson Research Center, International Business Machine Corp., Yorktown Heights, NY
7. Karl Hess, Visiting Assistant Professor, 1973-1974
Currently Associate Professor of Physics, Department of Physics and Boltzmann Institute, University of Vienna
8. S. H. Lee, Research Associate, 1973-1975
Currently at Naval Research Laboratory, Washington, D. C.
9. Arnost Neugroschel, Research Associate, 1973-1975
Currently Assistant Professor of Electrical Engineering, University of Florida, Gainesville, Florida
10. C. T. Wang, Research Associate, 1973-1974
Currently at Hewlett-Packard Co., Loveland, CO
11. M. J. McNutt, Research Associate, 1974, Assistant Professor, 1975-1977
12. Kenji Miyata, Visiting Fellow, 1974-1975
Currently at Semiconductor Division, Hitachi Corporation, Japan
13. Herman Maes, Belgium-American Fellow, 1974-1975, Research Associate, 1975
Currently Assistant Professor of Electrical Engineering, University of Leuven, Belgium
14. K. Y. Tsao, Research Associate, 1974-1975
15. Raymond Marchand, IBM Postdoctoral Fellow, 1975-1976, Assistant Professor, 1976-1977

APPENDIX B

GRADUATE STUDENTS AND THESIS TITLES DIRECTED BY C. T. SAH DEGREE DATE AND AFFILIATION

1. Henry C. H. Pao, Ph.D., Electrical Engineering, December 1965

THEORETICAL AND EXPERIMENTAL INVESTIGATIONS OF METAL OXIDE SEMICONDUCTOR TRANSISTORS

Formerly employed by Sperry Research Center, Sudbury, MA, Raytheon Co., Newton, MA and by Fairchild Semiconductor, Palo Alto, CA

2. S. Y. Wu, Ph.D. in Electrical Engineering, May 1966

THEORETICAL AND EXPERIMENTAL STUDIES OF CURRENT SATURATION PHENOMENA AND LOW FREQUENCY GENERATION NOISE IN JUNCTION-GATE FIELD-EFFECT TRANSISTORS

Currently employed by Westinghouse Research Center, Pittsburgh, PA

3. Frank H. Hielscher, Ph.D., Electrical Engineering, August 1966

1/f SURFACE NOISE IN MOS TRANSISTORS

Formerly employed by Sprague Electric Co., North Adames, MA and currently Associate Professor in Electrical Engineering, Lehigh University, Bethlehem, PA

4. Robert F. Pierret, Ph.D., Physics, August 1966

EFFECTIVE MOBILITY THEORY IN SILICON SURFACE CHANNELS AS MEASURED BY THE MOS TRANSISTORS

Currently employed as Associate Professor of Electrical Engineering at Purdue University, West Lafayette, IN

5. Robert F. Pfeifer, M.S., Electrical Engineering, January 1966

A DISTORTION ANALYSIS OF THE METAL-OXIDE-SEMICONDUCTOR TRANSISTOR

Formerly employed by the Westinghouse Research Center, Pittsburgh, PA and currently employed by National Cash Register Co., Dayton, OH

6. D. R. Collins, Ph.D., Electrical Engineering, November 1966

EXPERIMENTAL INVESTIGATIONS OF THE ELECTRONIC PROPERTIES OF THE OXIDIZED SILICON SURFACE USING MOS CAPACITORS

Currently employed by the Semiconductor Components Division, Texas Instruments, Inc., Dallas, TX

7. Dieter K. Schroder, Ph.D., Electrical Engineering, February 1968
IMPEDANCE AND OTHER PROPERTIES OF GOLD DOPED SILICON P-N JUNCTIONS
Currently employed by Westinghouse Research Center, Pittsburgh, PA
8. T. L. Chiu, Ph.D., Electrical Engineering, August 1968
EXPERIMENTS AND THEORY ON THE CHARACTERISTICS OF METAL-OXIDE-SEMICONDUCTOR TRANSISTORS IN THE CURRENT SATURATION RANGE
Formerly employed by IBM Components Division, East Fishkill, NY and Cambridge Memory, Inc., Wraplinger Falls, NY
9. L. D. Yau, Ph.D., Electrical Engineering, February 1969
EXPERIMENTS AND THEORY OF THE GENERATION-RECOMBINATION NOISE IN MOS TRANSISTORS
Formerly Assistant Professor of Electrical Engineering at the University of the Philippines (1969-1970), Assistant Professor of Electrical Engineering, University of Illinois, Urbana (1970-1971), and currently employed by Bell Telephone Labs., Murray Hill, NJ
10. A. F. Tasch, Jr., Ph.D., Physics, June 1969
STUDIES OF THE THERMAL AND OPTICAL EMISSION RATES AND CROSS SECTIONS OF CARRIERS AT GOLD ACCEPTOR CENTER USING THE IMPURITY PHOTOVOLTAIC EFFECT
Currently employed at the Central Research Laboratory, Texas Instruments, Inc., Dallas, TX
11. J. R. Edwards, Ph.D., Physics, December 1969
STUDIES OF SURFACE SCATTERING MECHANISMS AT THERMALLY OXIDIZED SILICON SURFACE
Formerly employed by the Bell Telephone Laboratories, Allentown, PA and currently employed by American Microsystem Inc., Santa Clara, CA
12. L. L. Rosier, Ph.D., Physics, December 1969
ELECTRICAL AND OPTICAL PROPERTIES OF SULFUR IN SILICON
Currently employed as Manager of Magnetic Bubble Devices at the IBM Research Center, San Jose, CA
13. L. Forbes, Ph.D., Electrical Engineering, December 1969
THERMAL AND OPTICAL EMISSION AND THERMAL CAPTURE OF ELECTRONS AND HOLES AT GOLD CENTERS IN SILICON
Formerly employed at the IBM Components Division, East Fishkill, NY and Assistant Professor of Electrical Engineering, University of Arkansas and currently Associate Professor of Electrical Engineering, University of California, Davis, CA

14. H. S. Fu, Ph.D., Electrical Engineering, February 1971

SURFACE 1/f NOISE ON OXIDIZED SILICON

Formerly Research Assistant Professor in Electrical Engineering at the University of Illinois and currently employed by the Texas Instruments, Inc., Dallas, TX

15. W. R. Hunter, Ph.D., Physics, June 1971

THIN OXIDE MOS CAPACITOR STUDIES OF FAST SURFACE STATES

Currently employed by the IBM Thomas J. Watson Research Center, Yorktown Heights, NY

16. R. F. Pfeifer, Ph.D., Electrical Engineering, June 1971

HIGH FREQUENCY CHARACTERISTICS OF TRANSISTOR CURRENT GAIN

Formerly employed by the Westinghouse Research Center, Pittsburgh, PA and currently employed by the National Cash Register, Inc., Dayton, OH

17. T. H. Ning, Ph.D., Physics, June 1971

MULTI-VALLEY EFFECTIVE-MASS APPROXIMATION OF GROUP-V AND GROUP-VI DONOR STATES IN SILICON

Formerly IBM Postgraduate Fellow (1971) and Assistant Professor of Electrical Engineering (1972), University of Illinois, Urbana, and currently employed by The IBM Thomas J. Watson Research Center, Yorktown Heights, NY

18. R. E. Anderson, M.S., Electrical Engineering, January 1970

USE OF PHASE-SENSITIVE NULL DETECTORS FOR ADMITTANCE BRIDGES

Currently employed by Sandia Corp., Albuquerque, NM

19. G. Panigrahi, M. S., Electrical Engineering, June 1970

SOLUTIONS OF POISSON'S EQUATION FOR SEMICONDUCTORS WITH NON-CONSTANT DOPING PROFILES AND A SAMPLE APPLICATION

Currently with Burrough Corporation

20. C. T. Ho, M.S., Electrical Engineering, June 1970

FURTHER INVESTIGATION OF THE LARGE SIGNAL BEHAVIOR OF METAL OXIDE SEMICONDUCTOR CAPACITOR

Currently employed by the IBM Components Division at East Fishkill, NY

21. K. Jain, M.S., Electrical Engineering, August 1970

LARGE SIGNAL EQUIVALENT CIRCUIT MODELS OF SEMICONDUCTORS

Currently a Research Associate in Electrical Engineering at M.I.T.

22. W. W. Chan, M.S., Electrical Engineering, February 1971

A STUDY OF DEEP ENERGY LEVELS IN ION IMPLANTED SILICON

Currently employed by Texas Instruments, Inc., Dallas, TX

23. L. L. Tschopp, Ph.D., Physics, February 1972

SCATTERING OF ELECTRONS BY SURFACE STATES ON OXIDIZED SILICON

Currently employed as Research Associate in Biophysics at Indiana University, Indianapolis, IN

24. D. R. Eaton, Ph.D., Physics, October 1972

PROPERTIES OF SILICON-SILICON DIOXIDE INTERFACE STATES IN THIN OXIDE MOS STRUCTURES

Formerly employed by the Bell Telephone Laboratories, Allentown, PA; currently at Hewlett-Packard Company, Loveland, CO

25. J. M. Herman, III, Ph.D., Electrical Engineering, October 1972

HIGH FIELD EMISSION AND CAPTURE OF ELECTRONS AND HOLES AT ZINC CENTERS IN SILICON

Formerly employed as Assistant Professor of Electrical Engineering, Texas A & M University, College Station, Texas, and currently employed by the Texas Instruments, Inc., Dallas, TX

26. J. W. Walker, Ph.D., Physics, January 1973

PROPERTIES OF ONE-MeV-ELECTRON-IRRADIATED DEFECT CENTERS IN SILICON

Currently employed by the Texas Instruments, Inc., Dallas, TX

27. C. T. Smiley, M.S., Electrical Engineering, June 1972

AC ADMITTANCE OF GOLD-DOPED P+N JUNCTION

Currently employed by the Gates Radio Company, Quincy, IL

28. Sokrates T. Pantelides, Ph.D., Physics, June 1973

THEORY OF POINT-IMPERFECTION STATES IN SEMICONDUCTORS

Formerly employed as a Research Associate at the W. W. Hansen Laboratory of Applied Physics of Stanford University and currently employed by the IBM Watson Research Laboratory, Yorktown Heights, NY

29. Falke Hennig, Ph.D., Electrical Engineering, September 1974

EMISSION AND CAPTURE OF ELECTRONS AND HOLES AT GOLD CENTERS IN SILICON AT THERMAL EQUILIBRIUM

Currently employed by the Fairchild Semiconductor Laboratory, Palo Alto, CA

30. Michael J. McNutt, Ph.D., Electrical Engineering, September 1974

THEORY AND EXPERIMENTS ON HIGH FREQUENCY METAL-OXIDE-SEMICONDUCTOR CAPACITANCE

Currently employed as Assistant Professor of Electrical Engineering at the University of Illinois, Urbana

31. P. S. Bachert, M.S., Electrical Engineering, December 1974

HIGH-FREQUENCY CAPACITANCE-VOLTAGE ANALYSIS OF MOS SURFACE STATES

Currently employed by the Motorola Inc., Chicago, IL

32. J. W. Holtkamp, M.S., Electrical Engineering, September 1975

DIFFERENTIAL EQUATION SOLUTION OF METAL-OXIDE-SEMICONDUCTOR CAPACITANCE

Currently employed by the Naval Avionics Laboratory, Indianapolis, IN

33. Mon-Yen Tsai, M.S., Electrical Engineering, September 1975

ANALYSES OF THE BASE TRANSPORT FACTOR OF HIGH FREQUENCY TRANSISTORS

34. Ching-Ho Chan, M.S., Electrical Engineering, September 1975

APPLICATION OF EQUIVALENT CIRCUIT MODEL TO THE STUDY OF PROPERTIES OF GOLD IN N-SILICON

Currently employed as research assistant at the Solid State Electronics Laboratory, University of Illinois, Urbana

35. Mark J. Pavicic, M.S., Electrical Engineering, December 1975

HIGH-FREQUENCY CAPACITANCE-VOLTAGE CHARACTERISTICS OF MOS CAPACITORS WITH A REALLY INHOMOGENEOUS OXIDE CHARGES

Currently employed by Texas Instruments, Inc., MA

36. Thomas Y. Lo, Ph.D., Electrical Engineering, January 1977

COMPUTER AUTOMATED ELECTRICAL CHARACTERIZATION OF SEMICONDUCTOR DEVICES

Currently Assistant Professor of Electrical Engineering, Chung Yuan University, Taiwan, Republic of China

CURRENT GRADUATE STUDENTS

37. Bob C. C. Shiue

38. Mark T. Bohr

39. Phil C. H. Chan

40. Robin W. K. Cheung

- 41. James F. Detry
- * 42. Allen P. I. Ho
- 43. Alan R. Stivers
- * 44. Thomas J. Woodley

CURRENT UNDERGRADUATE STUDENTS

- 45. Arthur E. Brosius
- 46. Patricia A. Hall
- 47. William C. Moody
- 48. Roger N. Switzer

* Doctoral thesis near completion.

APPENDIX C

PUBLICATION LIST

1. C. T. Sah and H. S. Fu
Current and capacitance transient responses of MOS capacitor. I. General theory and applications to initially depleted surface with surface states
Phys. Stat. Sol. (a), v11, 297-310, 16 May 1972
2. J. W. Walker and C. T. Sah
Properties of 1 MeV electron-irradiated defect centers in p-type silicon
Phys. Stat. Sol. (a), v11, 513-522, 16 June 1972
3. C. T. Sah
Differential d.c. conductance of a p-n junction space-charge region
Electronics Letters, v8, 355, 13 July 1972
4. D. H. Eaton and C. T. Sah
Frequency response of Si-SiO₂ interface states on thin oxide MOS capacitors
Phys. Stat. Sol. (a) v12, 95-109, 16 July 1972
5. C. T. Sah and L. D. Yau
Measurements of trapped-minority-carrier thermal emission rates from Au, Ag and Co traps in silicon
Appl. Phys. Letts., v21, 157-158, 15 August 1972
6. C. T. Sah, T. H. Ning and L. L. Tschopp
The scattering of electrons by surface oxide charges and by lattice vibrations at the silicon-silicon dioxide interface
Surface Science, v32, 561-575, 1 September 1972
7. L. D. Yau, C. F. Smiley and C. T. Sah
Thermal emission rates and activation energies of electrons and holes at silver centers in silicon
Phys. Stat. Sol. (a), v13, 457-464, 16 October 1972
8. Hisao Katto and C. T. Sah
Frequency response of the surface state admittance in weakly inverted thin SiO₂-Si MOS capacitors
Phys. Stat. Sol. (a), v13, 417-428, 16 October 1972
9. C. T. Sah and H. S. Fu
Current and capacitance transient responses of MOS capacitor. II. Recombination centers in the surface space charge layer
Phys. Stat. Sol. (a), v14, 59-70, 16 November 1972
10. J. M. Herman, III and C. T. Sah
Thermal ionization rates and energies of holes at the double acceptor zinc centers in silicon
Phys. Stat. Sol. (a), v14, 405-415, 16 December 1972

11. T. H. Ning and C. T. Sah
Theory of scattering of electrons in a nondegenerate semiconductor surface inversion layer by surface oxide charges
Phys. Rev. B, v6, 4605-4613, 15 December 1972
12. S. Pantelides and C. T. Sah
Theory of impurity states in semiconductors
Solid-State Communications, v11, 1713-1718, 15 December 1972
13. L. D. Yau, C. F. Smiley and C. T. Sah
Thermal emission rates and activation energies of electrons and holes at cobalt centers in silicon
Phys. Stat. Sol (a), v14, 655-662, 16 December 1972
14. J. M. Herman, III and C. T. Sah
Photoionization cross sections of holes at zinc centers in silicon
J. Appl. Phys., v44, 1259-1262, 1 March 1973
15. C. T. Sah and J. W. Walker
Thermally stimulated capacitance for shallow majority-carrier traps in the edge region of semiconductor junctions
Appl. Phys. Letts., v22, 384-385, 15 April 1973
16. J. W. Walker and C. T. Sah
Properties of one-MeV electron-irradiated defect centers in silicon
Phys. Rev. B, v7, 4587-4605, 15 May 1973
17. L. D. Yau, C. F. Smiley and C. T. Sah
Application of the transmission line equivalent circuit model to the analysis of the pn junction admittance under d.c. bias
Solid-State Electronics, v16, 895-901, 1 August 1973
18. D. H. Eaton and C. T. Sah
Series equivalent circuit representation of the SiO₂-Si interface and oxide trap states
Solid-State Electronics, v16, 841-846, 1 August 1973
19. F. Hennig and C. T. Sah
Matrix analysis of distributed semiconductor circuit models
Solid-State Electronics, v16, 1081-1083, 1 September 1973
20. J. M. Herman, III and C. T. Sah
Thermal capture of electrons and holes at zinc centers in silicon
Solid-State Electronics, v16, 1133-1139, 1 October 1973
21. C. T. Sah and F. A. Lindholm
Transport in semiconductors with low scattering rate and at high frequencies
Solid-State Electronics, v16, 1447-1448, 1 December 1973
22. J. W. Walker and C. T. Sah
Spherical square well defect potential model for one MeV electron irradiated defects in silicon
Phys. Rev. B, v8, 5597-5603, 15 December 1973

23. J. W. Walker and C. T. Sah
Characteristics of 1 MeV electron-irradiated surface-controlled silicon junction diodes
Radiation Effects, v20, 187-195, 1973
24. T. H. Ning and C. T. Sah
Effects of inhomogeneities of surface-oxide charges on the electron energy levels in a semiconductor surface-inversion layer
Phys. Rev. B, v9, 527-535, 15 January 1974
25. L. D. Yau and C. T. Sah
Quench-in centers in silicon p+n junctions
Solid-State Electronics, v17, 193-201, February 1974
26. C. T. Sah and H. S. Fu
Transient response of MOS capacitors under localized photoexcitation
IEEE Trans. on Elec. Dev., vED-21, 202-209, March 1974
27. K. Hess and C. T. Sah
Hot carriers in silicon surface inversion layers
J. Appl. Phys., v45, 1254-1257, March 1974
28. M. J. McNutt and C. T. Sah
High frequency space charge layer capacitance of strongly inverted semiconductor surfaces
Solid-State Electronics, v17, 377-385, April 1974
29. S. T. Pantelides and C. T. Sah
Theory of localized states in semiconductors. I. New results using an old method
Phys. Rev. B, v10, 621-637, 15 July 1974
30. S. T. Pantelides and C. T. Sah
Theory of localized states in semiconductors. II. The pseudo impurity theory application to shallow and deep donors in silicon
Phys. Rev. B, v10, 638-658, 15 July 1974
31. M. J. McNutt and C. T. Sah
Effects of spatially inhomogeneous oxide charge distribution on the MOS capacitance-voltage characteristics
J. Appl. Phys., v45, 3916-3921, September 1974
32. K. Hess and C. T. Sah
Warm and hot carriers in silicon surface-inversion layers
Phys. Rev. B, v10, 3375-3385, 15 October 1974
33. C. T. Sah, C. T. Wang and S. H. Lee
Junction edge region thermally stimulated capacitance (TSCAP) on n-Si doped with phosphorus and bismuth
Appl. Phys. Letts., v25, 523-524, 1 November 1974
34. Karl Hess and C. T. Sah
Dipole scattering at the Si-SiO₂ interface
Surface Science, v47, 650-654, 1975

35. M. J. McNutt and C. T. Sah
Experimental observations of the effects of oxide charge inhomogeneity of fast surface state density from high-frequency MOS capacitance-voltage characteristics
Appl. Phys. Letts., v26, 378-380, 1 April 1975
36. K. Hess, A. Neugroschel, C. C. Shiue and C. T. Sah
Non-Ohmic electron conduction in silicon surface inversion layers at low temperatures
J. Appl. Phys., v46, 1721-1727, 1 April 1975
37. C. T. Sah and C. T. Wang
Experiments on the origin of process-induced recombination centers in silicon
J. Appl. Phys., v46, 1767-1776, 1 April 1975
38. K. Hess and C. T. Sah
High frequency hot electron conductivity and admittance in Si and Ge
Solid-State Electronics, v18, 667-669, July/August 1975
39. M. J. McNutt and C. T. Sah
Determination of the MOS oxide capacitance
J. Appl. Phys., v46, 3909-3913, September 1975
40. M. J. McNutt, C. T. Sah, R. Van Overstraeten, G. Declerck and P. Muls
Comments on "Effects of spatially inhomogeneous oxide charge distribution on the MOS capacitance-voltage characteristics"
J. Appl. Phys., v46, 5057, November 1975
41. M. J. McNutt and C. T. Sah
Exact capacitance of a loss-less MOS capacitance
Solid-State Electronics, v19, 255-257, March 1976
42. Karl Hess, G. Dorda and C. T. Sah
The current-voltage characteristics of field-effect transistors with short channels
Solid-State Communications, v19, 471, 01 May 1976
43. K. Miyata and C. T. Sah
Thermal emission rates and activation energies of electrons at tantalum centers in silicon
Solid-State Electronics, v19, 611-613, 01 July 1976
44. C. C. Shiue and C. T. Sah
Studies of electron screening effects on the electron mobility in silicon surface inversion layers
Surface Science, v58, 163-172, 01 August 1976
45. T. H. Ning and C. T. Sah
Photoionization cross sections of a two-electron donor center in silicon
Phys. Rev. B, v14, no. 6, 2528-2533, 15 September 1976
46. C. T. Sah and A. Neugroschel
Concentration profiles of recombination centers in semiconductor junctions evaluated from capacitance transients
IEEE Trans. on Elec. Dev., vED-23, no. 9, 1069-1074, September 1976

47. Herman Maes and C. T. Sah
Application of the equivalent circuit model for semiconductors to the study of Au-doped p-n junctions under forward bias
IEEE Trans. on Elec. Dev., vED-23, no. 10, 1131-1143, October 1976
48. K. Y. Tsao and C. T. Sah
Temperature dependence of resistivity and hole conductivity mobility in p-type silicon
Solid-State Electronics, v19, 949-953, 01 November 1976
49. C. T. Sah
Bulk and interface imperfections in semiconductors
Solid-State Electronics, v19, 975-990, 01 December 1976
50. R. L. Marchand and C. T. Sah
Studies of thermally induced deep levels in Al-doped silicon
J. Appl. Phys., v48, no. 1, 338-341, 01 January 1977
51. C. T. Sah
Detection of defect and impurity centers in semiconductors by steady-state and transient junction capacitance and current techniques
Semiconductor Silicon 1977, Proceedings of the Third International Symposium on Silicon Materials Science and Technology, v77-2, 868-893, 9-13 May 1977
52. R. L. Marchand, A. R. Stivers and C. T. Sah
Recombination centers in aluminum-doped silicon diffused in high phosphorus concentration
J. Appl. Phys., v48, no. 6, 2576-2580, 01 June 1977

METRIC SYSTEM

BASE UNITS:

<u>Quantity</u>	<u>Unit</u>	<u>SI Symbol</u>	<u>Formula</u>
length	metre	m	...
mass	kilogram	kg	...
time	second	s	...
electric current	ampere	A	...
thermodynamic temperature	kelvin	K	...
amount of substance	mole	mol	...
luminous intensity	candela	cd	...

SUPPLEMENTARY UNITS:

plane angle	radian	rad	...
solid angle	steradian	sr	...

DERIVED UNITS:

Acceleration	metre per second squared	...	m/s
activity (of a radioactive source)	disintegration per second	...	(disintegration)/s
angular acceleration	radian per second squared	...	rad/s
angular velocity	radian per second	...	rad/s
area	square metre	...	m
density	kilogram per cubic metre	...	kg/m ³
electric capacitance	farad	F	A·s/V
electrical conductance	siemens	S	A/V
electric field strength	volt per metre	...	V/m
electric inductance	henry	H	V·s/A
electric potential difference	volt	V	W/A
electric resistance	ohm	Ω	V/A
electromotive force	volt	V	W/A
energy	joule	J	N·m
entropy	joule per kelvin	...	J/K
force	newton	N	kg·m/s
frequency	hertz	Hz	(cycle)/s
illuminance	lux	lx	lm/m ²
luminance	candela per square metre	...	cd/m ²
luminous flux	lumen	lm	cd·sr
magnetic field strength	ampere per metre	...	A/m
magnetic flux	weber	Wb	V·s
magnetic flux density	tesla	T	Wb/m
magnetomotive force	ampere	A	...
power	watt	W	J/s
pressure	pascal	Pa	N/m
quantity of electricity	coulomb	C	A·s
quantity of heat	joule	J	N·m
radiant intensity	watt per steradian	...	W/sr
specific heat	joule per kilogram-kelvin	...	J/kg·K
stress	pascal	Pa	N/m
thermal conductivity	watt per metre-kelvin	...	W/m·K
velocity	metre per second	...	m/s
viscosity, dynamic	pascal-second	...	Pa·s
viscosity, kinematic	square metre per second	...	m ² /s
voltage	volt	V	W/A
volume	cubic metre	...	m ³
wavenumber	reciprocal metre	...	(wave)/m
work	joule	J	N·m

SI PREFIXES:

<u>Multiplication Factors</u>	<u>Prefix</u>	<u>SI Symbol</u>
$1\ 000\ 000\ 000\ 000 = 10^{12}$	tera	T
$1\ 000\ 000\ 000 = 10^9$	giga	G
$1\ 000\ 000 = 10^6$	mega	M
$1\ 000 = 10^3$	kilo	k
$100 = 10^2$	hecto*	h
$10 = 10^1$	deka*	d
$0.1 = 10^{-1}$	deci*	d
$0.01 = 10^{-2}$	centi*	c
$0.001 = 10^{-3}$	milli	m
$0.000\ 001 = 10^{-6}$	micro	μ
$0.000\ 000\ 001 = 10^{-9}$	nano	n
$0.000\ 000\ 000\ 001 = 10^{-12}$	pico	p
$0.000\ 000\ 000\ 000\ 001 = 10^{-15}$	femto	f
$0.000\ 000\ 000\ 000\ 000\ 001 = 10^{-18}$	atto	a

* To be avoided where possible.

MISSION
of
Rome Air Development Center

RADC plans and conducts research, exploratory and advanced development programs in command, control, and communications (C³) activities, and in the C³ areas of information sciences and intelligence. The principal technical mission areas are communications, electromagnetic guidance and control, surveillance of ground and aerospace objects, intelligence data collection and handling, information system technology, ionospheric propagation, solid state sciences, microwave physics and electronic reliability, maintainability and compatibility.